Non-contact friction studied with pendulum AFM

Inauguraldissertation

zur

Erlangung der Würde eines Doktors der Philosophie
vorgelegt der
Philosophisch-Naturwissenschaftlichen Fakultät
der Universität Basel

von

MSc. Markus Samadashvili

aus Rheinfelden, Baden-Württemberg

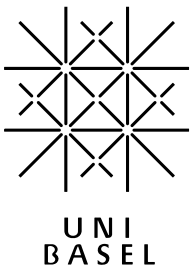

Basel, 2014

Genehmigt von der Philosophisch-Naturwissenschaftlichen Fakultät

auf Antrag von:

Prof. Dr. Ernst Meyer
Prof. Dr. Martino Poggio

Basel, den 25. März 2014

Prof. Dr. Jörg Schibler
Dekan

creative commons

Namensnennung-Keine kommerzielle Nutzung-Keine Bearbeitung 2.5 Schweiz

---

Sie dürfen:

das Werk vervielfältigen, verbreiten und öffentlich zugänglich machen

Zu den folgenden Bedingungen:

Namensnennung. Sie müssen den Namen des Autors/Rechteinhabers in der von ihm festgelegten Weise nennen (wodurch aber nicht der Eindruck entstehen darf, Sie oder die Nutzung des Werkes durch Sie würden entlohnt).

Keine kommerzielle Nutzung. Dieses Werk darf nicht für kommerzielle Zwecke verwendet werden.

Keine Bearbeitung. Dieses Werk darf nicht bearbeitet oder in anderer Weise verändert werden.

- Im Falle einer Verbreitung müssen Sie anderen die Lizenzbedingungen, unter welche dieses Werk fällt, mitteilen. Am Einfachsten ist es, einen Link auf diese Seite einzubinden.
- Jede der vorgenannten Bedingungen kann aufgehoben werden, sofern Sie die Einwilligung des Rechteinhabers dazu erhalten.
- Diese Lizenz lässt die Urheberpersönlichkeitsrechte unberührt.

Quelle: http://creativecommons.org/licenses/by-nc-nd/2.5/ch/ Datum: 3.4.2009

Contents

1 Abstract

The goal of natural sciences is to advance on every level. Nature has a headstart of 16 billion years and achieves naturally the optimal solution for a given problem set. However, mankind is eager to catch up the giving knowledge gap. The science of physics itself is dedicated to understand the fundamental basic concepts of nature, why things happen, the way they happen.
The devision of material science inside physics is interested to understand the properties of matter, which is all around us and the keen interest is to gain control over material properties, to shape them in the way mankind desires to achieve better and smarter technology. In that sense, the rapid increase of the technological progress of the last century is not comparable to the millennium before.
The goal of every thesis is to contribute to this advancements. This thesis is dedicated to investigate the effects of frictional processes on the nanoscale [1], especially in the non-contact regime. Why is this important? Despite the fact that frictional studies have a long history, ranging back to the investigations of Leonardo da Vinci in the 15th century [2], our everyday life is full of examples including frictional processes. Some of them are desired, like the brakes on your mountain bike, the friction of a tire on the street, or your sole of a shoe, when walking in the winter on icy surfaces. Others are undesired, since contact friction always accompanies wear and lead the breakdown of mechanical parts and cause enormous maintenance costs for the industry and costumers. *In the case you asked yourself, why the coffee grinder of your fully automated coffee machine broke for the third time.*
The investigation and understanding of non-contact friction leads to the advantage of gaining control over friction properties in the absence of wear [3]. In this thesis several mechanisms leading to the existence of non-contact friction at the nanoscale are studied and discussed.
Chapters 2 and 3 concern the tool of choice, the pendulum AFM and the relevant forces and why it is a wonderful tool to investigate non-contact friction, chapter 4. The fundamental concepts of the experimental setup are discussed in chapter 5. Since the pendulum AFM is not a common tool in the research field and it is hardly discussed in literature, a detailed introduction of the working principal and sensing mechanism is given for the first time in chapter 6.
Furthermore, the basic concepts are applied on a widely studied reference system, copper with sodium chloride, see chapter 7, where the non-contact friction behavior of a metal-insulator substrate is investigated. The result of this chapter show a distinguishable difference in the smooth rise of the non-contact friction due to the existence of an dielectric media on top of a metal, causing Joule dissipation.
Moving on to more challenging system in the chapter 8, with a rather special electronic phase transition, the **C**harge **D**ensity **W**ave (CDW), observed in niobium-diselenide $NbSe_2$ below $T = 34K$. Here, we state for the first time the observation of discrete non-contact friction maxima multiplets. In collaboration with group of

Prof. Dr. Erio Tosatti it was possible to find the theoretical explanation to the newly discovered non-contact friction mechanism. We observed hysteresis of the local 2π phase slips in the CDW phase order parameter, under the local influence of the tip potential.
Furthermore, in the last chapter of the thesis, the preliminary results of niobium doped strontium titanate $Nb : SrTiO_3$ (STO) are presented. We observed non-contact friction in the vicinity of the structural phase transition, which was theoretically proposed by Benassi *et al.*, due to the softening of phononic modes at the structural anomaly, when the system becomes slow and soft. In addition, STO offers a second phase transition from the paraelectric state to the ferroelectric, and the random oriented electric dipoles become ordered and form domains in the XY plane. In this phase, we observed a remarkable train of non-contact friction maxima, which still lack a quantitative theoretical explanation. However, a possible candidate for the mechanism is briefly discussed.
In summary, this thesis presents an overview over yet unknown mechanism of non-contact friction of matter, giving an adequate contribution to the understanding of dissipation processes of matter on the nanoscale.

2 Material science with the Atomic Force Microscopy

Feeling atoms is a beautiful way to explain the working principal of the Atomic Force Microscope (AFM) . Two atoms feel already an interaction force between each other, even at separations of several nanometer. The average force at those distances is on the order of several pico Newton (pN) and can increase for small separations to several nano Newton (nN). The goal of an AFM is to be sensitive enough to detect these forces. Since the invention of the Atomic Force Microscope in 1986 [4], and the technique of Dynamic Force Microscopy (DFM) [5] [6], the layout of an AFM did not change drastically. Nevertheless, let me briefly mention the detection mechanism.
Lets consider a vibrating bar, if it is driven in a harmonic regime, meaning that the restoring force of the prong is proportional to the driving force, it has due to its own geometry a fundamental resonance frequency. The angular frequency is then determined by the square root of restoring force k devided by the mass m of the bar $\omega = \sqrt{\frac{k}{m}}$. If a force gradient is acting on the vibrating bar, the restoring force will exert an addition component $k_{eff} = k + k_{interact}$. Depending on the interaction the effective spring constant will be larger or smaller. Taking the effective spring constant now into account, we find that ω_{eff} will be different. Since the restoring force in the Hook's regime is given by $F_{restore} = -k \cdot x$, we see in first approximation

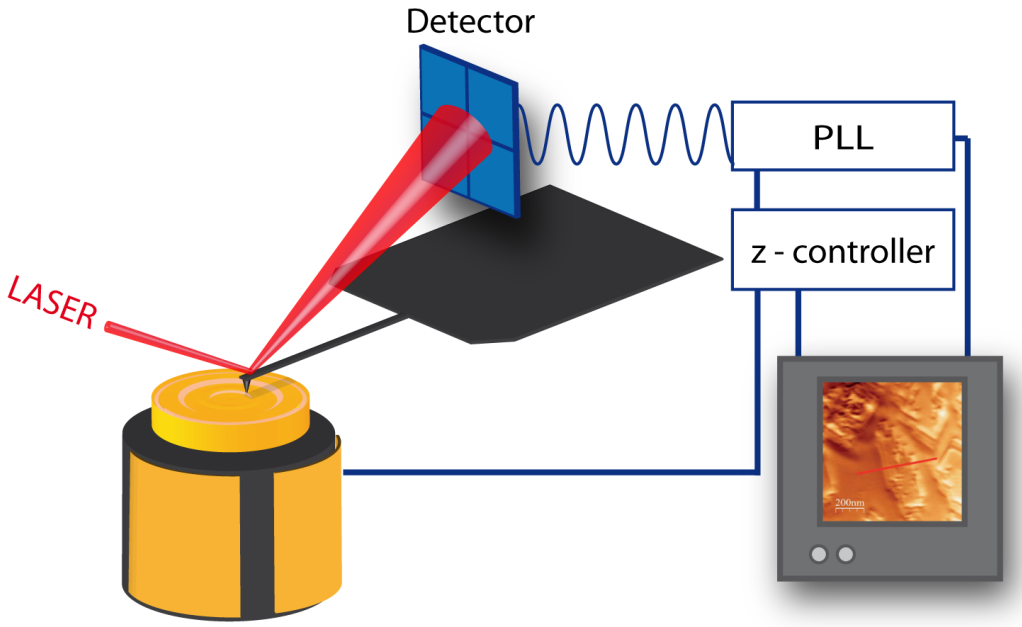

Figure 2.1. Schematics of the common AFM

a proportionality of the angular frequency to the force.
To be able to detect a frequency change of our vibrating bar, upon single nano Newton, we must decrease the mass m of the bar. Todays vibrating prongs, namely cantilevers, are about $150 - 450\mu m$ long, $30 - 50\mu m$ wide and $1 - 5\mu m$ thick. They are made out of silicon and have a mass of $0.1 - 2.6 \cdot 10^{-10} g$, which is sufficiently low in order to be affected in the resonance frequency upon a pico newton force.
To detect the oscillation of a cantilever, a beam deflection detection system is commonly used. This enables to measure the oscillation amplitude and frequency with high fidelity. Since a harmonic oscillator, which was kicked for a single time, rings down, due to internal and external losses, one has to excite the cantilever continuously. A Phase-Locked-Loop (PLL) electronics is doing this job. It can track the frequency, oscillation amplitude, determine the phase compared to a reference oscillation and excite the oscillator continuously.
Therefore, it is also straightforward to understand, that if the harmonic oscillator interacts with the surface in a non-conservative way, the harmonic oscillator will lose the stored energy. Hence, the oscillation amplitude will decrease. Nevertheless, the PLL is now set to keep the oscillation amplitude at a constant value, thus, the excitation of the oscillation has to rise accordingly to maintain the setpoint. Due to this fact, we can relate the excitation voltage to dissipation processes in the tip sample junction.
In the common AFM, the cantilever is oscillating parallel to the surface. At the end of the continuously vibrating cantilever is a sharp tip pointing towards the surface. If the tip is brought close to the probing surface, the front most "atom" of the tip will feel the closest atom on the surface. The interaction between these two atoms, will shift the fundamental frequency of the cantilever towards a lower frequency. This shift of the frequency is constant, for a fixed oscillation amplitude and a certain distance.
A Scanning of the surface, with a feedback to the distance controller for a fixed frequency shift will result in a topography, see figure 2.1, similar to a plane flying at a constant distance over Switzerland.
AFM in the scientific research, evolved from an imaging tool to a highly advanced surface characterization tool. Due to its high sensitivity to forces and its adaptability to various environments, the AFM gives valuable insight to the forces and dissipative processes on the nanoscale [3, 7–9].

3 AFM relevant forces

What is meant by "feeling an atom"? Feeling something is mainly used for human perception, which has usually very little association with science on the nanoscale. Anyhow, if you as a reader, touch the paper of this freshly printed thesis and try to flip the page, you will find it hard to do so under dry conditions. Therefore, some readers will lick their fingers tips before touching the page and flip it. But why does that work?
If it is dry, your fingers have less interaction with the surface of the paper. Due to the finite roughness of your fingers and the paper's surface the interacting area is also reduced. While licking the fingers will deposit a small liquid layer on them an increase the adhesive force to the paper surface and in addition the interaction area. The paper is then sticking to the tip of your finger, or in other words, the paper exerts a larger attractive force to the finger.
This example shows that surfaces attract each other and the attraction can be changed by means of different materials. The interaction between atoms is therefore an important aspect to understand surface properties of matter [10, 11].
To take this example into account, an AFM tip acts like a finger on the atomic scale [12]. Going down, in the dimensions towards atoms one will find, that particular forces are relevant for different spacings. Here, it is useful to introduce the decay length of forces, meaning the distance at which a particular force contribution becomes negligible compared to other contributions or to the force sensitivity of the detector.
However, there are several origins of the total measured force in vacuum, to name them from the point of their decay length, we have the electrostatic, the van der Waals, the chemical interaction and the Pauli-repulsion force. The interaction of these force adds up to the total measured force [6, 13–15], leading to:

$$F_{total} = F_{el.} + F_{vdW} + F_{Chem.} + F_{Pauli} \tag{3.1}$$

Here, the Pauli-repulsion is the only contribution, which is of repulsive character, which prevents matter from collapsing to a single point. Except of the Pauli-repulsion all other AFM relevant forces act attractive between two bodies.

3.1 Electrostatic interaction

An illustrative presentation of the magnitude and long range character of this force, almost every experienced sometimes, if a pullover is taken off we feel the hair to stand up right and away from each other. This phenomenon is due to the static charges picked up by the hair from our pullover. If enough charges occupy the same volume, it can lead to an electrical discharge.
For static charges, the force can have both characters, repulsive for charges of the

same sign and attractive for charges of the opposite one. In the case of two single hair fibers, namely H_1 and H_2, we find that the repelling force is proportional to the number of charges in a infinitesimal volume on each one Q_1, Q_2 and the distance $\mathbf{r}$ between them (see Fig.: 3.1)

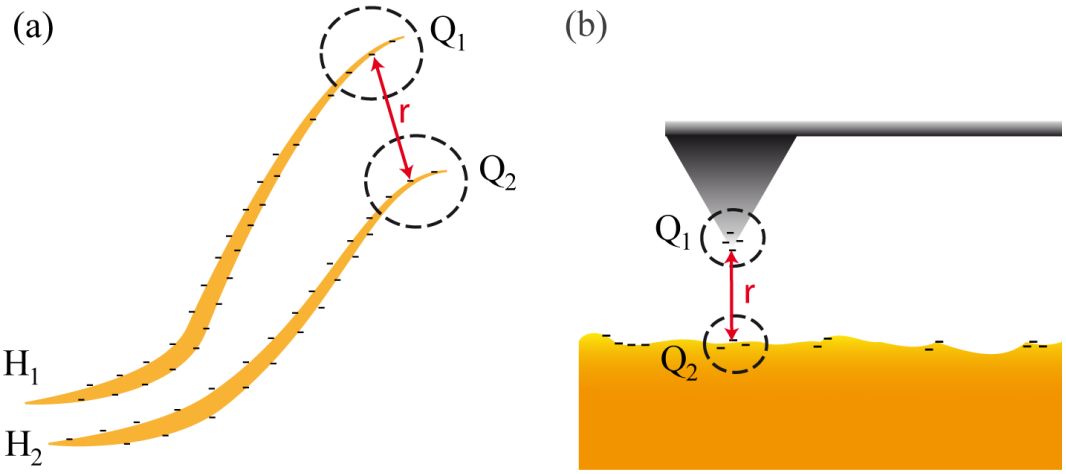

Figure 3.1. In (a) it is illustrated, that two hair repel each other, due to the electrostatic force. In (b) the same is noted on the same principal for an AFM tip above the surface.

Bringing it down a mathematical form we result in:

$$F_{Coulomb}(\mathbf{r}) = \frac{1}{4\pi\epsilon_0}\frac{Q_1 \cdot Q_2}{\mathbf{r}^2} \tag{3.2}$$

where ϵ_0 denotes the vacuum permittivity. In the case of the AFM, static charges might remain after surface preparation. This rare in common AFM, but explains in some cases the positive frequency shifts for large separations in a spectroscopy.
However, if two metallic surfaces brought closely together in an electric circuit, they exert an attractive force between them. This force is due to the capacitance. If a bias potential is applied to the circuit, the force depends on the area enclosed and quadratically on the potential U over the distance $\mathbf{r}$, leading to $F_{capacitor} = \frac{\epsilon_0}{2}\frac{A \cdot U^2}{\mathbf{r}^2}$. This force arises even without a external potential U, if the two capacitor plates are from different materials, due to their work function. The difference in the work function, is called the contact potential difference (CPD). While for a plate capacitor it is quiet simple do derive the dependence, it is quite humbling for a conical tip above the surface, due to the long decay of the electrostatic force, and the stray fields of the conical tip. Hudlet *et al.* [16] calculated the force of the a sphere with an conical extension above an metallic surface. A sphere placed above an infinite plane exerts a force, at distances larger than the radius of the sphere, $z \gg R$:

$$F_{sphere}(z) = -\pi\ \epsilon_0 \frac{R^2}{z^2} \cdot U^2 \tag{3.3}$$

However, in the case of the whole tip the expression needs to take the opening angle ψ and the height H of the tip into account. The full calculation of Hudlet *et al.* is described here [**?**], nevertheless the total electrostatic force on the tip is then:

$$F_{total\ el.}(z) = -\pi\ \epsilon_0\ U^2 \left[\frac{R^2}{z\,(z+R)} + c^2 \left(\ln \frac{z+R}{H} - 1 + \frac{R/\sin\psi_0}{z+R} \right) \right] \tag{3.4}$$

with $c^2 = \frac{1}{[\ln \tan(\psi_0/2)]}$. If the tip is closer to the surface than its radius, $z \ll R$, the tip surface force dependence changes to $\pi\epsilon_0 R/z$. Meaning that the force is dominated by the contribution of the apex [16].
To simplify the terms, the tip dependence is combined in the capacitance gradient $|\partial C/\partial z|$. In addition, a shift of the potential minimum is introduced accordingly to the contact potential difference U_{CPD}, resulting in the most common notation for the electrostatic force dependence for AFM:

$$F_{el.}(z) = -\pi\epsilon_0 \left| \frac{\partial C}{\partial z} \right| (U - U_{CPD})^2 \tag{3.5}$$

3.2 VAN DER WAALS interaction

Lets picture a small story. Mr. VAN DER WAALS *is single and entered a disco on Saturday night. In that disco he finds a large number of people, all single, half men, half women, separated on two side of the dance floor. He moves to the men side, the music is playing the people are dancing. Since, Mr.* VAN DER WAALS *is single, he looks around and sees a beautiful woman on the other side. He is excited and starts shouting at her that the should look at him and should come over. The attracted woman looks at him and finds him attractive as well. So, they start interacting and want to dance together. Then Mr.* VAN DER WAALS *discovers another beautiful woman and is excited about her as well, so he shouts to her. Since the beautiful woman noticed that Mr.* VAN DER WAALS *is into another woman now, she feels not attracted to him anymore and turns away. The third member perturbed the interaction between Mr.* VAN DER WAAL *and the beautiful woman. Nevertheless, he is interacting right away the next one... Therefore, everyone attracts a little with every other, however, no one is really interacting with one other.*
The VAN DER WAALS interaction is pretty similar to this little disco analogy, just between two neutral particles. The expectation value to find an electric dipole vanishes for an neutral particle, nevertheless, quantum mechanical and thermal fluctuations trigger electric dipole d_1. A electric field arises and induces a polarization $\alpha_2/\mathbf{r}^3$ at another neutral particle with a distance dependence $1/\mathbf{r}^3$. This influence leads to dipole moment d_2 at the second particle. Here, the interaction of the second dipole with the first particle induces a polarization $\alpha_1/\mathbf{r}^3$ back at the first particle [17]. Hence, from this the interaction between two particles can be characterized by:

$$V_{vdW.}(\mathbf{r}) = -\frac{d_1 \cdot d_2}{\mathbf{r}^3} = -\frac{\alpha_1 \cdot \alpha_2}{\mathbf{r}^6} \tag{3.6}$$

However, two macroscopic objects cannot be described simply by the sum of all particle interactions. The difficulty is due to the perturbation of a dipole and the rapid decay of the polarization by a third particle. Meaning the potential is highly non additive for large objects, which lead to major difficulties in the theoretical approach. In case of an cantilever hovering on top of an surface the potential inter-

action can only be empirically described. The distance dependence was found to be $V_{vdW}(\mathbf{r}) = 1/\mathbf{r}$, where the interaction force is found and described by:

$$F(\mathbf{r}) = -\frac{dV(\mathbf{r})}{d\mathbf{r}} \tag{3.7}$$

$$F_{vdW.}(\mathbf{r}) = -\frac{H\ R}{2\ \mathbf{r}^2} \tag{3.8}$$

with the Hamaker constant H, which describes the fit parameter of the complex interaction, multiplied by the Radius R of the tip [13, 14, 18].

3.3 Chemical interaction described by the Lennard Jones potential

What holds crystals together? How can we describe solids, by means of interaction with another atom [2, 12, 13]? One of the simplest approach was proposed by Lennard Jones. He investigated the interaction of molecular crystals of noble gases. The approach of him is based on empirical finding and had to take three facts into account [13].

1. For large separation distances the attractive potential is scaling with $1/\mathbf{r}^6$.
2. The potential becomes strongly repulsive for short distances
3. The potential has one minimum and the depth and the equilibrium distance is given by two parameters ϵ, σ respectively.

The interaction of two noble gas atoms, exert a distortion of their closed-shell configuration, which can be described by the fluctuating dipole interaction, as mentioned in the previous chapter of the van der Waals interaction. This leads to a weak attractive potential for large distances. However, to prevent a crystal of collapsing to infinite density, a rapid increasing short range repulsive force has to be present. The origin lies in the repulsion of ion cores, which determine also the equilibrium distance of two atoms toward each other.
It became convenient to describe the behavior as a power law. Here, it is simply convention to choose for the potential a exponent of 12 of the repulsive part. Nevertheless the potential has the form

$$V_{LJ}(\mathbf{r}) = -\frac{A}{\mathbf{r}^6} + \frac{B}{\mathbf{r}^{12}} \tag{3.9}$$

A, B are positive constants in the mathematical form. However, generally the equation is found to be

$$V_{LJ}(\mathbf{r}) = 4\epsilon\left[\left(\frac{\sigma}{\mathbf{r}}\right)^{12} - \left(\frac{\sigma}{\mathbf{r}}\right)^{6}\right], \qquad \begin{array}{l}\sigma = (B/A)^{1/6},\\ \epsilon = A^2/4B,\end{array} \tag{3.10}$$

Furthermore, we find the expression for the Lennard Jones force as mentioned in eq.: 3.7:

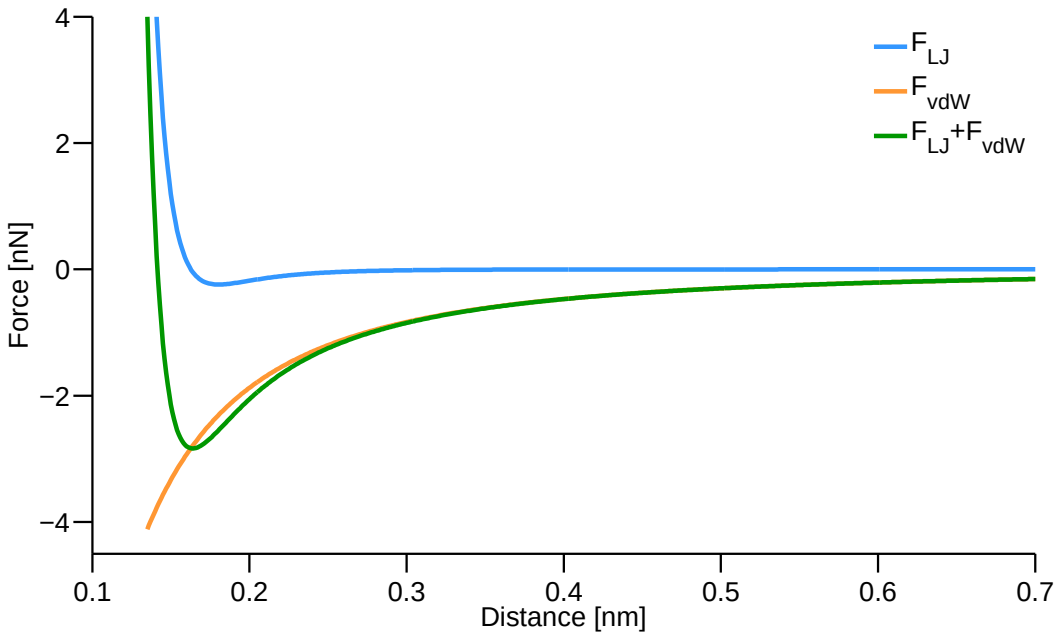

Figure 3.2. The distance dependence of two forces are plotted. On the one hand, the LENNARD JONES interaction force (red), on the other the VAN DER WAALS contribution (blue). The sum of both is plotted in purple. The parameters chosen for the plotting are, $\sigma = 0.145nm$ equilibrium distance, $\epsilon = 0.1nN$ binding energy, $R_{tip} = 15nm$ tip radius, $H = 0.1 \cdot 10^{-19} Joule$ for the Hamaker constant.

$$F_{LJ}(\mathbf{r}) = \frac{24\epsilon}{\sigma}\left[\left(\frac{2\sigma}{\mathbf{r}}\right)^{13} - \left(\frac{\sigma}{\mathbf{r}}\right)^{7}\right], \tag{3.11}$$

The depence of the LENNARD JONES interaction force is plotted in figure 3.2, as well as the VAN DER WAALS force. The sum of both forces is shown, which manifests the characteristically response of the force distance spectroscopy for an AFM.
The three described forces have all one thing in common. These potentials and with it the Forces itself are all conservative interactions. Meaning, any gain in energy of the interaction is fully reversible. This lead to the conclusion, that they cause no energy loss in the system, if it is a closed system.
However, real physical systems are never closed and therefore energy loss occurs. It is a normal process in nature to convert energy in forms like heat, radiation, oscillations [12,19–21]. Nevertheless, it is desired to control the origins, to manipulate the material properties to match the costumers need. For this reason, it is highly recommended to study the origins. In the following chapter, several origins of energy losses on the nanoscale are discussed in detail.

4 AFM and non-contact friction

The theory of non-contact friction on the nanoscale is still an ongoing topic in todays research. The origins and magnitude still lead to controversial discussions. The topic remains unclear, even though enormous effort has been made to design extremely sophisticated measuring tools or the access to large scale computing, providing possibility to understand their theoretical origin [12, 22–29]. In a basic concept one can formulate the idea, that energy losses are only possible, if an initial state E_i differs from the final state E_f, by a process, which is not continuous. For instance, an atom moving forth and back in a potential gradient, will not loose energy unless it changes its final state by emitting energy in form of radiation, phonons, plasmons or polarons.

$$E_i \neq E_f \tag{4.1}$$

In order to understand the energy dissipation between two interacting objects, one must first understand the energy loss mechanisms in the sensor itself.
In case of an AFM, the cantilever is beautifully described by a damped harmonic oscillator. The vibrational amplitude is decaying in time, due to the fact, that the kinetic energy exerts losses until it reaches its thermodynamic equilibrium. The detectable amplitude is in equilibrium with the stochastic fluctuations of the force due to the finite temperature of the system. In such a linear damped system the dynamics of a harmonic oscillator is:

$$m_{eff}\frac{d^2x(t)}{dt^2} + \Gamma\frac{dx(t)}{dt} + m_{eff}\ \omega_0^2\ x(t) = f_{ext}(t) + F(x(t)) \tag{4.2}$$

where $F(x(t))$ is the tip sample interaction force and f_{ext} is the external force to maintain the steady state of the oscillator, which equals to the sum of all damping forces, the stochastic and the non-stochastic. Every quantity can be derived from this linear differential equation 4.2, which describes the motion of the cantilever. Here, Γ denots the friction coefficient, which is in direct proportionality to the friction force and the velocity v of the oscillator.

$$F = -\Gamma \cdot v \tag{4.3}$$

However, the friction coefficient Γ is the sum of all dissipation channels in the probe. Therefore we have to take the following into account:

$$\Gamma = \Gamma_1 + \Gamma_2 + \Gamma_3 + \cdots + \Gamma_N \tag{4.4}$$

Where N denotes the N-th channel of dissipation. Anyhow, we will regard Γ_0 in the following sections as the friction coefficient of the pure damped harmonic oscillator, without any additional interaction. This fundamental friction coefficient can be found

experimentally by measuring the decay time τ of the amplitude for the resonantly excited cantilever. This so called quality factor Q, is determined by:

$$Q = \frac{\tau \cdot \omega_0}{2} \tag{4.5}$$

From the knowledge of the spring constant k of the oscillator, one can determine the fundamental friction coefficient of the system, by the relationship:

$$\Gamma_0 = \frac{k}{\omega_0 \cdot Q} \tag{4.6}$$

In Γ_0 all loss effects of the system are combined. However, the main origins of losses in the sensor are the following [12]:

1. Thermoelastic dissipation.
2. Damping due to bulk losses of the sensor.
3. Damping due to surface losses of the sensor.
4. Losses due to acoustic emission.
5. Dissipation due to clamping of the sensor.
6. Viscous damping due to the presence of gases and liquids around the sensor.

In order to minimize the internal losses, we need to discuss the origins shortly.

4.1 Internal Losses

Viscous damping is not in particular an internal loss mechanism, nevertheless it can be a major issue. Since, the oscillation through gaseous and liquid media is desired for the purpose of a particular study [2,12]. Anyhow, for the further investigations of this thesis, viscous damping has a negligible influence, since we operate under Ultra High Vacuum (UHV) conditions, which means pressures below $p_{base} < 1 \cdot 10^{-10}\ mbar$. Further we can minimize the losses of clamping, since it can be optimized by the use of rigid metallic clamping of the sensor itself. In addition, the absence of glue with a high internal damping the losses decrease. An additional loss factor is the clamping of the vibrating cantilever bar at the support chip. If the crystal contains a large defect density at the interface, the transmission of the vibration is suppressed and leads to shear friction. The setup of the holder used in this work is shown in the further chapters 6.
The acoustic emission into the surrounding can be neglected due to the same practical reasons as in the case of viscous damping. Since, the remaining gaseous media in our measurements has a density comparable to the pressure, acoustic emission is improbable, since the propagation of an acoustic wave is a propagating density variation. Therefore, we can consider the first three mentioned loss mechanisms as the most important losses of the underlying sensor. For a micro mechanical oscillator at room temperature, the thermoelastic dissipation is considered to be the dominant factor.

4.1.1 Thermoelastic Dissipation

Microelectromechanical (MEMS) oscillators are often the choice for high fidelity, highly accurate sensor systems [5]. These oscillators are predominantly used in their flexural or torsional vibrational mode [30]. Here, the thermoelastic (TE) dissipation mechanism [31] is one of the dominant loss channel at room temperature [32]. The periodic expansion and compression of a vibrating element is accompanied with thermal currents between the compressed and expanded areas, in an elastic media. Regarding this we easily acknowledge, that the heat flow between the opposing faces of the compressed areas takes place. Therefore, the distance between them is one of the determining factors for the loss rate. Thus, the thickness influences the thermal phonon current as well as energy dissipation. Hence, the energy loss due to the thermoelastic dissipation can be given by:

$$\frac{1}{\omega}\frac{dE}{dt} = \phi_f^0 \; E_f \tag{4.7}$$

where ϕ_f^0 denotes the internal friction resulting from the pure flexure, E is the total energy of the mode, and E_f is the energy of the bending mode. Under the assumptions, that eq:4.7 is the loss rate of an arbitrary mode, we can determine the loss rate of a particular oscillation by:

$$\phi_f = \phi_f^0 \; \frac{E_f}{E} \tag{4.8}$$

The loss factor associated with a pure flexure was first predicted by Zener [33] and is given here by Nowick and Berry [34] as:

$$\phi_f^0 = \frac{\alpha^2 \; T \; E}{c_P} \frac{\omega_f \; \tau}{1 + (\omega_f \tau)^2} \tag{4.9}$$

where E is the Young's modulus, α the thermal expansion coefficient, c_P the specific heat per unit volume, T the temperature and τ the thermal relaxation time. where τ is further specified as:

$$\tau = \frac{a^2 \; c_P}{\pi^2 \; \kappa} \tag{4.10}$$

where a is the thickness and κ the thermal conductivity.
The thermoelastic dissipation is scaling linear with the temperature and was found (ref) to be dominant at room temperature and above. However, it can be considered rather negligible to the internal dissipation below $T = 150K$ [16]. Therefore other loss mechanisms must be taken into account.

4.1.2 Damping due to bulk and surface losses

In a vibrating beam the scattering of elastic waves upon defects in the bulk or adsorbents on the surface is an important loss mechanism. The oscillating beam is creating a time dependent local stress field. Where the propagation of energy through the media is scattered by crystal imperfection and changes the landscape of the stress field. Here, we neglect instabilities due to defects jumping in between lattice sites. Since the activation barrier is to high compared to the local energy of the stress field,

induced by a nanometer sized oscillation.
Further, we anneal our cantilevers under UHV conditions at temperatures above $500°C$ for several hours and it has been shown experimentally that the Q-factor can be improved by orders of magnitude [35]. In first considerations, adsorbents, like H_2O, CO, are removed from the surface of the sensor, since, the temperature is higher than the desorption temperature of the adsorbents. However, most desorption is taking place already at lower temperatures ($T = 150°C$) [36]. Anyhow, the Q-factor improves even further for longterm annealing at high temperatures. Thus, the desorption is not the only factor for improvement. Hence, defects and impurities of the bulk silicon change upon the high annealing temperature and in result of that decrease in the amount or density.
The quality of the crystallographic structure influences the local stress field. It is known [37, 38], that amorphous Si_3N_4 cantilevers reach lower Q-factors than comparable cantilevers made of SiO_2, by the factor of roughly $500 - 1000$.
To characterize the loss mechanism in a silicon single crystal cantilever oscillating at its fundamental mode, we have to consider first, what determines the fundamental resonance in a beam. The fundamental resonance is the solution of the beam equation with the lowest frequency component. Higher modes of oscillation refer to solutions with higher frequencies. Figure 4.1 indicates the first four eigenmodes for a cantilever beam, which is used in ladder measurements. Further, the color scale denotes the stress field of the beam at the maximum bending, the color scale is in arbitrary units. However, the stress field differ greatly from one eigenmode to the next.
Textbook physics defines the resonance ω of a harmonic oscillator by:

$$\omega_{1st} = \sqrt{\frac{k_{1st}}{m_{eff}}} \tag{4.11}$$

where, k_{1st} is the spring constant or restoring force of the first resonance and m_{eff} is the effective mass of the oscillator. While the spring constant k_{1st} of a rigidly anchored, rectangular beam can be further determined by:

$$k_{1st} = \frac{E\ w\ a^3}{4\ l^3} \tag{4.12}$$

with E as the Young's modulus, w width, a thickness and l length of the beam. Assuming a single Young's modulus E and disregarding any other loss factors, a single Dirac peak like resonance is expected. The resonance width is the measure of the Q-factor of an oscillator and its magnitude of internal losses. The vanishing peak width would imply an undamped, lossless, harmonic oscillator. The measured resonance broadening would not be expected, under UHV conditions, cryogenic temperatures of $T = 4K$ and minimized loss factors, by long term annealing.
The measured width of the resonance (4.2) might be estimated by taking into account an inhomogeneous Young's modulus $E(x, y, z)$ within the beam. Where the macroscopic quantity $E(x, y, z)$ is influenced by the local defect density on the atomic scale. Therefore, the equation 4.12 should take this inhomogeneities into account and should be rewritten as follows:

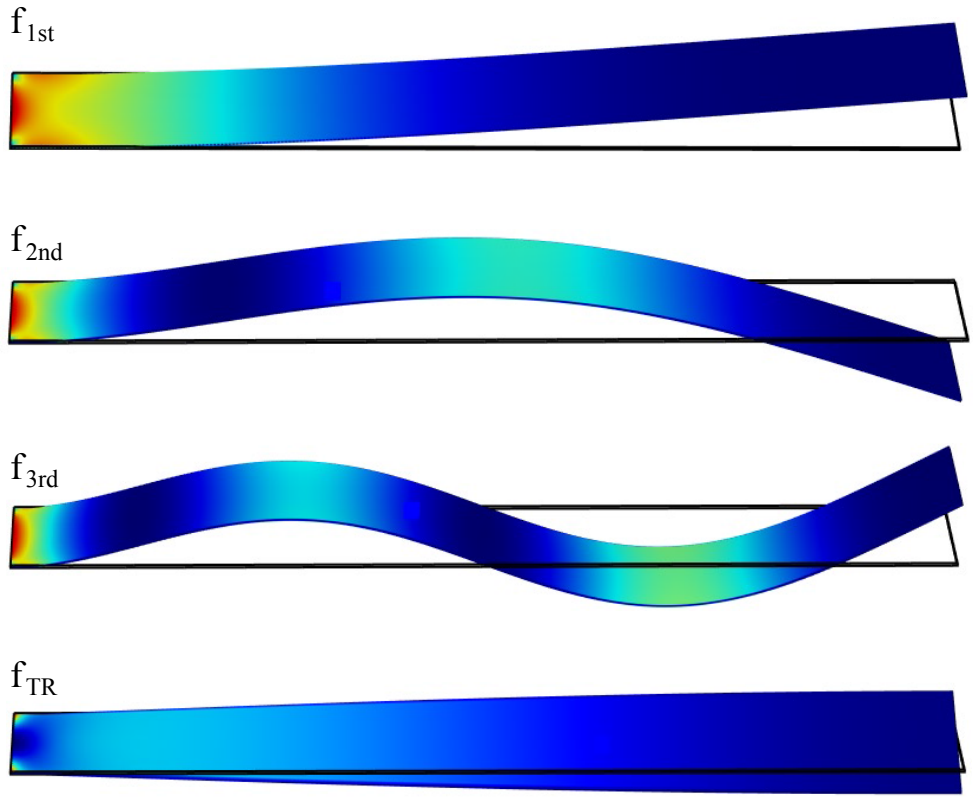

Figure 4.1. The series of beams are the plotted solutions of the beam equation of a cantilever, which is used in the ladder work. The dimensions of the beam are $450\mu m, 50\mu m, 1.5\mu m$, for the length, width and thickness, respectively. The first three resonances are the flexural solutions, while the last is the first torsional resonance.

$$k = \frac{E(x,y,z)\ w\ a^3}{4\ l^3} \tag{4.13}$$

where the tensor $E(x,y,z)$ takes the local Young's modulus into account.
Let's draw an analogy to an acoustic wave in an empty room. If your hear an echo, it means that the wave got reflected by the walls, with a high reflection coefficient, traveling forth and back between you and the walls. Nevertheless, the wave also has a finite possibility to be absorbed on the wall. The absorption on the wall is comparable to the thermoelastic damping, releasing the acoustic wave energy into the wall by phonon emission, heating the wall. The Q-factor is the measure of how often you hear your echo.
If the same room is filled with objects, the wave will be attenuated and scattered on each object, leading to a de-phasing of each scattering event. Even though the absorption is still possible, the echo will vanish due to the destructive interference of the superimposed waves with different phases.
We propose, that the loss rate of the vibrating beam can be approximated by the energy transfer between the time dependent local stress fields. Assuming that the energy oscillates between the stress fields, forth and back, are comparable to an acoustic wave in a solid media. We can determine a transmission and reflection

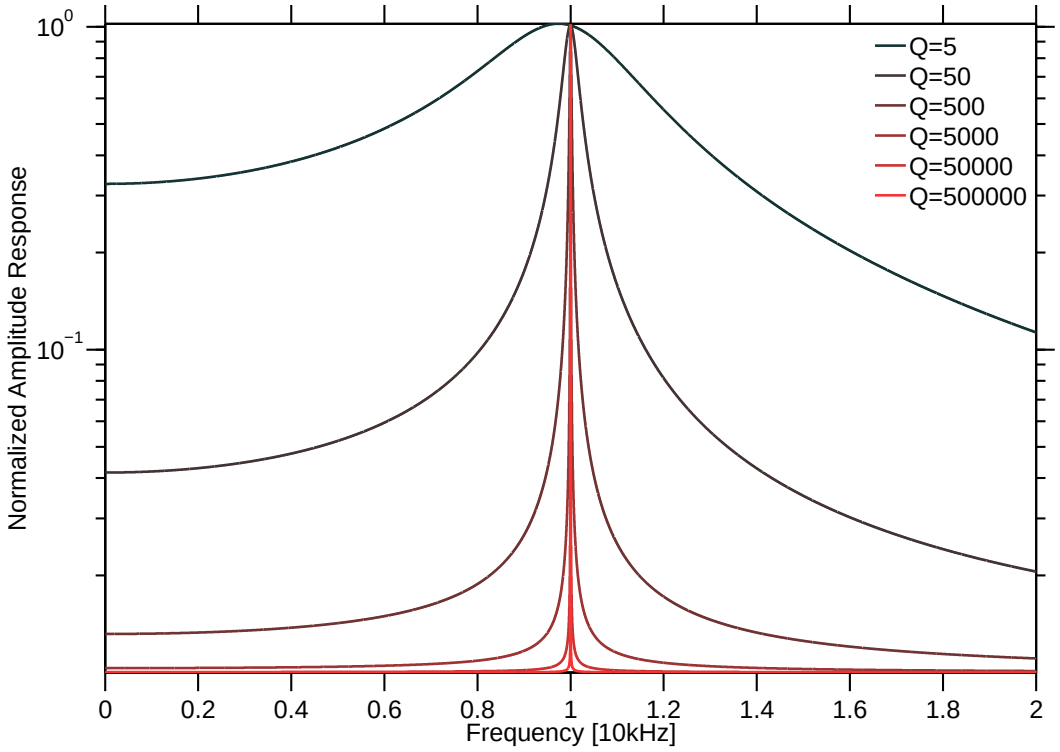

Figure 4.2. The figure shows a series of normalized amplitude response versus the frequency. The center frequency is in this case 10 kHz, while the width of the resonance indicates the internal losses or the quality factor, by the relationship $f/\Delta f = Q = E/\Delta E$. The Q-factors plotted from $5 - 50$ are measured in liquid environment. From 500 to 5000 is measured in ambient conditions. While $50000 - 500000$ is measured for UHV as well as cryogenic conditions and long term annealing. Nevertheless, even for the best conditions, one measures a finite width of the resonance, which denotes a non-vanishing internal dissipation. [12]

coefficients inside the beam. The wave equation for the transverse energy oscillation is given by:

$$\begin{aligned} \sigma^+(z) &= e^{ikz} + R_\sigma \cdot e^{-ikz} \\ \sigma^-(z) &= T_\sigma \cdot e^{-ik'z} \end{aligned} \tag{4.14}$$

the boundary conditions at the interface are continuity of the transverse energy oscillation, therefore we can write:

$$\begin{aligned} \sigma^+|_{z=0} &= \sigma^-|_{z=0} \\ \frac{\partial\sigma^+}{\partial z}|_{z=0} &= \frac{\partial\sigma^-}{\partial z}|_{z=0} \end{aligned} \tag{4.15}$$

under the assumption that a wave propagation through the media is dependent on the density ρ, as well as the propagation speed c, which is in a solid determined by $c = \sqrt{E/\rho}$, we result with following boundary conditions:

$$\begin{aligned} 1 + R_\sigma &= T_\sigma \\ \rho c(1 + R_\sigma) &= \rho' c'(1 + R_\sigma) \end{aligned} \tag{4.16}$$

This can be solved for the reflection and transmission coefficients:

$$R_\sigma = \frac{\rho c - \rho' c'}{\rho c + \rho' c'} \tag{4.17}$$

$$T_\sigma = \frac{2\rho c}{\rho c + \rho' c'} \tag{4.18}$$

Therefore, we have a reflection on the surface, due to the change of the density, for vacuum we can set $\rho = 0$ and have a perfect reflection condition with $R_\sigma = -1$. However, inside the beam we consider domains of different Young's modulus. Since the density in silicon does not change considerable upon impurities or doping, we can consider $\rho = \rho'$ for every domain. Nevertheless, the Young's modulus varies strongly on the impurity concentration [39, 40], we find for the reflection and transmission coefficients with $c = \sqrt{E/\rho}$:

$$R_\sigma = \frac{\rho\sqrt{E/\rho} - \rho\sqrt{E'/\rho}}{\rho\sqrt{E/\rho} + \rho\sqrt{E'/\rho}} = \frac{\sqrt{E} - \sqrt{E'}}{\sqrt{E} + \sqrt{E'}} \tag{4.19}$$

$$T_\sigma = \frac{2\rho\sqrt{E/\rho}}{\rho\sqrt{E/\rho} + \rho\sqrt{E'/\rho}} = \frac{2\sqrt{E}}{\sqrt{E} + \sqrt{E'}} \tag{4.20}$$

Here, we acknowledge that the transmission and reflection coefficients are purely depending on the change of the Young's modulus in the domains in a beam. Since, the coefficients take the amplitude change into account, the intensity is determined by the amplitude square of the wave. Therefore, we can determine the energy loss factor ϵ_T by the relation between the initial intensity I_0 to the transmitted I_T:

$$\epsilon_T = \frac{I_T}{I_0} = \frac{4E}{(\sqrt{E} + \sqrt{E'})^2} \tag{4.21}$$

Further, we easily see that a minor change in the Young's modulus results already in a considerable energy loss. Thus, from the definition of the Q-factor with the energy over the energy loss, $Q = E/\Delta E$. We find for a change of $1GPa$ in the Young's modulus for silicon ($E_{Si} = 169GPa$) [39, 40], that the energy loss of crossing one single domain inside the beam, results in an energy loss factor $\epsilon_T = 2.4325 \cdot 10^{-6}$ and therefore results in a Q factor of $Q = E/\Delta E = 1/\epsilon_T = 411097$. This takes into account that the whole energy oscillating between the stress field is crossing such a domain. However, if we consider a local inhomogeneity of the Young's modulus resulting from impurities and lattice defects, then we have to sum over all local energy losses to obtain the total energy loss.

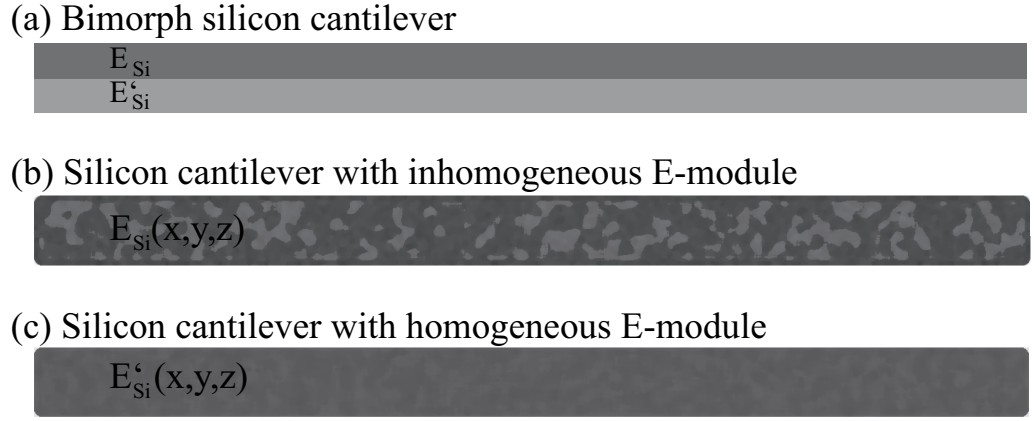

Figure 4.3. The three beams are denoting the possibilities of the underlying Young's modulus in silicon cantilevers. Where, the bimorph silicon cantilever, would suffer energy loss, due to the domain boundary, see Fig.4.3a. Since, impurities or dopants have large effect on the Young's modulus in solids, local variations can occur, see Fig.4.3b. Where each domain contribute to the energy loss, by the particular energy loss factor ϵ_T. However, for a long term annealing treatment of the cantilever, impurity diffusion reduce the local inhomogeneities, see Fig.4.3c. Or in other words, $\langle E \rangle = \langle E' \rangle$, nevertheless $\langle E^2 \rangle > \langle E'^2 \rangle$.

In this picture, the shape of the frequency response of the underlying beam, results in the knowledge of the homogeneity of the Young's modulus. Since, every change leads also to a different frequency response. Further more, it is straightforward, why different resonance frequencies exert different Q-factors, which result from the difference in local stress fields, which address different local variations of the E-module, $(E = E(x, y, z))$. It becomes clear, that long term annealing of the beam improves the Q-factor by two orders of magnitude, since the annealing temperature influences the diffusion of impurities (ref simon rast). This results in a more homogeneous distribution of impurities, leading to a homogeneous Young's modulus within the beam.
The understanding of the internal friction mechanism clarifies the dependence of the lowest detection limit of a probe. Thus we are able to improve the system to reach the desired noise level. In order to reach the aim, perfect clamping, heat treatment, low temperatures, as well as UHV conditions, become unavoidable for the latter measurements.

4.1.3 Minimum detectable force and friction

The first step of a characterization of the used probe, includes the measuring of the minimum detectable friction coefficient and force. The most important quantity is then the quality factor of the probe itself, which determines the lower limit of the detectable friction coefficient as well as the force limit. The straightforward determination of the Q, is done by means of the decay time τ of a resonantly driven cantilever to its thermal noise amplitude. With the relation $Q_i = \pi f_i \tau_i$, the i-th quality factor of the underlying resonance is defined. In addition, the internal friction coefficient is calculated as seen in 4.3 and the force limit by [15]:

$$F_{min,i} = \sqrt{\frac{2k_B T k_i}{\pi f_i Q_i}} \tag{4.22}$$

where, i denotes the i-th resonance. Besides the internal friction coefficient the dissipated power of the free resonantly driven probe can be determined by [19]:

$$P_0 = \frac{\pi k_i A_i^2}{eQ_i} \tag{4.23}$$

where A is the oscillation amplitude of the driven oscillator and e the electronic charge. Further, we can now define the dissipated power due to an interaction with the surface at a particular separation distance d by:

$$P_i(d) = P_0 \cdot \left(\frac{A_{exc_i}(d)}{A_{exc_i,0}} - \frac{f_i(d)}{f_{i,0}} \right) \tag{4.24}$$

with $A_{exc_i,0}$ the i-th excitation amplitude of the free oscillator resonance, $A_{exc_i}(d)$ the i-th excitation amplitude at distance d, $f(d)$ the measured distant dependent interaction frequency of the i-th oscillation and the free i-th resonance frequency $f_{i,0}$. Further, we can deduce from the dissipated energy the distance dependent non-contact friction coefficient Γ_i by:

$$\Gamma_i(d) = P_i(d) \cdot \frac{e}{2\pi^2 A_i^2 f_i} - \Gamma_{i,0} \tag{4.25}$$

Γ_i is independent of the used amplitude of oscillation, as well as the frequency. Therefore, the spring constant and Q-factor determine the lowest detection limit. Thus, measurements of two independent probes or even independent measurement systems can be compared in order to gain the best knowledge of the energy dissipation of the probed material.

4.2 Origins of Non-contact friction

To understand non-contact friction of two objects in relative motion, we have to clarify what we mean by non-contact friction. Friction is always designated by two objects, which are in contact and exert a resisting force against the relative motion. The understanding of friction itself has a long history. It goes back to the first systematic studies of Leonardo da Vinci in the 15^{th} century [2]. In the 17^{th} century, Guillaume Amontons rediscovered the knowledge and stated the first two of three friction laws, which are still valid at the macroscale. Charles-Augustin de Coulomb stated after his extended studies the last of the three fundamental friction laws in the 18^{th} century. The laws are the following:

1. **Amontons' First Law**: The Force of friction is directly proportional to the applied load.
2. **Amontons' Second Law**: The Force of friction is independent to the apparent area of contact.
3. **Coulomb's Friction Law**: Kinetic friction is independent of the sliding velocity.

The laws of friction remain experimentally valid for a wide variety of conditions and also observed in everyday life experience. Furthermore, the laws can be extended, with minor changes, down to the nanoscale, which was shown by calculation and experiments [1, 7, 10, 11, 41].
The area of contact, does play an important role for the measured friction force. However, two surfaces form in almost no case a smooth contact with each other. Bowden stated in the BBC Broadcast 1950 nicely: "*Putting two solids together is rather like turning Switzerland upside down and standing it on Austria - the area of contact will be small.*", [42]. Which means, the surfaces have finite roughness, limiting the contact area to the asperities or "*mountain tops*", which "touch" each other. Further computational studies by Yifei Mo *et al.* [1], showed, that even this small "mountain tops" in contact, do not define completely the contact area. Only the atoms, which are close enough for chemical interactions mainly contribute to the friction. It was further stated that the friction is then linearly depended to the number of atoms, which are chemically interacting.
Thus, we can state, that two objects are in contact, if they are close enough to interact chemically. Therefore, non-contact is further defined by any distance larger than the chemical interaction range.
By this statement the question arises, if and how asperities, which are out of contact can contribute to friction? Or how slippery is vacuum?

In order to explain the non-contact friction between two closely spaced bodies, several well established mechanisms are discussed in literature [12]. These are listed in the following and will be discussed further:

1. Stochastic friction
2. Adhesion Hysteresis
3. Joule dissipation
4. Vacuum or van der Waals friction

The set of non-contact friction mechanisms still lead to ongoing discussions, since the theoretically predicted values might be orders of magnitudes smaller than the experimentally observed ones and published in literature. Nevertheless, a small introduction to each is presented in the following sections.

4.2.1 Stochastic friction

Particles at temperatures above absolute zero have a mean kinetic energy equal to the finite temperature. This motion is referred as the Brownian Motion. Where the instantaneous kinetic energy is given by: $E_{kin} = 1/2\ m \cdot \langle v^2 \rangle = 3/2\ k_b\ T$, where k_b is the Boltzmann constant [12].
Let us consider a Brownian particle with mass M in a system with free particles with mass m and the condition $M \gg m$. The Brownian particle will perform a random walk due to the collisions of the free particles. The average velocity $\langle V \rangle$ of the Brownian particle in an arbitrary direction is zero, resulting from the random collisions. As a result of the motion is described by the stochastic equation:

$$M\frac{d\mathbf{V}}{dt} = \mathbf{F}(t) \tag{4.26}$$

where, $\mathbf{V}(t)$ is the particle velocity at time t and $\mathbf{F}(t)$ is the random force. If the kinetic energy of that Brownian particle is now larger, due to some external force, the velocity is then greater than the one in the thermodynamic equilibrium. Therefore this particle is consider to be a hot subsystem, where the local temperature T_{loc} is given by $E_{kin} = 3/2\ k_b\ T_{loc}$. According to the second law of thermodynamics the energy of the hot subsystem should be given to its surrounding environment until it establishes the thermodynamic equilibrium. Mechanically, we can speak of a random friction force acting on the Brownian particle to reduce its kinetic energy. Let us here, reduce the set to a 1D problem, since collisions perpendicular to the motion of the particle are not dissipative. Let the initial velocity of our Brownian particle be $V > 0$, and the free particles v. Any collision will transfer energy and a momentum to the free particles. Therefore, by using the momentum and energy conservation we find the velocity after an collision at time t_1 to be $V(t_1) = V(t_0) - 2\ m/M(v(t_0) + V(t_0))$. The change of the momentum is then $\Delta K = MV(t_1) - MV(t_0)$ and this is equal to $-2mV$, since $V \gg v$. As a result of this the friction force during the collision is then $F_{col} = \Delta K/\Delta t = -mV/\Delta t$. Concluding, that random collisions result in a friction force proportional to the velocity. The Brownian particle will loose energy until its

velocity becomes equal to the thermal average. The equation of motion can be then written as:

$$M\frac{d\mathbf{V}}{dt} + \Gamma\mathbf{V} = \mathbf{f}(t) \tag{4.27}$$

where Γ is the friction coefficient and $\mathbf{f}(t)$ is a completely random force, which obeys $\langle\mathbf{f}(t)\rangle = 0$.
The coefficient Γ can be determined by averaging over many collisions and can be obtained by the non equilibrium statistical mechanic considerations. However, in the limit of infinity the Brownian particle has experienced a large number of collisions. The average velocity squared should be in thermodynamic equilibrium, namely $\langle\mathbf{V}(\infty)^2\rangle = 3k_BT/M$. So that we obtain for the friction coefficient:

$$\Gamma = \frac{1}{k_BT}\int_0^\infty \langle\mathbf{f}(t_0)\mathbf{f}(t_1)\rangle dt \tag{4.28}$$

where $\langle\mathbf{f}(t_0)\mathbf{f}(t_1)\rangle$ is the autocorrelation function of the random force. The equation 4.28 is better known as the fluctuation-dissipation theorem [43,44]. In particular we can state generally, that "*dissipation processes in a smaller system interacting with a larger one are due to the stochastic nature of the interaction between them*" [12,26,45].
The interaction of a non-contact AFM with a surface, draws several similarities to the Brownian particle motion. Let us consider the tip of an AFM as a Brownian particle, with an overall mass M much larger than the vibrating surface atoms with mass m. Firstly, we can consider the vibrational motion of each surface atom uncorrelated to the neighbor. Further the tip atoms move collectively in an oscillation. Since the oscillation frequency of the tip is rather small ($\sim 10^4 Hz$) compared to the surface vibrations ($\sim 10^{14}$). We consider for every position of the tip z a rather large number of fluctuating interactions, where the fluctuation depends only on the temperature itself.
Futher, the friction coefficient Γ depends on the exact position z of the tip above the surface. If the tip is at the closest position on top of the surface, we can assume that the elastic force of the lever is equilibrated with the interaction force $F_{cons} = 0$. In addition, we assume the zero crossing of driving force $F_{Exc} = 0$. Then we can reduce the equation of motion for the tip:

$$M\frac{d\mathbf{V}}{dt} + \Gamma\mathbf{V} = F_{cons} + F_{Exc} + F_{fluc}(z,t) \Rightarrow M\frac{d\mathbf{V}}{dt} + \Gamma\mathbf{V} = F_{fluc}(z,t) \tag{4.29}$$

where $F_{fluc}(z,t)$ is the random fluctuating tip surface force for the distance z. Therefore we can point out the analogy to the Brownian particle friction coefficient for a single oscillation:

$$\Gamma(z) = \frac{1}{k_BT}\int_0^\tau \langle F_{fluc}(z,0)F_{fluc}(z,t)\rangle dt \tag{4.30}$$

where τ is a characteristic timescale, which is longer than the oscillation time of an atom ω_D and shorter than the oscillation of the tip ω_i, $2\pi/\omega_D \gg \tau \gg 2\pi/\omega_i$.
In further calculation, which can be found [12], the energy dissipation of such a non-contact system is derived, where the energy loss is then given by:

$$\Delta E = \int_0^{2\pi/\omega_i} \Gamma(z) \left(\frac{dx}{dt}\right)^2 dt \tag{4.31}$$

This denotes the total energy loss per oscillation cycle. However, it is difficult to get to real values for the energy loss on the theoretical basis. The random force is difficult to take into account, since it is not possible to describe it by the equilibrium statistical mechanics.

4.2.2 Adhesion hysteresis and accompanied phononic friction

Another mechanism for non-contact friction is the adhesion hysteresis [12]. Here, it is considered, that the atoms in the tip and surface deform in a way, where the force felt by the tip on approach is different to the one on the retraction. This considers a non uniform force field, where the potential energy gained on approach is different and smaller than the one spent on retraction. This is hysteresis will then dissipate the energy of the oscillation to the surface atoms, due to time dependent elastic deformation [3, 20, 27, 46].
There the assumption lies in the case, that the characteristic timescale of the deformation τ_d is comparable to the motion of the tip τ_t, otherwise the dissipation mechanism is inefficient. Second, the deformation of the atoms needs to recover in each oscillation cycle to their original lattice sites to be a continuous loss mechanism. For the case of $\tau_d \sim \tau_t$ the hysteresis reaches the maximum magnitude. There the tip is oscillating above a lattice site. The surface atom is relaxed in the crystal lattice at its equilibrium position A. On the approach of the tip, the atom senses the additional force of the tip and moves to a new equilibrium position B, minimizing the non compensated additional force component. Further the energy spent for a continuous process, would be equal on approach and retract, meaning $\Delta E_{A\to B} = \Delta E_{B\to A}$. Therefore, an energy barrier with finite height must be introduced, in order to get a discontinuous process, which obeys $\Delta E_{A\to B} \neq \Delta E_{B\to A}$.
The reasons for an energy barrier are unclear. However, experiments have shown localized dissipation features on the atomic scale. Further, it is only observed for small tip sample separations, where the force acting on the surface is large. Therefore non linear processes are likely to happen in the tip sample junction [22, 23, 28, 45].

4.2.3 Joule dissipation

This general dissipation mechanism brought light and heat to the world for a century in form of a light bulb. If a current I is flowing through a conductor with resistance R it dissipates power P, the so called Joule dissipation is usually expressed by $P = U \cdot I = R \cdot I^2$, with the power output in Watt.
In non-contact dynamic AFM we encounter this phenomena as well [47]. If a voltage U is applied between tip and sample, the system acts as a distance dependent capacitance. Due to the amplitude A_i of the driven oscillator, the capacitance varies accordingly. The change of capacitance generates an alternating displacement current in the tip upon the oscillation at the driving frequency ω_i. The dynamic distance is then given by $z(t) = z_0 + A_i \cdot \cos(\omega_i t)$, with the mean distance z_0. Further, we can write the displacement current D as:

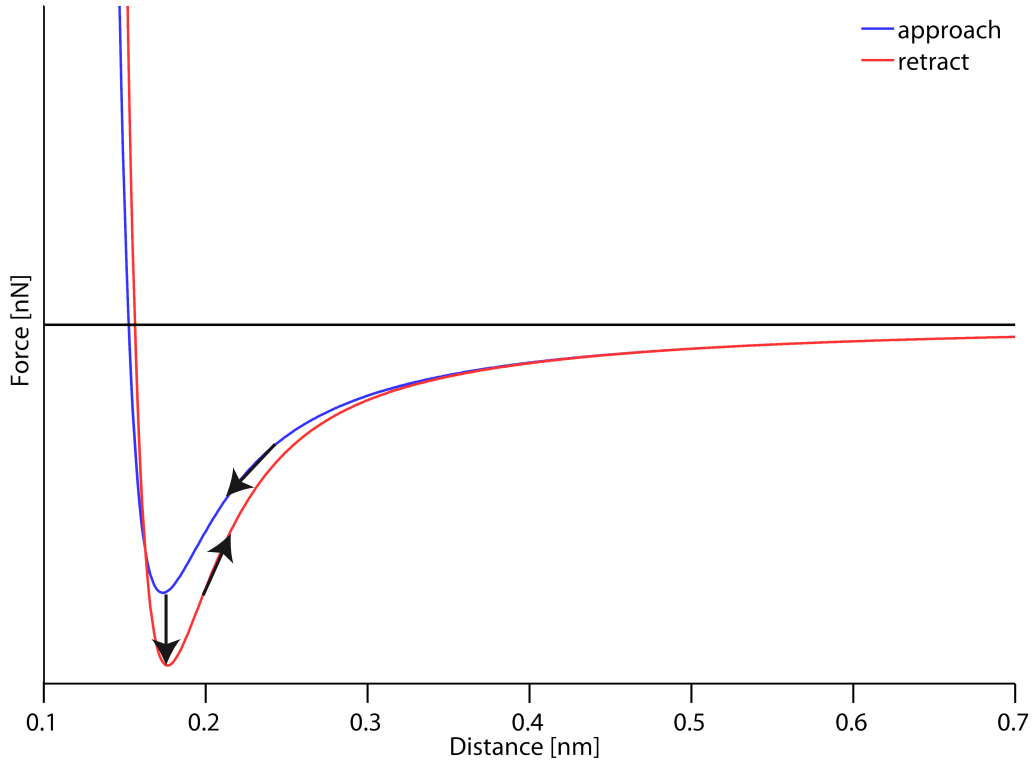

Figure 4.4. The tip follows on the approach the force field of the blue line, where at some point the deformation of the surface takes place. On the retraction curve the tip follows a new force field of the red line. At a certain distance the influence of the tip is negligible and the surface atom relaxes to its original position. This closes the hysteresis loop and the tip feels again the original force field.

$$D(t) = \frac{\partial C}{\partial t} U = \frac{\partial C}{\partial z} \frac{\partial z}{\partial t} U \tag{4.32}$$

with the $\dot{z}(t) = A_i \omega_i \sin(\omega_i t)$ we find for the Joule dissipation:

$$P_{joule} = R_{tip} \cdot D^2(t) = R_{tip} \left(\frac{\partial C}{\partial z} \right)^2 U^2 A_i^2 \omega_i^2 \sin^2(\omega_i t) \tag{4.33}$$

where R_{tip} is the resistance of the tip material used to probe the surface. The average power dissipated $\langle P_{Joule} \rangle$ in one single oscillation cycle is:

$$\langle P_{Joule} \rangle = \int_0^{2\pi/\omega} P_{joule} \, dt = \pi \; R_{tip} \left(\frac{\partial C}{\partial z} \right)^2 \; U^2 \; A_i^2 \; \omega_i^2 \tag{4.34}$$

The average power dissipation of typical magnitudes ($R_{tip} \approx 10^4 \Omega/cm$, $\frac{\partial C}{\partial z} \approx 10^{-9} F/m$, $U \approx 1V$, $A_i \approx 10nm$, $\omega_i \approx 10^4 Hz$) gives:

$$\langle P_{Joule} \rangle \approx 10^{-24} Watt/cycle \approx 10^{-5} eV/cycle \tag{4.35}$$

$10^{-5} eV/cycle$ is above the detection level of a pendulum AFM, however conventional systems do not reach this low internal power dissipation. Therefore, it is much more difficult to expect dissipation in a conventional AFM setup.

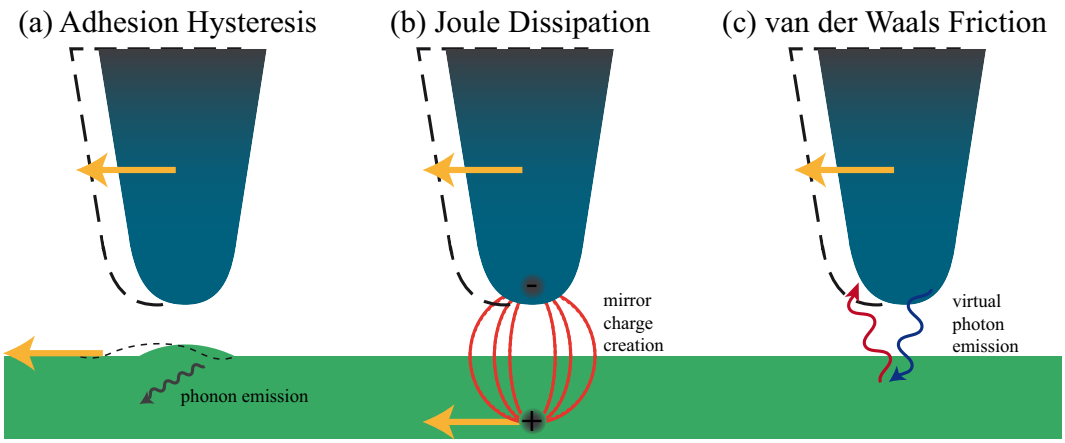

Figure 4.5. Adhesive hysteresis appears at small a tip sample separation of the order of several angstroms. A surface deformation occurs and is dragged along with the tip movement. Upon the spatial variation of this deformation phonons are created and energy loss occurs (ref marcins paper), see (a). Joule Dissipation takes place if non compensated charges of the surface or the tip move through resistive media. The spatial variation creates a displacement current in tip and sample, both exert a resistance, when moved through the media. The delay between each other causes friction. The work done by the tip is then proportional to the force times the displacement, see (b). The Van der Waals Friction is a more subtle dissipation mechanism. It arises from the van der Waals force mechanism, where a spontaneous dipole is created. This emits a real/virtual photon to the surface, where a dipole is induced. The re-emitted photon is absorbed back in the tip. The friction arises due to the fact, that the initial photon compared the the reabsorbed one are Doppler shifted. Therefore, the interaction lost energy is due to the velocity of the tip, see(c)

4.2.4 Van der Waals friction

The van der Waals friction is closely related to the van der Waals force mentioned in section 3.2. The force arises from the quantum fluctuation of the electron density, when a spontaneous dipole is created [26, 44, 48–51]. The short lived dipole interacts with a nearby atom via a photon exchange and induces a dipole moment. The induced dipole re-emits a photon to the original one and a force arises between the two dipoles. Friction occurs between two closely spaced bodies, if they are in relative motion to each other, due to the photon exchange, which is Doppler shifted. This is the origin of the van der Waals friction.
The calculation of the van der Waals friction is more complex than the force, since it originates from the electromagnetic field fluctuations with moving boundary conditions. The literature approaches the solution by regarding each surface in its reference frame. The relation between the two electromagnetic fields of each reference frame is determined by the Lorentz transformation [12, 49, 50]. In the range of "slow" velocities, where AFM is mostly originated, the first approach is by writing the force acting on both bodies as $F = F_0 - \Gamma \cdot v$, where F_0 is the conservative force independent of v and Γ the friction tensor. Since, Γ originates from the electromagnetic field fluctuations, we use the approach of the Stochastic friction, see section 4.2.1, equation 4.30. Where the friction arising from fluctuations is determined by:

$$\Gamma(z) = \frac{1}{k_B T} \int_0^\infty \langle \mathbf{F}_{fluc}(z,0)\mathbf{F}_{fluc}(z,t)\rangle dt \tag{4.36}$$

Here, the $\langle \dots \rangle$ give the thermal average of the fluctuation in the force originating from the electromagnetic field $\mathbf{F}_{fluc}(z,t)$ at a given distance z and time t. Assuming the interacting surfaces as an extended system, the force fluctuations will be then expressed by the stress tensor σ_{ik}:

$$F_i = \int \sigma_{ik} dS_k \tag{4.37}$$

where the force is integrated over the surface i of the i-th body, with the tensor :

$$\sigma_{ik} = \frac{1}{4\pi}\left[E_i E_k + B_i B_k - \frac{1}{2}\delta_{ik}\left(E^2 + B^2\right)\right] \tag{4.38}$$

where, E and B are respectively the electric and magnetic induced fields. The calculation of the force-force correlation function is performed in [12, 50]. This way of calculating has the advantage, since it can be extended to more complex geometries. However, the approach is just for velocities, where the retardation effect of the electric field can be neglected. Further, it needs to be emphasized, that any theoretical approach leaded to friction coefficients, which are several orders of magnitude below experimentally observed ones. Nevertheless, the theoretical approach introduces complex stochastic non equilibrium theory, where a lot of simplifications are made. However, the discrepancy between theory and experiment may be reduced in further investigations.
Nevertheless, pendulum AFM can bring insight to mechanisms and can clarify origins of non-contact friction, due to its high sensitivity. With the standard sensitivity on the order of $\Gamma_{min} = 1 \cdot 10^{-12} kg/s$, it is comparable with other sophisticated setups mentioned in literature [26, 51]. Further, due to its possibility to operate within a wide range of temperatures, namely $4.8K - 300K$, it provides useful insight to the dependence of friction mechanism on the environmental temperature. Since, phase transition of material provides further clearness to origins of non-contact friction. To gain the best knowledge, one must first understand the basic principals of pendulum AFM and its operation mode. Therefore, the technical setup will be discussed in the next chapter, as well as the force detection mechanism in chapter 6.

5 Experimental setup

The surface of a dinner table cleaned with a sponge is anything, but clean. An AFM image of such a surface would show something comparable to a top view of a "rain forest" covering the interesting ground. There will not be any useful information in these measurements. To avoid a "rain forest" from growing on the surface of interest, we have to consider other means of cleaning, than a sponge.
The main dirt on the sample surface originates from contaminants of the air. Therefore, the most straight forward solution is to have a fully depleted environment, which means **U**ltra **H**igh **V**acuum (UHV) conditions. At this environment, the pressure is below $p_{UHV} < 10^{-10} mbar$, and the remaining amount of contaminants is significantly reduced. It is hard to imagine what it means to have such a low pressure, since the ambient pressure at which we live in is $p = 1013 mbar$. As a comparison, the mean pressure on the summit of the Mount Everest is $p_{ME} = 337 mbar$, which is already barely survivable for ordinary human beings. The standard vacuum conditions for the latter measurements, are comparable to the pressure on the moon.
Anyhow, a more comprehensive model is the mean free path of a particle under such pressures. This model estimates the mean distance l, at which a particle travels before it collides with another particle in the gas. The model defines the probability of traveling a certain distance between two successful collisions. This is based on the number of particles n in a gas at a certain pressure with the cross sectional area σ. If all particles are of the same element, then it is straight forward to calculate the mean free path by:

$$l = \frac{1}{\sqrt{2} n \sigma} \tag{5.1}$$

For ambient conditions the mean free path is roughly $l \sim 68 nm$, while in UHV conditions we achieve $l_{UHV} > 10000 km$. This means, a particle travels a very long distance, before it reaches another remnant particle of the vacuum. Since the dimensions of a vacuum chamber are, somewhat small, it also suggests, that a particle collides with the wall of the chamber several thousands of times, where it is most likely to be absorbed, rather than on the sample surface. Thus it is highly favorable to operate an AFM under these conditions, since a probed surface is longer "clean", or free from surface contaminants of the remnant particles in the gaseous phase.
In order to achieve UHV conditions, several pumping stages are connected to chamber to literally "suck the dirt out". The first stage is done by rotary pumps, which provide low vacuum $p_{lv} \approx 10^{-1} mbar$. The second stage are the turbo molecular pumps, which look like small turbo fan engines of a plane, where the shovels of the fan rotate at $1000 Hz$ frequency. If the shovels hit a particle, a kinetic energy is transferred to it, where the trajectory of the particle is changed to leave the chamber, by this method a pressure of $p_{hv} \approx 10^{-9} mbar$ is achieved. The third stage of pumping includes chemical absorption pumps, like **T**itan **S**ublimation **P**umps (TSP) or ion

getter pumps. Both work on similar principal, titanium has an adsorption capability, where a remnant element of the gas is chemically bound to the surface of the vacuum chamber. So a remaining pressure of $p_{UHV} < 10^{-10} mbar$ can be achieved. The additional factor of the system, described here, is the capability to reach cryogenic conditions as well, where the microscope and its chamber are cooled, by either liquid nitrogen ($LN_2 \approx 77K$) or liquid helium ($LHe \approx 4.8K$). A particle hitting a cold wall will lose a fraction of its kinetic energy until it is finally adsorbed or "frozen" on the wall itself.
The cryogenic conditions in the measurement system are not only to improve the vacuum, but to see additional physics of an investigated system. The abundance of physics at low temperatures is a crucial point of this thesis. Where it is necessary to cross phase transitions of a matter and exert phenomena, which are not observable at room temperature.

5.1 The pendulum AFM system

The pendulum AFM is a home built design, from the University of Basel [52], with the capability of working in UHV as well as cryogenic conditions with high magnetic fields ($B_{magnet} = \pm 7T$). The setup of the microscope chamber is shown in figure 5.1(a) with the image of the microscope itself in 5.1(b). The microscope was changed form its original design to allow combined AFM/STM modes. However, the latter measurements were performed in the AFM mode only, since the changes were done at a later time. The original design and the specifications of the cryostat and the microscope can be found in the work of Urs Gysin *et al.* [52].
The microscope was changed to achieve a lower noise floor of the beam detection (**P**hoto **S**ensitive **D**iode, PSD), by a shielded cabling from the PSD to the current-voltage converter (IV-converter). The improved system allows to operate at much lower oscillation amplitudes ($A_{min} \sim 30pm$). In addition, a shielded STM line with a decoupled ground towards the microscope was added. The STM line is desired to perform fast imaging, with the capability of achieving atomic resolution.
The design of the cantilever holder had to be changed, since the old design was purely metallic and therefore made a short cut of the STM current with the microscope ground. In order to avoid grounding the cantilever, an isolator had to be introduced. In the figure 5.2 a CAD drawing of the new cantilever holder is shown. The Omicron UHV transfer holder is the original design, see 5.2 6. The new MACOR ceramics isolator is mounted on top by a molybdenum screw, in oder to withstand the high annealing temperatures, see 5. The Cantilever, 1, as well as the STM platinum-iridium wire, 2, is clamped by a copper block, 3, which provides the electrical contact with the connection arm, 4, via a second molybdenum screw. The advantage of this setup is the capability to measure AFM and STM independently as well as achieving high Q-factors for sensitive AFM measurements.

5.2 AFM operation schematics

In order to measure in the AFM mode a set of electronics has to be configured. Firstly, a laser must be focused on the back of the cantilever, the beam reflection is

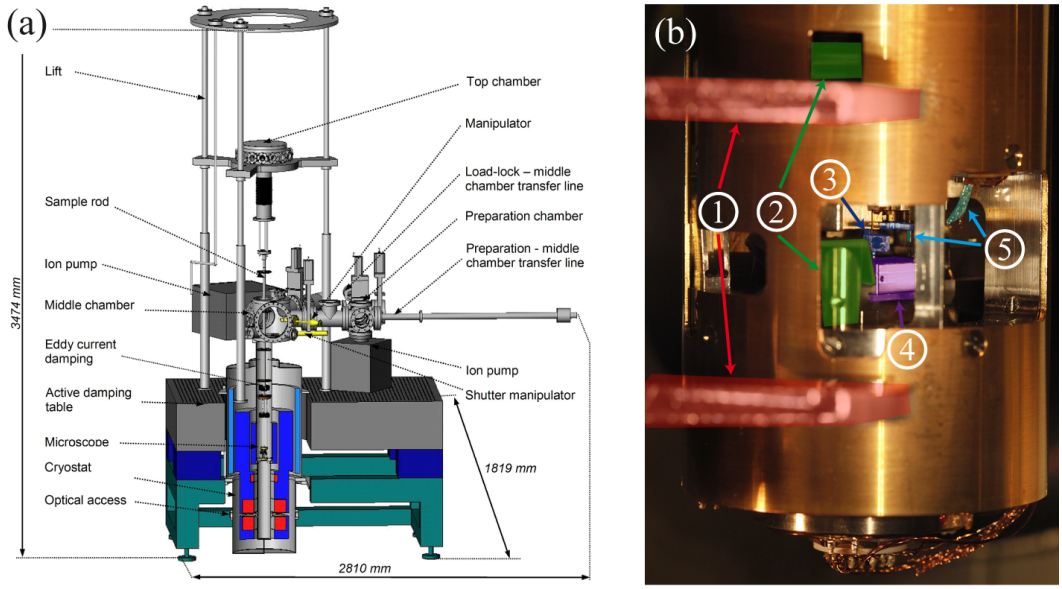

Figure 5.1. The microscope chamber is shown in figure (a) with the top loader cryostat, adapted from reference [52]. The microscope itself is shown in (b), where 1 (*red*) is the microscope holder for transferring, 2 (*green*) the mirrors for the beam deflection detection, 3 (*dark blue*) the cantilever itself, 4 (*violet*) the sample holder and 5 (*light blue*) the STM shielded current line.

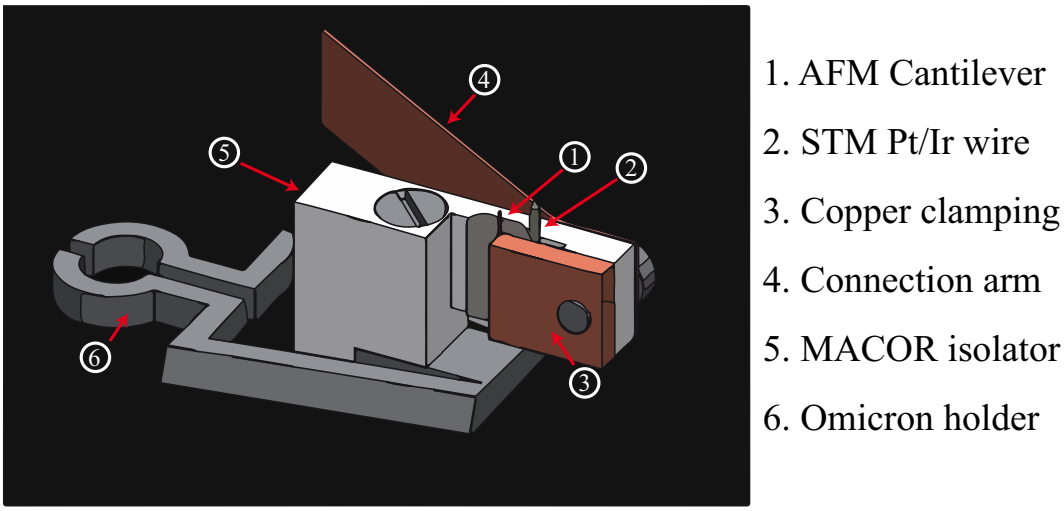

Figure 5.2. The new design of the STM/cantilever holder is shown, with 1 the AFM cantilever, 2 the STM Pr/Ir wire, 3 the copper clamping, 4 the STM connection arm to the STM current line, seen in figure 5.1(b), 5 the MACOR isolator and 6 the Omicron holder for transfer.

brought via mirrors to the four quadrant photo sensitive diode, where the physical oscillation readout to a corresponding oscillating voltage is done. The PSD output is given to the **P**hase-**L**ock-**L**oops (PLL), where the detection of the frequency, amplitude and phase are performed. The corresponding excitation amplitude is brought back to a shaking piezo, in order to excite the cantilever at its fundamental and the

second resonance simultaneously, to reach the desired oscillation amplitude.
The frequency shift of the cantilever is set to zero for "large" separation distances (several microns). The Distance controller gets the current frequency shift value and compares it with a setpoint, approaches if the setpoint is not reached, or retracts if the current value is beyond. The current z value is given to the operator as a topography signal.
Besides the topography, KPFM is acquired simultaneously. Here, an alternating potential U_{ac} is given to the substrate, the resulting modulation of the electrostatic force is picked up by the cantilever, which modulates the frequency shift on the side band. The modulation frequency and its amplitude is fed back to the lock-in of the KPFM module. The Kelvin controller reduces the electrostatic force modulation by a dc voltage U_{dc} until the contact potential is reached. The contact potential voltage U_{CPD} is displayed to the operator.

5.3 Spectroscopy

The pendulum AFM is not an overwhelming imaging tool, it has the capability to acquire a topography, however, due to the lateral oscillation a spacial averaging is performed in every topographic pixel. Hence, atomic resolution hard to reach.
Nevertheless, the strength of the pendulum geometry lays in the spectroscopy. Probing surface properties, which are quasi independent of the lateral positions of the

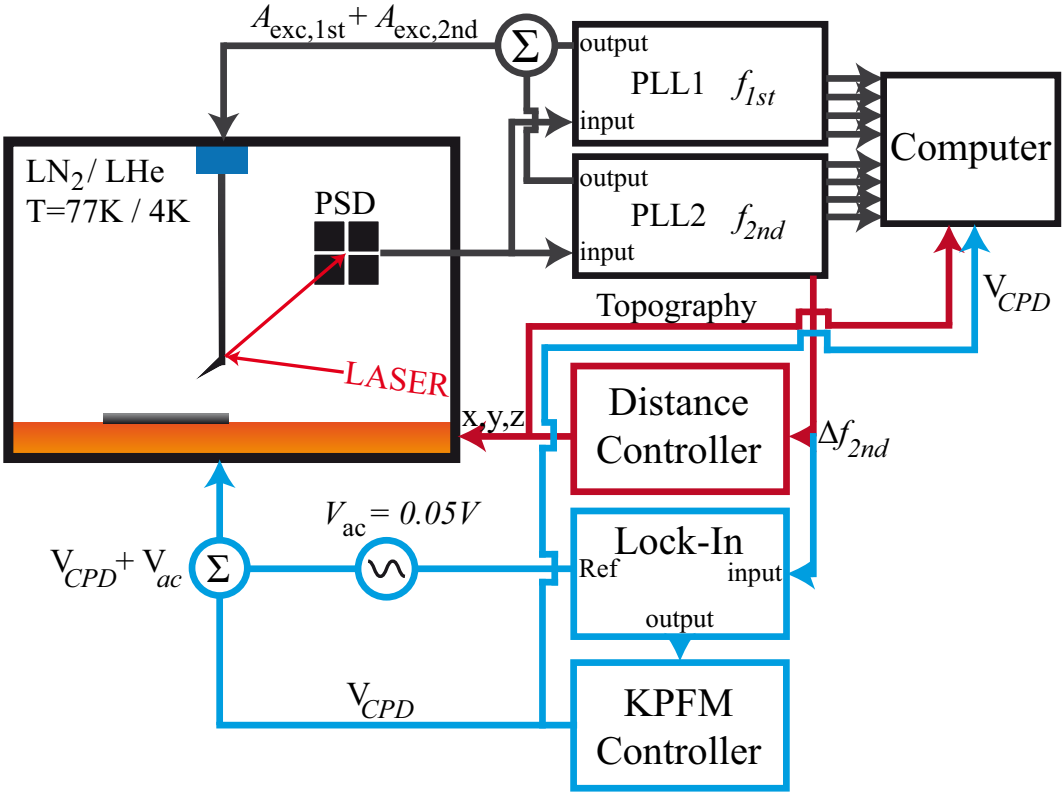

Figure 5.3. The operation schematics.

probe. The one dimensional spectroscopy $1D$ with extremely high sensitivity conservative and dissipative forces, are the working horses of the pendulum AFM. In the latter results section two different types of spectroscopies are used. Firstly, the force distance curve.

5.3.1 Force-Distance Spectroscopy

The force-distance spectroscopy is used to obtain high resolution in the distance dependent force $F(z)$ and dissipation $\Gamma(z)$. Here, the probe is placed at a starting separation distance on top of the surface. The probe is excited at its fundamental resonance to gain higher sensitivity. The oscillation control is set to a desired amplitude, usually $A_L = 5nm$, and the contact potential is compensated to a fixed value and the active tracking by the KPFM controller is switched off. The following signals are then tracked and recorded for later studies: distance z, vertical deflection $Vert$, horizontal deflection $Hori$, frequency shift Δf, phase shift θ, amplitude A_L, excitation voltage Exc.
These signals are recorded for every distance step of the force distance spectroscopy. The distance resolution of the spectroscopy is typically in the range of a few picometer, for an overall spectroscopy range of several tenth of nanometer. Each acquired point is averaged for a second, to prevent signal artifacts of any kind.
The spectroscopies are stopped, when the tip touches the surface, visible in the linear increase of the vertical deflection signal. There are no other means of determining the exact distance of the swept range. The distance dependent non-contact friction is then obtained according to the formula 4.24.
The stability and reproducibility of these long term spectroscopies are given by the temperature stability of the cryostat. Thermal drift of the sample can be neglected in the equilibrated state, due to the long retention time of coolant in the cryostat. Furthermore, an image is taken before and after every series of spectroscopies to rule out irreversible damages of the surface or probe. The same stability concerns are taken into account for the second type of spectroscopy used in the latter measurements.

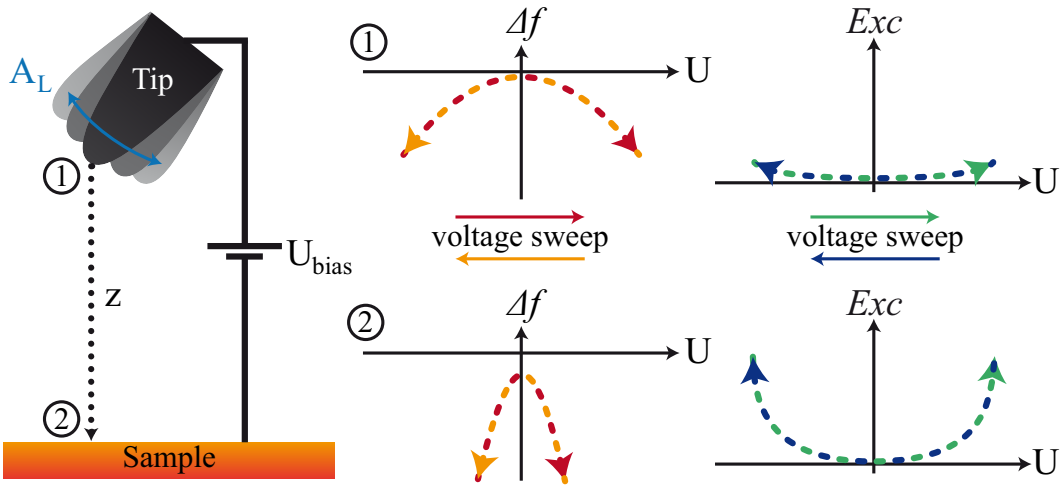

Figure 5.4. The schematics of the bias sweep spectroscopy is seen, where the spectroscopy starts at point 1 to sweep the voltage. The cantilever properties, like frequency shift, excitation, amplitude and phase are acquired for every voltage step of the sweep. The distance z is decreased after the sweep cycle is finished. The bias spectroscopy is stopped if point 2 is reached.

5.3.2 Bias sweep spectroscopy

Bias sweep spectroscopy consists of a set of measurements. Here, the tip is placed at a starting separation distance on the surface, where the signals are set, as mentioned in the force distance spectroscopy. Then the bias U_{bias} is swept forth and back with a certain $\pm\Delta U$ according to the contact potential U_{CDP}. The change in the electrostatic force between the cantilever and the surface, influences the measured frequency shift as well as the excitation voltage. The bias sweep finishes at its initial value, the separation distance is decreased, by one step towards the surface and a new sweep is performed. The whole spectroscopy is stopped, if the sample surface is reached.
In the bias sweep spectroscopy might be distinguished between different mechanism of dissipation, like it is demonstrated in the case of sodium chloride on copper and $NbSe_2$. However, before we start to explore the nature of various dissipation mechanisms, some light has to be shed on the obscure contrast mechanism of the pendulum AFM. Thus, we discuss the sensing mechanism of an AFM oscillating perpendicular to the surface for the first time in detail.

6 Pendulum AFM

6.1 Sensing of forces in a conventional AFM

In this section, we want to discuss, how the force acting on an oscillating cantilever affects the frequency. Therefore, we start by describing the mechanism of a conventional AFM setup and develop the mechanism for the pendulum geometry. The difference lays in the direction in which the force acts. For a conventional geometry the force normal to the surface acts parallel to the cantilever oscillation. Therefore, we are able to directly use the equation of an externally driven damped harmonic oscillator. In case of frequency modulated detection for a non dissipative interaction, the internal damping force is compensated by the external driving force [5,6,13,15,53,54]. Thus, it is possible to reduce the equation of motion 4.3 to the following:

$$m_{eff}\ddot{z(t)} = -k_{eff}z(t) + F(z(t)) \tag{6.1}$$

where m_{eff} is the effictive mass, k_{eff} the effective spring constant, $F(z(t))$ the distant dependent interaction force. In order to solve the equation of motion it is common to use the sample surface as a reference, with $z(t) = z_0 + A_i \cdot \sin(\omega_i t)$. Since, the interaction is distance depended, the force acts sinusoidal on the tip apex, Thus Eq.:6.1 is substituted to:

$$m_{eff}A\omega^2 \sin^2 \omega_i t = -k_{eff}A \sin^2 \omega_i t - k_{eff}z_0 \sin \omega_i t + \sin \omega t \cdot F(z_0 + A \sin(\omega t)) \tag{6.2}$$

Integrating the equation over one oscillation cycle $2\pi/\omega_i$ and resorting results:

$$\begin{aligned}\int_0^{2pi/\omega_i} m_{eff}A\omega^2 \sin^2(\omega_i t) + k_{eff}A \sin^2(\omega_i t)dt = \\ - \int_0^{2pi/\omega_i} k_{eff}z_0 \sin(\omega_i t)dt \\ + \int_0^{2pi/\omega_i} \sin(\omega_i t) \cdot F(z_0 + A \sin(\omega_i t))dt\end{aligned} \tag{6.3}$$

Since, the integration of a sinus is always zero, then $\int_0^{2\pi} \sin(x)dx = 0$ and in addition $\int_0^{2\pi} \sin^2(x)dx = \pi$, so we find for Eq.:6.3:

$$\pi\ Ak \left(\frac{1}{\omega_i} - \frac{m}{k}\omega_i \right) = \int_0^{2\pi/\omega_i} \sin \omega_i t \cdot F(z_0 + A \sin(\omega_i t))dt \tag{6.4}$$

with the identity $\omega_{i,0} = \sqrt{k/m_{eff}}$ and the approximation $\frac{1}{\omega_i} \sim \frac{1}{\omega_{i,0}}$ we get:

$$\pi\ Ak\left(\frac{\omega_{i,0}-\omega_i}{\omega_{i,0}^2}\right)=\int_0^{2\pi/\omega_i}\sin\omega_i t\cdot F(z_0+A\sin(\omega_i t))dt \tag{6.5}$$

in addtion, we use $\Delta\omega_i=\omega_{i,0}-\omega_i$ and $\omega=2\pi f$ to obtain:

$$\frac{\Delta f_i}{f_{i,0}^2}=\frac{1}{\pi\ Ak}\int_0^{2\pi/\omega_i}\sin\omega_i t\cdot F(z_0+A\sin(\omega_i t))dt \tag{6.6}$$

Further, the probe will oscillate a large number of cycles in the same interaction field, therefore we substitute the force interaction to get the time averaged frequency shift, by $\phi=\omega t\Leftrightarrow d\phi/dt=\omega\Leftrightarrow d\phi/\omega=dt$ and still $\frac{1}{\omega_i}\sim\frac{1}{\omega_{i,0}}$:

$$\Delta f_i=\frac{f_{i,0}}{\pi Ak}\int_0^{2\pi}\sin\phi_i\cdot F(z_0+A\sin(\phi_i))d\phi_i \tag{6.7}$$

Equation 6.7 explains the measured frequency shift of the i-th resonance, resulting from the time averaged interaction force. This equation holds for forces acting parallel to the motion of the beam. Further, the frequency shift Δf of any resonance is only true, if the amplitude is constant and the dissipative forces are compensated by the external driving force. The frequency shift relation for an AFM was first deduced from [53]. This holds, for any conventional AFM setup, where the cantilever oscillates perpendicular to the surface. In case of the pendulum AFM the geometry is changed. Thus, the motion of the cantilever is not perpendicular to the plane, but parallel to it. Hence, the lateral force produces a frequency variation as well. Therefore, we discuss here the relation of forces acting on the tip to the measured frequency shift.

6.2 Sensing in pendulum geometry with symmetric cantilevers

Once you measure with the pendulum AFM, you'll get to know, that there is some difference in the way a pendulum AFM acquires the topography. Therefore, it is very important, to discuss the sensing mechanism in detail. Since, the geometry is still exceptional to the field of AFM, it has not been discussed in the literature.
In the conventional geometry of AFM, where the cantilever is mounted parallel to the surface, one suffers from a snap-in-contact, which takes place, when the restoring force is lower than the attractive interaction force. Therefore, cantilevers operating in a non-contact regime, have to have a spring constant, which is larger than $10N/m$, to avoid snapping. The usual spring constant of commercially bought cantilevers for non-contact purpose is about $48N/m$. Since the sensitivity of the minimum detectable force 4.22 and dissipation 4.23 is limited by the spring constant, one expects low sensitivity for this setups. The pendulum geometry suspends the cantilever perpendicular to the surface. Thus, the, snap-in-contact can be avoided, since the elastic elongation of the lever itself is suppressed, due to the high Young's modulus. This enables the possibility to utilize very soft cantilevers of about $k=0.23N/m$, which also have increased Q factors. Therefore, the sensitivity is enhanced in the range of several orders of magnitude ($F_{min,normal}/F_{min,pendulum}\sim 10^2$) for the force as well

as dissipation ($P_{min,normal}/P_{min,pendulum} \sim 10^4$). However, force sensing through the pendulum geometry is not exactly comparable to that of a normal AFM. Firstly, due to the oscillation quasi parallel to the surface, secondly due to the influence of lateral forces to the measured frequency shift.
In order to evaluate this behavior for symmetric cantilevers, one has to solve the equation of motion of the vibrating lever for the normal axial force F_z and add the lateral force F_x into the equation.
A lever with the frequency $\omega = \sqrt{\frac{EI\lambda}{\rho A}}$ in the presence of an external axial force N has the form:

$$\frac{d^4}{dz^4}x\left(z\right) + \frac{N}{EI}\frac{d^2}{dz^2}x\left(z\right) = x\left(z\right)\lambda \tag{6.8}$$

where E is the Young's modulus, Ith area moment of inertia, ρ is the mass density and A is the lever cross section. After substitution $z = ZL$ the lever elongation is $x\left(z\right) = x\left(ZL\right)$ and the equation (6.8) is expressed in dimensionless coordinates Z:

$$\frac{d^4}{dZ^4}x\left(Z\right) + A\frac{d^2}{dZ^2}x\left(Z\right) - \Lambda x\left(Z\right) = 0 \tag{6.9}$$

where $A = \frac{N}{EI}\cdot L^2$ and $\Lambda = \lambda \cdot L^4$. The general solution of equation (6.9) after substitution $a = \frac{1}{2}A$ and $b = \frac{1}{2}\sqrt{A^2 + 4\Lambda}$ has a form of:

$$\begin{aligned} x(Z) = c1\ \cos\left(\sqrt{a+b}Z\right) + c2\ \sin\left(\sqrt{a+b}Z\right) + \\ +c3\ \cosh\left(\sqrt{-a+b}Z\right) + c4\ \sinh\left(\sqrt{-a+b}Z\right) \end{aligned} \tag{6.10}$$

The solution $x(Z)$ after applying boundary conditions $x(0) = \frac{dx}{dZ}_{(x=0)} = 0$ and $\frac{d^2x}{dZ^2}_{(x=1)} = \frac{d^3x}{dZ^3}_{(x=1)} = 0$ for deflection, slope, moment and share force of the deformed lever is:

$$\begin{aligned} x(Z) = & \quad c1(\cos\left(\sqrt{a+b}Z\right) \\ & + \frac{\left(-\cos\left(\sqrt{a+b}\right)a - \cos\left(\sqrt{a+b}\right)b + \cosh\left(\sqrt{-a+b}\right)a - \cosh\left(\sqrt{-a+b}\right)b\right)\sqrt{-a+b}\sin\left(\sqrt{a+b}Z\right)}{\left(\sqrt{-a+b}\sqrt{a+b}\sin\left(\sqrt{a+b}\right) - \sinh\left(\sqrt{-a+b}\right)a + \sinh\left(\sqrt{-a+b}\right)b\right)\sqrt{a+b}} \\ & - \cosh\left(\sqrt{-a+b}Z\right) \\ & - \frac{\left(-\cos\left(\sqrt{a+b}\right)a - \cos\left(\sqrt{a+b}\right)b + \cosh\left(\sqrt{-a+b}\right)a - \cosh\left(\sqrt{-a+b}\right)b\right)\sinh\left(\sqrt{-a+b}Z\right)}{\sqrt{-a+b}\sqrt{a+b}\sin\left(\sqrt{a+b}\right) - \sinh\left(\sqrt{-a+b}\right)a + \sinh\left(\sqrt{-a+b}\right)b}) \end{aligned} \tag{6.11}$$

The boundary conditions yields also to characteristic equation:

$$\begin{aligned} 0 = -a^2\cos\left(\sqrt{a+b}\right)\cosh\left(\sqrt{-a+b}\right) + a^2 + \\ +a\sqrt{-a+b}\sin\left(\sqrt{a+b}\right)\sqrt{a+b}\sinh\left(\sqrt{-a+b}\right) + \\ +b^2 + \cos\left(\sqrt{a+b}\right)\cosh\left(\sqrt{-a+b}\right)b^2 \end{aligned} \tag{6.12}$$

In case of $N = 0$ the equation (6.12) reduces to well known form for the free oscillating lever [55]:

$$\cos\left(\sqrt[4]{\lambda}L\right)\cosh\left(\sqrt[4]{\lambda}L\right)+1=0 \tag{6.13}$$

The equation (6.12) can be easily solved numerically and the solution for a and b is shown in Fig. 1(b) together with the approximated 4th order polynom:

$$\begin{aligned} b &= 3.516+0.221\cdot a+0.146\cdot a^2-0.003\cdot a^3-0.001\cdot a^4= \\ &= b_0+b_1\cdot a+b_2\cdot a^2+b_3\cdot a^3+b_4\cdot a^4 \end{aligned} \tag{6.14}$$

In the particular case of $a=\frac{NL^2}{2EI}=0$, b is equal $b_0=3.516$ - the value for unperturbed problem [55]. We consider the case of $a\ll 1$, i.e. the lack of longitudinal elongation of the lever. The equation (6.14) reduces to:

$$b=b_0+b_1\cdot a=3.516+0.221\cdot a \tag{6.15}$$

and the eigenvalue λ:

$$\lambda=\frac{{b_0}^2}{L^4}+\frac{b_0\,b_1\,N}{L^2EI} \tag{6.16}$$

The eigenfrequency of the cantilever in the presence of normal axial force is then equal:

$$\omega=\omega_0\sqrt{1+\frac{b_1\,NL^2}{b_0\,EI}} \tag{6.17}$$

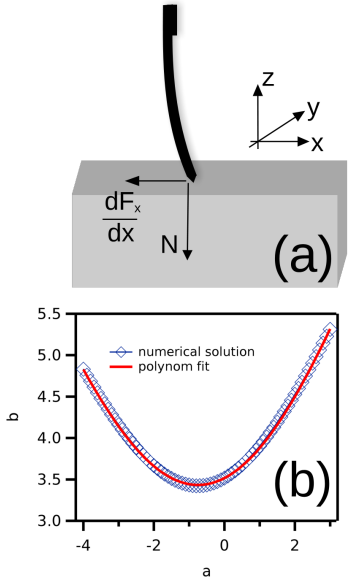

Figure 6.1. Schematic representation of the oscillating cantilever in the pendulum geometry (a), with the normal axial force N and the lateral force gradient $\frac{dF_x}{dx}$. On (b) the numerical solution of eq.(6.12) and the approximated 4th order polynomial fit are shown.

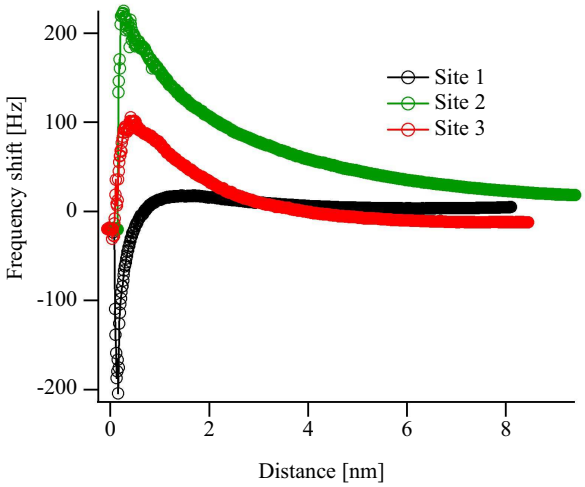

Figure 6.2. In this graph three force distance curves are shown, acquired at different spatial positions on the surface. The huge deviation of each other is clearly visible. Thus, any intension to use symmetric cantilevers acquire topographical images via the frequency shift feedback are foredoomed to fail.

6.2.1 Lateral force gradient

In order to consider the lateral force influence on frequency shift, the additional force $F(x)$ term is added into eq. (6.8). The lateral force $F(x)$ can be expanded in the Taylor series $F(x) \simeq F_0 + \frac{dF_x}{dx}x(z) + ...$ and after neglecting the homogeneous part F_0, eq.(6.8) looks as following:

$$\frac{d^4}{dz^4}x(z) + \frac{N}{EI}\frac{d^2}{dz^2}x(z) - \left(\lambda - \frac{1}{EIL}\frac{dF_x}{dx}\right)x(z) = 0 \tag{6.18}$$

After substitution:

$$\lambda' = \lambda - \frac{1}{EIL}\frac{\partial F_x}{\partial x} \tag{6.19}$$

the eigenfrequency od the oscillating lever is:

$$\omega = \omega_0 \sqrt{1 - \frac{b1\ NL^2}{b0\ EI} + \frac{L^3}{b_0^2 EI}\frac{\partial F_x}{\partial x}} \tag{6.20}$$

or for rectangular lever:

$$\omega = \omega_0 \sqrt{1 - \frac{3b1\ N}{b0\ Lk} + \frac{3}{b_0^2 k}\frac{\partial F_x}{\partial x}} \tag{6.21}$$

Since, the lateral force gradient can have positive or negative values, due to the directional dependence of the interaction, ω can have arbitrary values. Thus, imaging at a constant frequency setpoint is not possible for a symmetric lever. This can be confirmed in site dependent force distance spectroscopies, see figure 6.2. However, imaging possibility is highly desired to refer to site dependent events. The solution to the issue is the asymmetry of the tip, which will be discussed in the following.

6.3 Sensing with asymmetric cantilevers

For all latter measurements, we utilize a commercially bought ATEC Cont cantilever (**A**dvanced **T**ip at the **E**nd of the **C**antilever for **Cont**act mode, see figure 6.3b). The advanced tip makes it possible to establish a stable frequency shift feedback.This originates from the asymmetry of the tip at the end of the lever. To understand the working principal, let us start with the static considerations.

6.3.1 Static force interaction

The ATEC Cont levers are usually $l = 450\mu m$ long, $w = 50\mu m$ wide, $a = 2 - 3\mu m$ thick and have a tip height of $h = 15 - 20\mu m$ advancing the lever bar with an angle of $\theta = 60°$. In the first assumption, which we consider here, the tip is infinitely rigid attached to the lever, which means that the tip-lever angle will not change due to any force interaction. Secondly, we consider no further tip apex deformation. Hence, it is possible to reduce the total picture of tip cantilever to a straight lever, which is clamped at the base and forms a closed triangle with the tip end. This straight lever has then the effective length l_{eff} and encloses an angle α with the actual lever, see fig.: 6.3a.

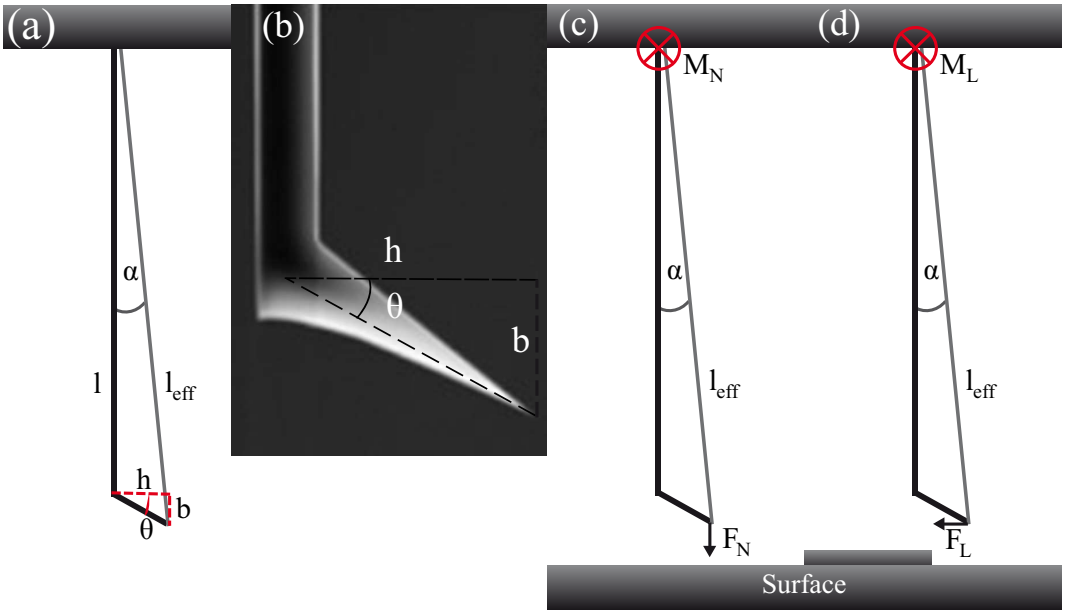

Figure 6.3. Figure (a) shows the schematics of an ATEC Cont lever, with the reduced effective length l_{eff}. Where the advanced tip is shown in the SEM picture, made by (Nanosensors), (b). Schematics (c,d) give the idea of the force induced bending moment on the lever, where the bending moment induced by F_N is effectively reduced compared to F_L.

$$\begin{aligned} b &= h \cdot \tan(\theta) \\ \alpha &= \tan^{-1}\left(\frac{h}{l+b}\right) \Rightarrow \alpha \approx 1.87^\circ \\ l_{eff} &= \sqrt{(l+b)^2 + h^2} \Rightarrow l_{eff} \approx 485\mu m \end{aligned} \tag{6.22}$$

where, b is the addition to the length due to the tip, see fig.: 6.3a. Hence, for non-vanishing angles α, the reduced lever exerts a bending moment on the clamped end for any force acting normal to the surface F_N. The bending moment is then equal to $\mathbf{M}_N = \mathbf{l}_{eff} \times \mathbf{F}_N \Rightarrow M_N = l_{eff} \cdot F_N \cdot \sin(\alpha)$, where bold letters denote vectors. On the other hand, any lateral force will also contribute to the bending moment by $\mathbf{M}_L = \mathbf{l}_{eff} \times \mathbf{F}_L \Rightarrow M_L = l_{eff} \cdot F_L \cdot \cos(\alpha)$, see fig.: 6.3 c,d. If the relation $|M_N| = |M_L|$ holds, we can compare the forces:

$$\begin{aligned} F_N \cdot l_{eff} \cdot \sin(\alpha) &= F_L \cdot l_{eff} \cdot \cos(\alpha) \\ F_L &= F_N \cdot \left(\frac{h}{l + h \cdot \tan(\theta)}\right) \Rightarrow F_N \cdot 0.033 \end{aligned} \tag{6.23}$$

For the given numbers we obtain $\tan(\alpha) = 0.033$, meaning that the sensitivity to normal forces is reduced compared to the lateral, due to geometrical reasons. In addition, this is valid for angles $0^\circ < \alpha \leq 45^\circ$, while angles $\alpha < 45^\circ$ reduce the lateral sensitivity. In the limit of $\alpha = 90^\circ$ we obtain the sensitivity of a normal geometry, while the limit of $\alpha = 0^\circ$ would result in the symmetric cantilever case, which was discussed previously. Further, we can now deduce the dynamic behavior of the tip, in case of a resonantly driven motion.

6.3.2 Cantilever dynamics

When the cantilever is now resonantly driven, the motion of the tip apex will follow a trajectory of an arc with the radius of the effective tip length l_{eff}. While the read out of the beam deflection detection system is done on the backside of the lever itself. The tip apex motion has an offset compared to the zero crossing of the cantilever by the angle α. Therefore, we easily see that the tip motion is not symmetric and we have to consider a perpendicular variation dz in addition to the lateral motion dx, which scales with the oscillation amplitude, see fig.: 6.4(a,b).

To determine the dx, dz variation of any amplitude, we use straightforward the relationship of the unit circle, with the lever clamping at the origin and the tip apex is following an arc. Thus, for a given lateral amplitude A_L, we find a normal amplitude component A_N as the following:

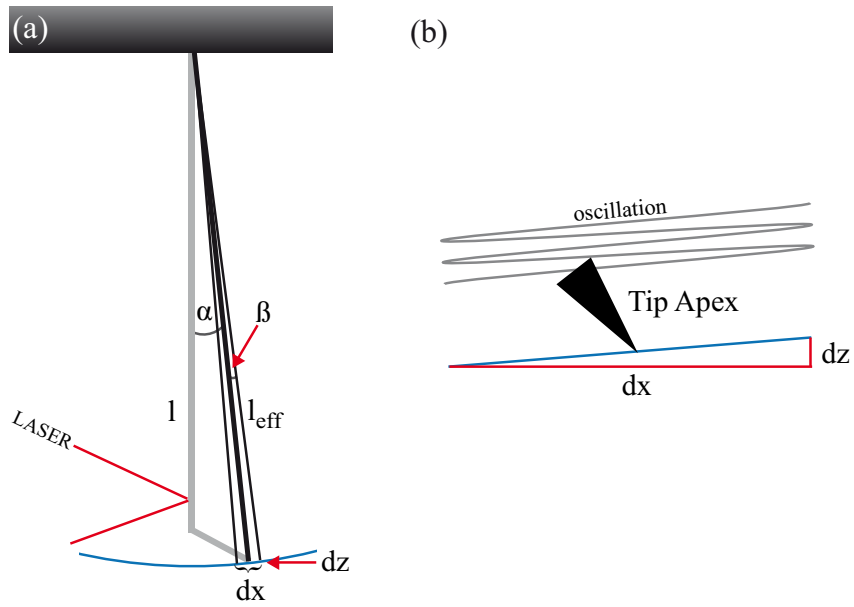

Figure 6.4. In case of a resonantly driven lever, the beam detection read out is done on the backside of the lever, which oscillates through the zeros, in a x-z coordinate system. However, the oscillation amplitude is small compared to the tip height. Therefore, the tip apex is following an arc trajectory, with the radius of the effective length. The tip apex has an offset towards the beam, due to the tip height and advancement, which can be determined by the angle α. Thus, it is clear, since the oscillation amplitude introduces a motion around $\alpha+\beta$, with $\beta \ll \alpha$, that the tip motion is not symmetric in a single oscillation. Thus, we have to consider a small non-vanishing normal variation dz in addition to the motion in parallel to the surface dx, see (b).

$$
\begin{aligned}
A_L &= l_{eff} \cdot (\sin(\alpha+\beta) - \sin(\alpha-\beta)) \\
A_N &= l_{eff} \cdot (\cos(\alpha+\beta) - \cos(\alpha-\beta))
\end{aligned}
$$

$$
\begin{aligned}
\Rightarrow A_L &= l_{eff} \cdot (\sin(\alpha)\cos(\beta) + \sin(\beta)\cos(\alpha) - \sin(\alpha)\cos(\beta) + \sin(\beta)\cos(\alpha)) \\
\Rightarrow A_L &= 2 \cdot l_{eff} \cdot \sin(\beta)\cos(\alpha) \qquad (6.24) \\
\Rightarrow \beta &= \sin^{-1}\left(\frac{A_L}{2 \cdot l_{eff} \cdot \cos(\alpha)}\right) \qquad (6.25)
\end{aligned}
$$

If we assume now the specifications of the above mentioned cantilever, we find for a lateral amplitude of $A_L = 5nm$ and accordingly a normal oscillation amplitude of $A_N = 0.206nm$. This relationship between the amplitudes is fixed for the fundamental resonance. However, this normal amplitude is not negligible, further we want to emphasized that it is important here, **not** to assume the oscillation to be perfectly parallel aligned to the surface. Even thought, that the angle $\alpha \sim 2°$. Due to the high sensitivity to forces, the small dz variation gives still a significant influence to the measured frequency shift. Nevertheless, the normal oscillation arises from the motion on an arc trajectory. Thus, any higher resonance of the lever favors the normal component, due to change of the oscillation node of the lever, which decreases

the effective length and therefore reduces the radius of the arc.
Let us briefly mention, how to calculate the nodes of the higher resonances. This is done by taking the beam equation into account, where lever displacement $z(l)$ is calculated as a function of the length l:

$$z(l) = A \cdot \left[(\cos(\kappa\ l) - \cosh(\kappa\ l)) + \frac{D'}{B'}(\sin(\kappa\ l) - \sinh(\kappa\ l)) \right] \stackrel{def.}{=} 0 \tag{6.26}$$

where A is the amplitude and κ, $\frac{D'}{B'}$ are the following for the first four resonances:

$$\kappa \Rightarrow \{1.875,\ 4.694,\ 7.855,\ 10.996\} \tag{6.27}$$

$$\frac{D'}{B'} \Rightarrow \{-0.7341,\ -1.0185,\ -0.9992,\ -1\} \tag{6.28}$$

From the equation 6.26 with the values of 6.27 and 6.28 we get the node positions of the beam by finding the zero crossings. The node positions for the three first higher resonances are:

$$\frac{l_{node}}{l} \Rightarrow \{0.7833,\ 0.8668,\ 0.9285\} \tag{6.29}$$

Using the node positions of the higher resonances to determine the z component shows, that the z oscillation amplitude increases for higher flexural modes. The relationships of A_z/A_x for the four resonances are then:

$$\frac{A_z}{A_x} \Rightarrow \{0.0413,\ 0.1513,\ 0.2115,\ 0.2993\} \tag{6.30}$$

This shows, that higher resonances have larger amplitudes in the direction normal to the surface and therefore normal forces influences the frequency shift accordingly to the equation 6.7.

6.3.3 Frequency shift in the pendulum geometry

It was shown in the section 6.1 that the resonantly driven cantilever exerts a frequency change due to the interaction force, see eq.: 6.7. Here, we want to extend the equation towards the fact, that the frequency shift in pendulum geometry is influenced by both force components, lateral and normal.
It is always possible to split force components into their unit vectors, given by the reference system. From the fact that these unit vectors are orthogonal to each other. It is allowed to treat these force components independently and adding them up to the total measured frequency shift $\Delta f_{total} = \Delta f_L + \Delta f_N$, where the amplitudes and force sensitivities are taken into account as the following:

$$\begin{aligned} \Delta f_{total} &= \Delta f_L + \Delta f_N \\ \Rightarrow \Delta f_L &= \frac{f_0}{\pi A_L k} \int_0^{2\pi} \sin\phi \cdot F(x_0 + A_L \sin(\phi), z_0) \cdot \cos(\alpha) d\phi \\ \Rightarrow \Delta f_N &= \frac{f_0}{\pi A_N k} \int_0^{2\pi} \sin\phi \cdot F(x_0, z_0 + A_N \sin(\phi)) \cdot \sin(\alpha) d\phi \end{aligned} \tag{6.31}$$

where the factors $\sin(\alpha)$ and $\cos(\alpha)$ are the force sensitivity reductions for the normal and lateral components, respectively. These equations 6.31 hold for higher resonances as well. Since the normal amplitude increases for higher flexural modes, we deduce that the normal force has a larger influence on the measured frequency shift.
In addition, in case of a symmetric lever, where the tip is an arrow along the lever, the change of the normal component vanishes over the oscillation cycle. Since, $\alpha = 0°$ and the frequency shift is dominated by the lateral force contribution. Further, in the limit of $\alpha = 90°$, the lateral component vanishes, and the equation 6.31 reduces to 6.7.
To test the assumptions towards the actual measurements, we conducted simulations on a toy-model. Where we build up a static snapshot of a force field in the x, z-direction originated from a base of atoms.

6.4 Simulating a force field to obtain a frequency shift map

The relevant force in AFM was discussed in chapter 3. Since, the forces cannot be added up, we start with potential fields U_i from single atoms and take the sum over all potentials $U_{tot} = \sum_i^N U_i$ and use the identity $F_{tot} = -\nabla U$ to get the force field. Where U_i is also the sum of the potentials originating from the Lennard Jones, van der Waals and electrostatic potential, $U_i = U_{LJ,i} + U_{vdW,i} + U_{el,i}$. Resulting in a potential on a grid point for one single atom:

$$U_i(\mathbf{r}) = -4\epsilon \left[\left(\frac{\sigma}{\mathbf{r}}\right)^{12} - \left(\frac{\sigma}{\mathbf{r}}\right)^{6} \right] - \frac{H \cdot R}{6 \cdot \mathbf{r}} - \pi\ \epsilon_0 \frac{R^2}{\mathbf{r}} \cdot \left(U_{bias} - U_{CPD}\right)^2 \tag{6.32}$$

where $\mathbf{r}$ is the distance between tip and atom, ϵ the potential depth of the short range force, σ the equilibrium distance, H the Hamaker constant, R the tip radius, ϵ_0 the permittivity constant, U_{bias} the applied voltage across the tip sample junction and U_{CPD} the contact potential of the material.
The equation 6.32 shows already, that the LJ potential is dominant for small tip sample separations as well as fragile on minor changes of the parameters, due to the high power-law decay. The attractive term with the $6th$ power determines the local variation in the force, which results in the atomic resolution for AFM. Therefore, high resolution is only achievable in the last few angstroms of the tip sample junction. Further the lateral variation originated from the atoms decay rapidly, leading to a homogeneous force field without a lateral component, see fig.:6.5
The lateral component vanishes for a flat surface, for distances larger than the decay length of the short range force. This holds for any atomically flat infinite surface with no additional impurities. However, if an atomically high step edge is introduced, lateral force variations occur, due to the abrupt change at the edge, see figure 6.6.
The figures 6.5 and 6.6 were simulated by positioning one atom and calculating the potential, eq.: 6.32, for each point on the simulation grid. All calculated potentials were summed up and derived accordingly to the identity $F_{tot} = -\nabla U$. Each graph consists of 1000×3000 grid points, while the spacing between the grid point was varied, between $30pm$, $15pm$, $7.5pm$, $2.5pm$ for 6.5 and 6.6 (a,b), (c,d), (e,f), (g,h) accordingly.

For the flat surface simulation, four layers of 1100 atoms each, were calculated with a VAN DER WAALS radius σ_{cu} of copper, according to literature values. The Hamaker constant was assumed to be $H = 1.2 \cdot 10^{-19} J$ [19,37,53], with the tip radius $R = 15nm$, the permittivity constant is $\epsilon_0 = 8.8 \cdot 10^{-12} F/m$, while the electrical potential was assumed to be zero $U_{bias} = 0V$ and only the contact potential difference was taken into account with $U_{CPD,Cu} = 0.4V$.
With this we obtained a pseudo realistic force field, with no edge effects of the simulation box. The parameters mentioned above, are chosen to match the force given by the experiments in literature. Hence, the goal was to achieve a static pseudo realistic picture.
In case of the stepped surface, a bilayer of 550 atoms each, was placed at the origin, to obtain a lateral force on top of the surface. The only difference from the previously simulated system is a new VAN DER WAALS radius σ_{NaCl} matching the one of sodium chloride, and the contact potential of $U_{CPD,NaCl} = -0.6V$.

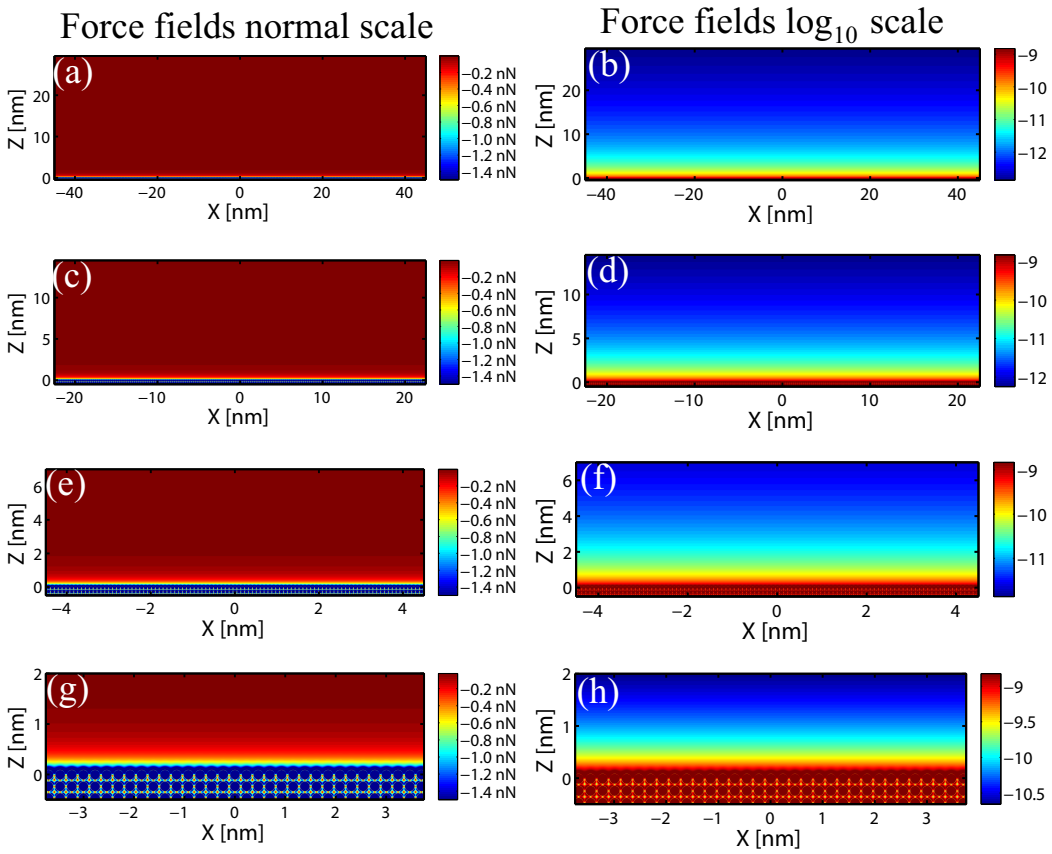

Figure 6.5. The following graphs show the simulated force fields of a flat, perfect surface. The left side is the normal scale of the force, while the right shows the logarithmic scale, for enhanced visibility of the force decay. In both columns no lateral force exists, until the short range force variations dominate. Each graph shows the same surface with just smaller dimensions and decreased grid size. Simulation consists of four layers of atoms with 1100 in each layer, to avoid edge effects of the force field. The simulation box has a $x-z$ grid of 1000×3000 points. The grid spacing is $30pm$, $15pm$, $7.5pm$, $2.5pm$ for (a,b), (c,d), (e,f), (g,h) accordingly.

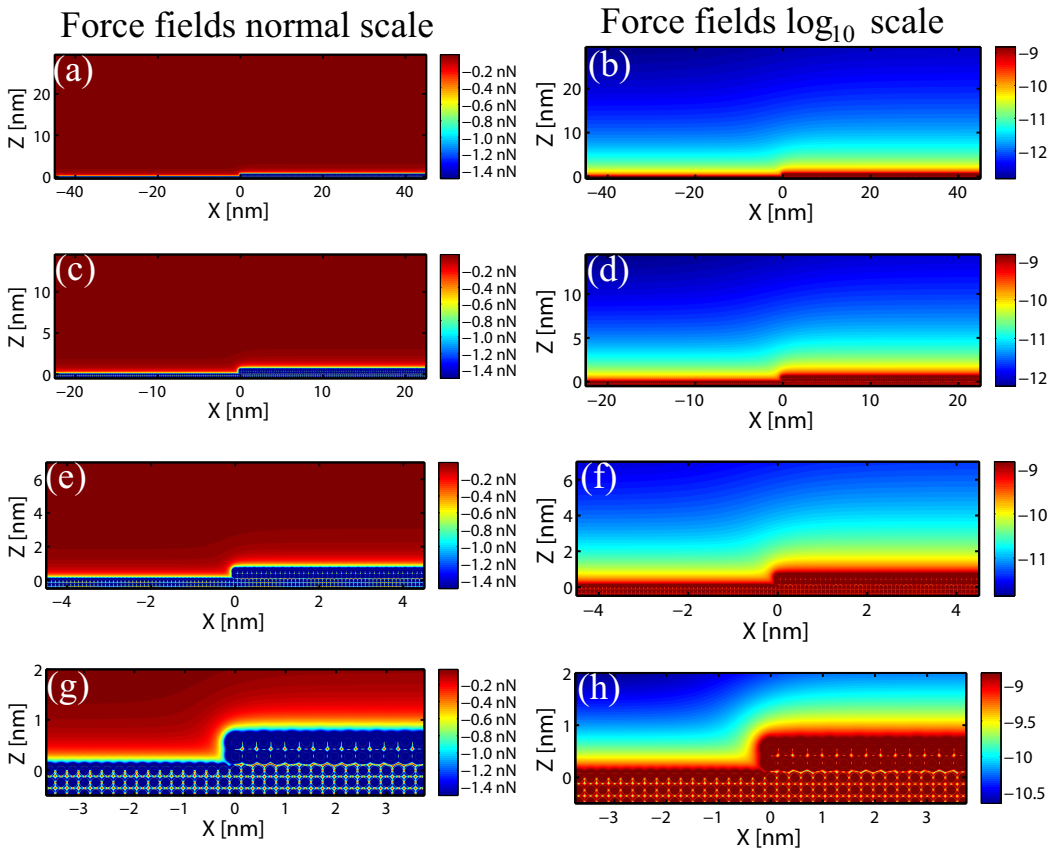

Figure 6.6. In this figure the simulations show a force field with the same parameters of figure 6.5 and an additional bilayer of an ionic island. For the ionic surface the van der Waals radius of $Na - Cl$ was chosen. The left and right column show again the normal scale and the logarithmic scale of the same force fields to enhance the visibility. In the logarithmic scale one nicely recognizes a force gradient in the z-direction, on top of the step at the origin ($x = 0$). The step edge creates a lateral force, which extends several tenth of nanometer out of the surface. Simulation consists of four layers of atoms with 1100 in each layer, to avoid edge effects of the force field. In addition, a surface bilayer was added to create a step edge, with 550 atoms in each layer starting from the origin. The simulation box has a $x - z$ grid of 1000×3000 points. The grid spacing is $30pm$, $15pm$, $7.5pm$, $2.5pm$ for (a,b), (c,d), (e,f), (g,h) accordingly.

The resulting force fields are presented on the figures 6.5 and 6.6. On the left side the actual force in nano-newton nN is shown, while the right side of both figures are the logarithm of the force to show the decay in space. Further, one notices easily, that the stepped surface introduces a lateral force, which extends several tenth of nanometer out of the surface plane, as well as away form the step itself. There the logarithmic scale is more suitable to see this effect, see figure 6.6 (b,d,e,f).
It needs to be emphasized, that these simulations are toy models to create a pseudo realistic force field to roughly obey the demands of this study. Since, we are interested in the contrast mechanism of the pendulum AFM, where the geometry influences the measured frequency shift signal. This simulated force field lacks several aspects of a more sophisticated approach, such as Molecular Dynamics simulation. Since this

simplified model calculates the interaction between a tip and the atoms only, it is rather coarse and leads to an overestimation of the force field. Furthermore, it does not allow motion or relaxation of the atoms, nevertheless, for our demands this study is sufficient enough.
Further, we want to test the derived equation 6.31, whether it can explain the measured frequency shift and therefore the topography, **or not**. Thus, an additional simulation was performed, which integrates lateral force over one oscillation in the x direction and adds it to the integral of the vertical force in the same oscillation cycle. This results in a calculated frequency shift for one point of the grid.
This calculation was then carried out for each point of the grid, to result in a $2D$ map of the expected frequency shift for the asymmetric cantilever. This df-simulation was performed on the flat and the stepped force fields, seen in figures 6.5(c), 6.6(c). Figure 6.7 is divided in two columns and also two sections. The left column shows the calculated frequency shift of the flat surface and the right one for the stepped. In addition, the dependence of the frequency shift was simulated for the first and second flexural resonance, see 6.7 (a-d) and (e-h) accordingly. All simulations were carried out with the same lateral amplitude, to gain the possibility of comparison. The difference between the first and second resonance arises in the larger amplitude for the normal oscillation, as mentioned in eq.: 6.30, as well as the higher flexural spring constant of the second mode.
However, the contour plots 6.7(c, f) show clearly, that the fundamental mode of oscillation has a larger sensitivity to the forces, since the value of $\Delta f_{1st} = -1Hz$ is already reached at larger separation distances, compared to the second mode. Therefore, we can state, that the larger normal oscillation of the second mode, which should result in a larger contribution to the frequency shift, is compensated by the higher effective stiffness.
For the stepped surface, a dip and a protrusion is seen in the constant frequency shift contour, 6.7(d, h). The minimum of the dip becomes sharper in shape and decreases in lateral distance from the step edge for more negative frequency shifts (visual guidance of the minimum is given by the red dotted line). While the protrusion decreases in relative magnitude and lateral separation distance to the edge. The features are more pronounced for the first mode compared to the second.
The "wiggling" (protrusion and dip) in the constant frequency shift contour is the direct result from the lateral force contribution, which adds up to the frequency shift. Since the lateral contribution is more dominant for the first mode than for the second mode, we expected a more pronounced "wiggling" for the fundamental mode.
The simulation shows, that the second resonance, is less affected by the lateral force influence. This is again, due to the higher spring constant of the second flexural resonance. Leading to the assumption, that the second resonance measures for a constant frequency shift a more accurate replica of the topography underneath. Further, we can assume a larger stability of the topography measurements for the second resonance.
One open question remains, what is the influence of the amplitude A_L for the measured topography? To answer this question, we performed a similar Δf calculation for a lateral Amplitude of $A_L = 15nm$. The results are shown in figure 6.8. The figure is divided in two columns, where the left side shows the graphs for an amplitude of $A_L = 2nm$ and the right side shows for the results for $A_L = 15nm$. Each calcu-

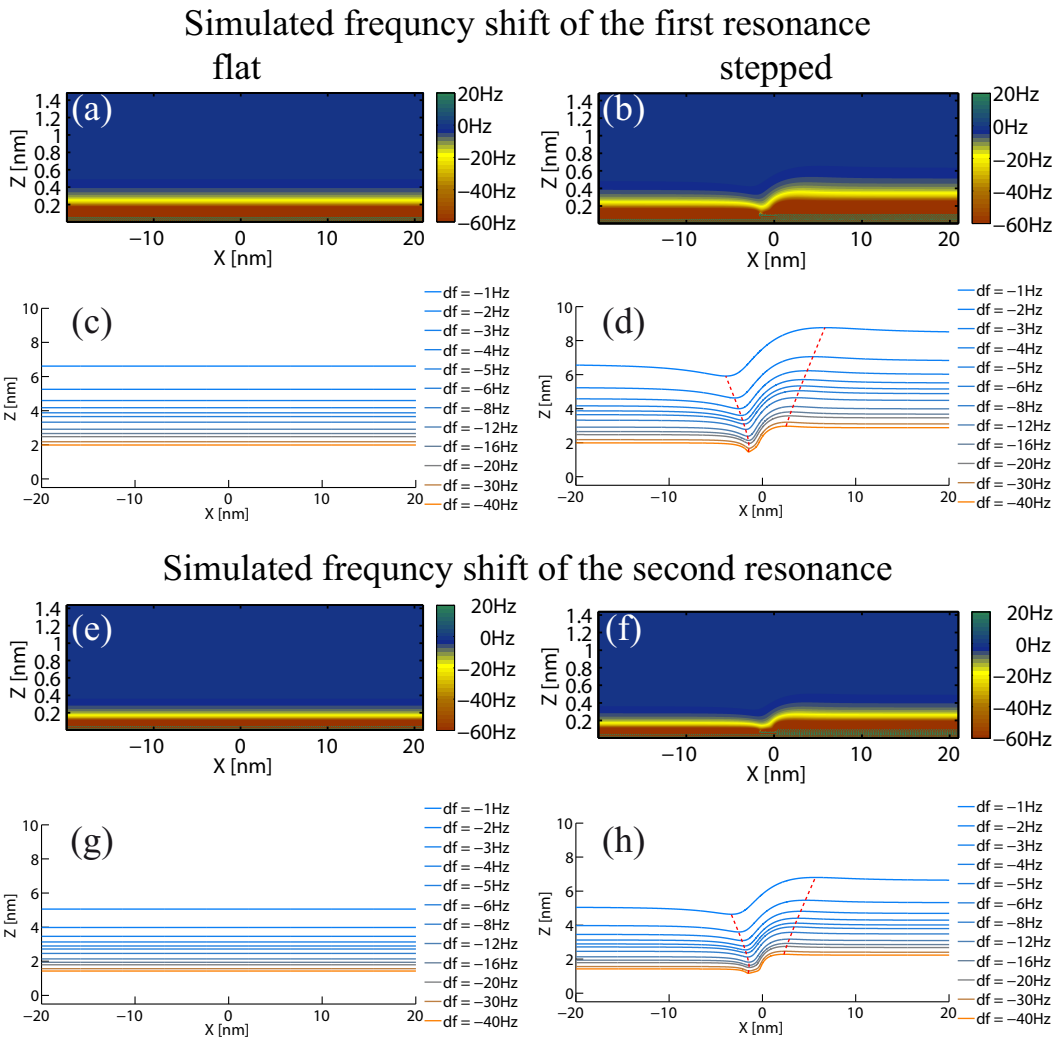

Figure 6.7. The set of figures show the simulated frequency shift of the previously shown force fields, 6.5(c), 6.6(d). The left column is the calculation for the flat surface, while the right column is the stepped surface. The graphs show always a $2D - \Delta f$-map and a contour plot for constant Δf below, for the flat and stepped surface, as well as first and second resonance. The lateral amplitude of both resonances was the same $A_L = 2nm$, while the normal amplitude differs according to equation 6.30. In addition, the spring constant k is stiffer for the second mode. Furthermore, the contour plots of the stepped surface show clearly a dip in the separation distance just before the step and a protrusion after the step. These becomes more pronounced with more negative frequency shifts. The minimum of the dip and the maximum of the protrusion is indicated with the dotted red line. For these simulations we used the parameters $f_{1st} = 14000Hz$, $k_{1st} = 0.23N/m$, $A_{L,1st} = A_{L,2nd} = 2nm$, $\alpha_{1st} = 2.36°$, $f_{2nd} = 87000Hz$, $k_{2nd} = 9.6N/m$, $\alpha_{2nd} = 8.6°$, according to a usual **ATEC Cont** lever.

lation consists of a $2D - \Delta f$ map and below a contour plot of constant frequency shift. In addition, the dependence of the first mode is compared to the second one as well. Since the oscillation amplitude of $15nm$ was to large for the simulation box of 6.6(c), we performed the calculation on the force field 6.6(a). Since, the force is

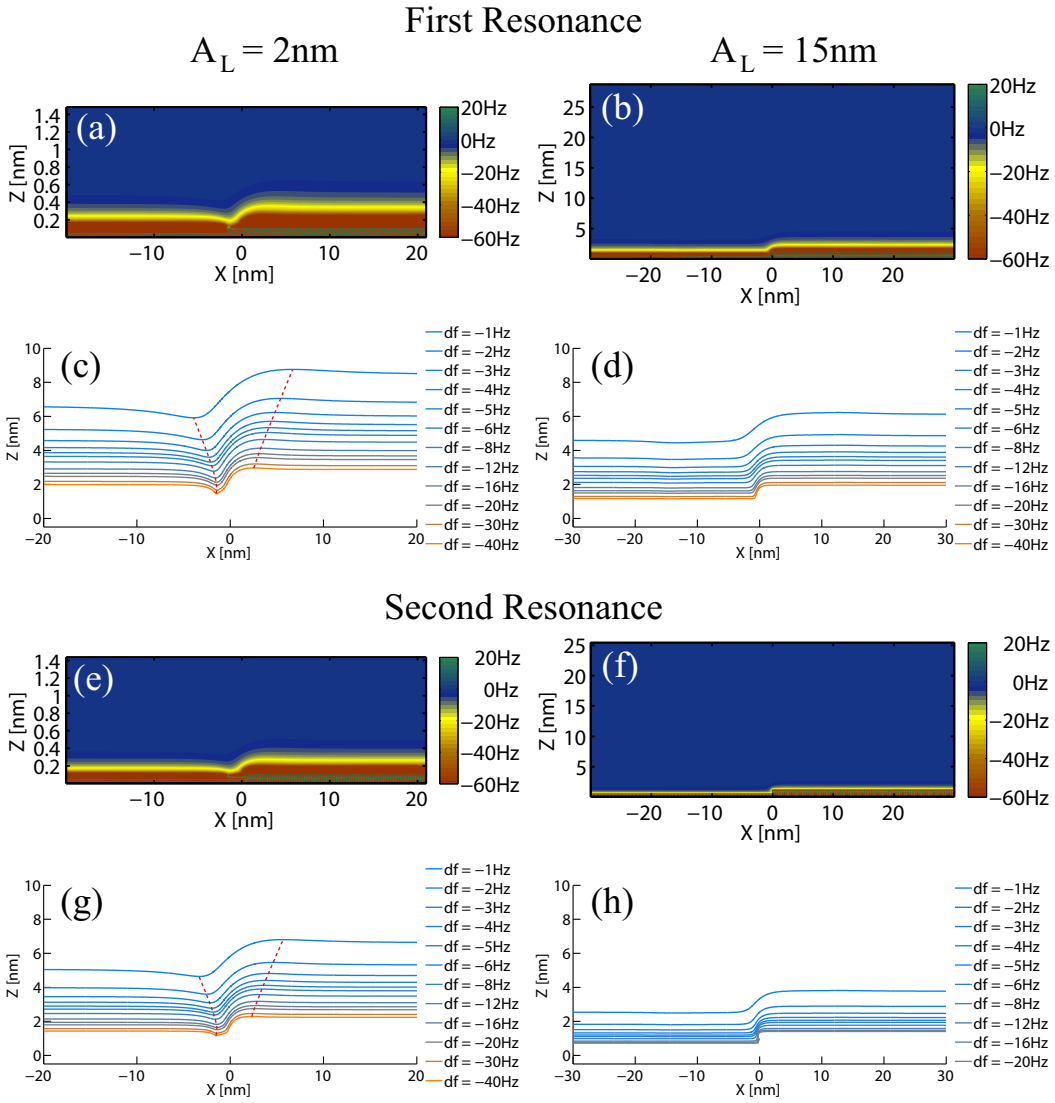

Figure 6.8. The set of figures show the simulated frequency shift of the previously shown force fields, 6.6(a), 6.6(c). The left column is the calculation for the stepped surface with an amplitude of $A_L = 2nm$, while the calculations of $A_L = 15nm$ are shown in the right column. The graphs show always a $2D - \Delta f$-map and a contour plot for constant Δf below, for both amplitudes, as well as first and second resonances. For these simulations we used the parameters $f_{1st} = 14000Hz$, $k_{1st} = 0.23N/m$, $A_{L,1st} = A_{L,2nd} = 2nm$ $(leftside)$, $A_{L,1st} = A_{L,2nd} = 15nm(rightside)$, $\alpha_{1st} = 2.36°$, $f_{2nd} = 87000Hz$, $k_{2nd} = 9.6N/m$, $\alpha_{2nd} = 8.6°$, according to an usual **ATEC Cont** lever.

exactly the same for the same region, it is certain, that we do not introduce errors by choosing the different simulation box.
Comparing the results of the amplitude dependence, one easily sees that the small amplitude is more sensitive to the forces and generates a frequency shift of $\Delta f = -1Hz$ already at larger separation distances. This holds for both resonances. Furthermore, one striking fact is, that the lateral force contribution is strongly reduced by the large amplitude. The "wiggling" is somewhat suppressed for the first reso-

nance and it is not visible for the second mode of oscillation. No dip or protrusion was found by means of calculating the minimum or maximum of each contour line. Since the normal amplitude rises in magnitude accordingly to the lateral, we know that the frequency shift is also stronger influenced by the normal component. However, it seems that the lateral force of the step is averaged out during one large oscillation cycle. While the amplitude for the normal direction is on the orders of $A_{N,1st} = 0.6nm,\ A_{N,2nd} = 2.3nm$ it is still small enough to avoid averaging to zero. Nevertheless, the contour plots show a significant sensitivity loss to normal forces for both amplitudes, due to the time averaging of the oscillations.
The main goal of using large amplitudes, lies in the fact, that the lateral contribution to the measured Δf vanishes. Thus, a stronger correlation of the measured frequency shift to the actual topography exists. This fact is more desired for practical application, since one can determine easier the surface topography from the performed measurements.

6.4.1 Comparison of the Simulations to the Measurements

We performed measurements on two different sets of samples, to verify the derived theory and the prediction of the simulations. Firstly, we investigated the copper - sodium - chloride system as it was simulated above. For a bilayer step and a lateral oscillation amplitude of $A_L = 3nm$, see fig.: 6.9 (a, b), we measured the "wiggling", due to the influence lateral force. Before the step edge, the characteristic protrusion is seen, while after the step the predicted dip is seen as well in the profile. The second "bump" after the step is due to the uncompensated electrostatic force, since the contact potential difference between NaCl and Cu is $U_{CPD} \sim 1V$. The AFM tip apex is averaging the influence of the electrostatic force over a wide range. In the simulations the tip was treated as a point like particle with no spacial extension.
To overcome the issue of the work function difference, which is a material property, the second measurement was performed on **H**ighly **O**riented **P**yrolytic **G**raphite (**HOPG**). The sample is made of one material with the same work function regardless of the step. Again a lateral oscillation amplitude of $A_L = 3nm$ was used in the second mode. In the graphs of figure 6.9 (c, d) a bilayer step is shown, where the characteristic protrusion is measured immediately before the step edge. However, the dip after the step is absent in the profile, which can have several origins. On the one hand, the tip apex averages the lateral force contribution to zero, while oscillating on the lower side of the step. On the other hand, it could originate from the decreased lateral force, due to the absence of the electrostatic force.
However, the derived formalism and the supporting simulations seem to verify the sensing mechanism of the pendulum geometry AFM. Thus, from the understanding of the sensing mechanism, we are able to deduce parameters of the further measurements, with high fidelity. This gives us a good head start to perform more challenging measurements.

6.5 Kelvin Probe Force Microscopy

The energy to extract an electron from the Fermi level of a surface out into the vacuum, is the so called work function Φ. The amount of work spent on a particular

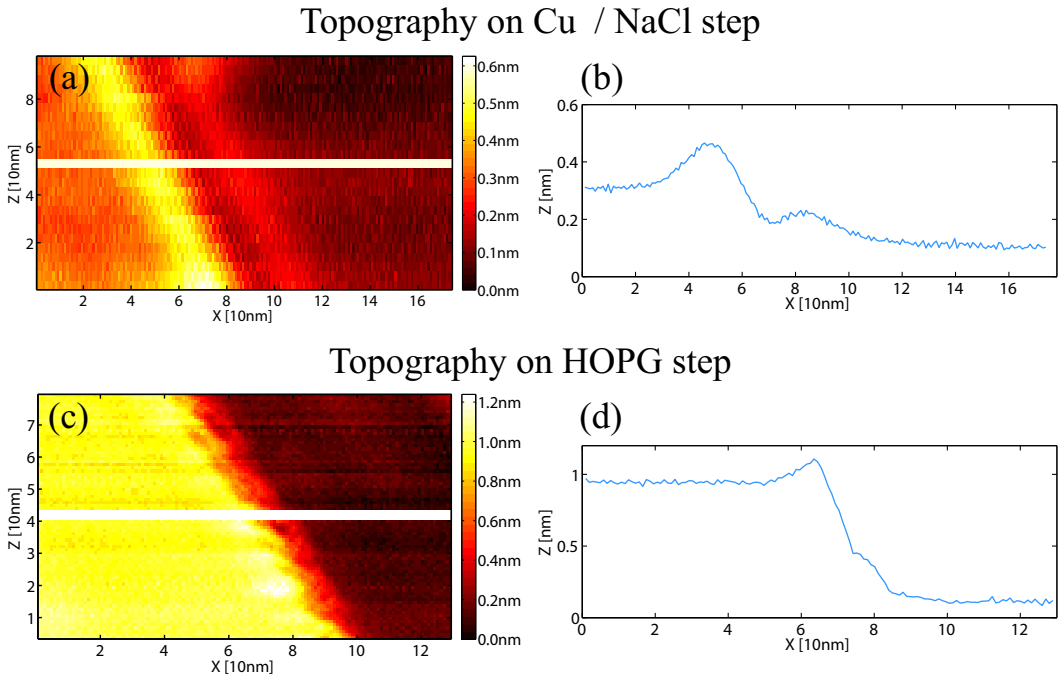

Figure 6.9. The following graphs show a step in the topography image and a line scan besides it (white line indicates the position) of two different samples. The step on a copper substrate with a bilayer of NaCl, as well as on HOPG, both show the protrusion immediate before the step edge. However, the dip after the step is only visible on the Cu/NaCl topography, which can be related to the larger lateral force. Since NaCl and Cu have a work function difference of $U_{CPD} \sim 1V$, and at the step edge the potential difference can not be nullified. In the case of HOPG, we expect a constant work function and therefore no additional lateral force, which reduces the lateral contribution to the frequency shift. Image parameters: $f_{2nd} \sim 87000Hz$, $k_{2nd} \sim 9.5N/m$, $A_{L,2nd} \sim 3nm$, $\Delta f \sim -15Hz$, recorded by an usual **ATEC Cont** lever.

electron to leave the surface, is a material property, since it depends on the element, its crystallographic arrangement and the surface reconstruction. This barrier, which prevents the electrons from eventually leaving the bulk material, is called the vacuum barrier E_V.

The most accurate way to determine the work function of a pure underlying material, was explained by the Nobel prize honored Albert Einstein with the photoelectric effect. Where a photon with a certain energy $E_p = h \cdot \nu$ hits the surface atom, and gets absorbed. If the absorbed energy is sufficient to give a single electron the energy to overcome the vacuum barrier, then it will leave the surface. This electron can be detected and its kinetic energy is then $E_{kin} = E_p - E_{bind} - E_V$. If the electron got emitted from the Fermi level, it is assumed that the binding energy $E_{bind} = 0$, which determines exactly the work function.

"OK, the fun is out, everything is already known." - Not at all. The experimental technique mentioned above is **P**hoton **S**pectroscopy (PS). It is very accurate in determining the global work function, however, it lacks the spacial resolution for blended material or todays semiconductor industry, which operates in a range of a few nanometers. Since, the incident beam can only be focused to a few tenth of

micros in normal setups and down to several microns in sophisticated experiments. In order to overcome issue of the spacial resolution, a different approach is chosen and a rather old one as well, the Kelvin probe method, named after Sir William Thomson a. k. a. Lord Kelvin. Here, the working principal of determining the work function is different. The original proposed method uses a voltage U applied to a plate capacitor with a known material and surface area, which is oscillating with a frequency ω on top of a second material. The resulting capacitance change ΔC induces a time dependent current $I(t)$, according to [56]:

$$I_{CPD}(t) = U\ \omega\ \Delta C\ \cos(\omega t) \tag{6.33}$$

The voltage $U = U_{dc} - U_{CPD}$ can be nullified by applying an addition electrical potential on the plate until the contact potential is reached and the electric field in the plate capacitor is compensated. Thus the time dependent current is zero as well. If the material work function Φ_p of the probing plate is known, then the determination of the work function Φ_2 of the unknown material is straight forward:

$$U_{CPD} = \frac{\Phi_p}{e} - \frac{\Phi_2}{e} = \frac{\Delta\Phi}{e} \tag{6.34}$$

where e is the elementary charge.
However, the detection of the time dependent displacement current is an issue for small objects, while the electrostatic force associated to the plates, is easily accessible in AFM. Therefore, AFM provides the leverage to overcome the spatial resolution issue and decrease the limit to the atomic scale in *Kelvin Probe Force Microscopy* measurements [56–59].

In KPFM, the tip apex is assumed to be a plate capacitor with a nanometer sized area. It feels the electrostatic force acting between the tip and the sample after they are brought in electrical contact through the voltage source, see fig.: 6.10, due to the alignment of the Fermi level E_F of both materials. This electrostatic force can be compensated by an additionally applied dc voltage U_{dc}, which matches the contact potential difference U_{CPD}.
The electrostatic force acting on the AFM is explained in the section 3.1 and by the equation 3.5. The sensitivity and the experimental technique results from the gradient of the tip-sample capacitor. In KPFM an additional oscillating voltage U_{ac} is applied to the capacitor junction with a frequency ω_{ac} and the resulting modulation of the force is the following:

$$F_{el}(z) = -\pi\epsilon_0 \left|\frac{\partial C}{\partial z}\right| \left(U_{dc} - U_{CPD} + U_{ac}\sin(\omega_{ac}\ t)\right)^2 \Rightarrow F_{el} = F_{dc} + F_{\omega_{ac}} + F_{2\omega_{ac}} \tag{6.35}$$

where each component can be rewritten as:

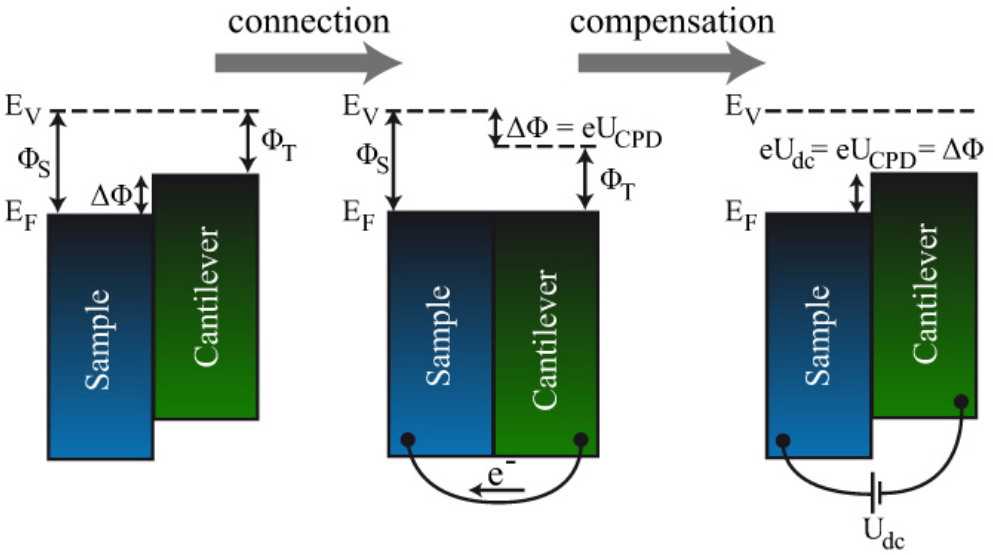

Figure 6.10. The working principal of the KPFM technique is illustrated in this figure. When two surfaces are brought in close contact the vacuum levels E_V aligns. If these materials are brought in electrical contact, their Fermi levels E_F equilibrate, which induces a force. Applying a dc voltage U_{dc}, which compensates the difference in their contact potential U_{CPD}, the electrostatic force is vanishing again. Therefore, the CPD is determined.

$$F_{dc} = -\pi\epsilon_0 \left|\frac{\partial C}{\partial z}\right| \left[\frac{1}{2}\left(U_{dc} - U_{CPD}\right)^2 + \frac{U_{ac}^2}{4}\right], \tag{6.36}$$

$$F_{\omega_{ac}} = -\pi\epsilon_0 \left|\frac{\partial C}{\partial z}\right| \left(U_{dc} - U_{CPD}\right) U_{ac} \sin(\omega_{ac}\, t), \tag{6.37}$$

$$F_{2\omega_{ac}} = +\pi\epsilon_0 \left|\frac{\partial C}{\partial z}\right| \frac{U_{ac}^2}{4} \cos(2\omega_{ac}\, t) \tag{6.38}$$

where the dc-force component, F_{dc}, contributes to the topography signal, the ac-force component $F_{\omega_{ac}}$ is used to determine the CPD and the $F_{2\omega_{ac}}$ is usually used for capacitance spectroscopy. The modulated force acting on the cantilever can be detected in two different ways. Firstly, by the amplitude modulation, where the modulated frequency of the ac voltage is at a resonance frequency of the detecting cantilever. Here, the force modulation excites the cantilever on its resonance and the dc voltage is varied until the amplitude is zero. Secondly, by the frequency modulated detection, where the alternating electrostatic force is detected by an oscillation in the frequency shift, at the frequency Δf_{ac}. The measured signal was found [56] to be proportional to the force gradient, which can be written as:

$$\Delta f_0 = -\frac{f_0}{2\,k}\frac{\partial F}{\partial z} \tag{6.39}$$

$$\Delta f_0(\omega_{ac}) = \frac{\partial F_{\omega_{ac}}}{\partial z} = -\pi\epsilon_0 \left|\frac{\partial^2 C}{\partial z^2}\right| \left(U_{dc} - U_{CPD}\right) U_{ac} \sin(\omega_{ac}\, t) \tag{6.40}$$

The frequency modulated KPFM is sensitive to the gradient of the electrostatic force. In principal, we can form an analogy to a radio antenna, lets assume our cantilever oscillating on top of a surface is the antenna, with its carrier frequency (f_0). It has a certain bandwidth $B = f_0 - f_{cutoff}$ around its carrier frequency, which can pick up a modulation signal f_{ac}, which was sent to the ether.
In the case of the radio, a lock-in amplifier is used to track the frequency component f_{ac} and apply a dc-voltage to maximize the signal out of the noise, with the condition $U_{dc} \neq U_{CPD}$. In case of KPFM, the opposite is done. The lock-in amplifier

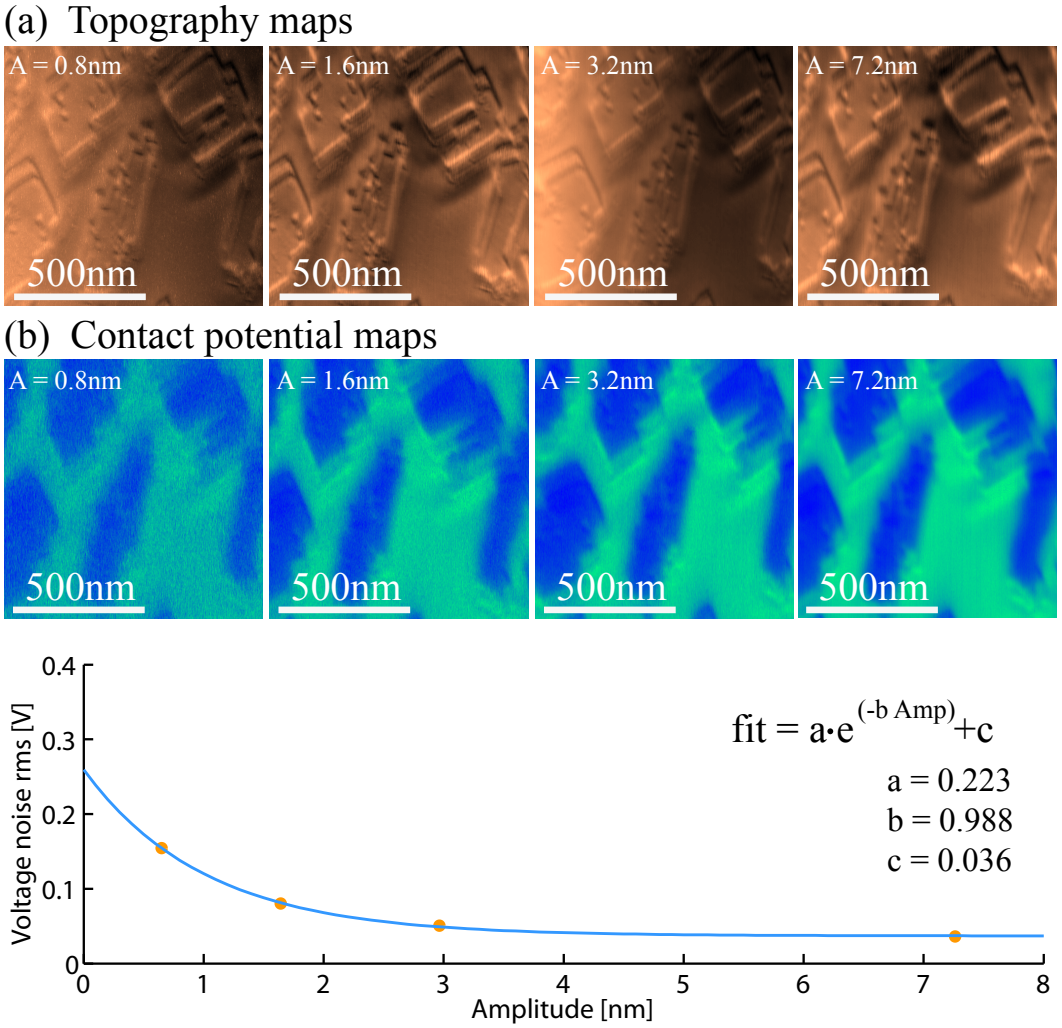

Figure 6.11. Dependence of the CPD noise rms on the oscillation amplitude of the second resonance. Figure row (a) show the topography maps corresponding to the used measuring amplitude A_L. In the row (b) below, the according contact potential maps are shown, measured by the FM-KPFM method. The noise dependence on the amplitude is clearly visible. Where the plot below shows the voltage noise rms of the CPD. The dots are the calculated rms values according to the CPD maps. The power law fit indicates a direct dependence on the amplitude, with $b \sim 1$. The minimum noise level is dependent on the offset c, which is the rms value of the applied alternating voltage, in this case $U_{ac} = 0.05V$.

module together with the Kelvin controller are used to demodulate and minimize the frequency component f_{ac} from the carrier frequency f_0. The demodulation is perfect is the condition $U_{dc} = U_{CPD}$ is reached, however, the noise level of the carrier frequency limits the demodulation of the f_{ac}. Thus, the dc-voltage cannot be accurately determined to compensate the contact potential. Therefore, it is easy to acknowledge, that the sensitivity is determined by the noise level of the force detection F_{min}, see eq.: 4.22. In addition, it is sensitive to the second derivative of the capacitance. Hence, the amplitude of oscillation is the second limiting factor, since the change of the capacitance is due to the time varying distant dependence of the tip sample junction. A series of measurements have been done, to prove the FM-KPFM principal and the noise performance for the pendulum geometry, see figure 6.11. A set of topographical images were taken, see row 6.11(a), with four different amplitudes. All show the same area of a copper surface with evaporated sodium chloride islands, recorded with the second resonance and lateral amplitudes of $A_L = \{0.8nm,\ 1.6nm,\ 3.2nm,\ 7.2nm\}$. The contact potential was determined and compensated simultaneously to the acquired topography, see row 6.11(b). From the obtained contact potential maps, we determined the **r**oot-**m**ean-**s**quare (rms) CPD voltage noise amplitude. In the plot below the images, the rms values have been plotted and fitted with a power law dependence, $a \cdot e^{-b \cdot A_L} + c$. The fit indicates that the rms noise level drop is exponentially dependent on the amplitude, since the fitting parameter $b \sim 1$. Furthermore, the voltage noise limit is dependent on the offset value c, which corresponds to the rms value of the applied alternating voltage $U_{ac} = 0.05V \Rightarrow U_{rms,\ ac} = 0.035V$. Therefore, if measurement amplitude is beyond $A_L > 5nm$, the limiting factor of the noise level is the applied alternating voltage. In pendulum geometry, the alternating voltage U_{ac}, can be strongly reduced due to the high force sensitivity. Hence, the pendulum AFM is an excellent KPFM probe. Furthermore, the sensitivity to the contact potential and the compensation in the FM-KPFM mode is enormously accurate, since the noise level of the obtained voltage maps is limited by the alternating voltage. For the standard measurements seen in figure 6.11, it is possible to work with an applied voltage $U_{ac} = 0.05V$, which is almost two orders of magnitude below the values $\sim 1 - 3V$ used in the normal AFM geometry [56].

Having shed light on the detection and contrast mechanism of the pendulum AFM, we discussed all the necessary tools to conduct the further measurements. Thus, we can investigate non-contact friction in the following chapter on a reference system, like copper - sodium chloride. Then, moving on to the niobium-diselenide ($NbSe_2$), where a rather special phase transition, like the **C**harge **D**ensity **W**ave transition (CDW), changes the character of non-contact friction drastically. Further we come to the last chapter of this theses, with strontium titanate ($SrTiO_3$), with two phase transitions, structural and electronic, where also enormous non-contact friction was observed.

7 Our Reference system - Cu/NaCl

The copper sodium chloride sample, acts here as a widely studied reference system [60–73], where a typical and smooth rise in non-contact friction is observed. Nevertheless, it is possible already to study the influence of the slipperiness of vacuum for a metal surface compared to the non-contact friction of a single bilayer of sodium chloride evaporated on top. The Kelvin probe measurements are in this case of major importance, since it provides direct insight in the surface material, due to the contact potential.

7.1 Preparation

First things first - Preparation. In these studies a single crystal of copper, Cu(1 0 0), was used as the substrate. The crystal was introduced and cleaned under UHV conditions, by means of argon sputtering and heat treatment. The argon sputtering, bombards the Cu surface with argon ions, which are accelerated in a static electric field of $U_{sputtering} = 1kV$. The pressure in the preparation chamber is adjusted to $p_{sputtering} = 5 \cdot 10^{-6} mbar$, to have a large sputtering yield, during the $t = 15min$ of exposure. The benefit of this procedure is to remove several layers of contaminants, nevertheless, the disadvantage is the surface roughening.
However, the heat treatment brings the single crystal below its melting point with $T_{annealling} = 770K$, where surface premelting takes place. The roughened topography equilibrates again and forms step edges, due to the surface mobility of the copper atoms. Nevertheless, the equilibration is not the only event, unfortunately the temperature enables bulk diffusion of contaminants, which slowly diffuse to the surface. Therefore, the time of annealing should be short, in this case $t_{anealing} = 15min$. The creation of large copper terraces is influence by the cooling rate. Slower is better, in this case a cooling rate of $r_{cooling} \sim 10K \ / \ min$ was chosen.
The sputtering and annealing cycles need to be repeated several times to achieve large, atomically flat, clean terraces of micrometer size. 15 cleaning cycles are performed from the point of introducing the sample for the first time to the UHV chamber for later measurements. The copper terrace size and contaminant distribution was checked several times, by means of AFM topography measurements, during the cleaning cycles.
After a proper preparation of the copper surface, the sodium chloride (NaCl) was prepared to achieve evaporation conditions. In order to obtain clean sodium chloride, a crucible of $> 99.0\%$ pure NaCl from Sigma-Aldrich was introduced in a Knudsen-cell evaporator to the UHV. Water and other light contaminants of the salt were removed by degassing at high temperatures. The Knudsen-cell was heated by a PID-heater stable at the temperature $T = 630K$ and annealed for $t \sim 36h$. This cleaning treatment reduces any contaminants of the salt to a minimum and the base pressure of the preparation chamber is $p_{cleaning\ NaCl} < 2 \cdot 10^{-10} mbar$ for a degassing

temperature of $50K$ below the actual evaporation temperature.
Further, the deposition rate of NaCl was determined, by heating the Knudsen-cell to the evaporation temperature $T_{evaporation} = 678K$, and the evaporation rate was measured with an Intellimetrics Il 150 Quartz Crystal growth rate monitor with the according calibration factors of the manual of sodium chloride with the density of $\rho = 2.54g/cc$ and acoustic impedance of $5.62 \cdot 10^5 gcm^3 s^{-1}$. The pressure in the chamber raised to $p_{evaporation} = 6 \cdot 10^{-10} mbar$ and the deposited thickness on the quartz crystal was measured for $t = 10min$ to evaluate the deposited thickness per minute.
After determining the deposition time in order to obtain $0.6ML$ of sodium chloride, we evaporated the NaCl on the cold clean copper surface. Further the copper / NaCl sample was annealed at $T = 400K$ for $t = 1h$ to support a proper island growth on the surface of the thermally evaporated sodium chloride film.
The prepared system was then transfered to the microscope chamber and cooled down to $T = 77K$ for measuring non-contact friction.

7.2 Imaging

Imaging the surface is the first step of every further measurement, with it we can determine the success or failure of the preparation procedure and justify the actual position for further spectroscopies. Nevertheless, it was mentioned in the previous chapters that the pendulum geometry isn't a perfect imaging tool. In order to distinguish locally the underlying material of the topography, whether it is copper or sodium chloride, an accompanied Kelving Probe Force measurement is relentless [69]. The material difference is only distinguishable by the contact potential. In the following figure 7.1 a typical topographical image (a) is shown, with its according contact potential map (b). Below each image one finds a cross sections of each. The topography does not reveal the true nature of the surface, due to the contribution of the normal and lateral forces, as we mentioned earlier. Therefore, each step appears not as a step, but rather as it's first derivative. While the contact potential map shows beautifully the chemical contrast, due to the difference in work functions. The vacuum level difference of copper towards highly doped silicon is $CPD_{Cu} \approx +0.4V$, whereas for sodium chloride is $CPD_{NaCl} \approx -0.6V$. Adding them up to the work function delta of the surface material gives $\Delta CPD_{Cu-NaCl} \sim 1V$ [56].
With the capability to distinguish the surface material, it is possible to perform site dependent spectroscopy to determine the effects of the metal/insulator contribution to the non-contact friction. The idea is, whether the dielectric constant and therefore the Joule dissipation mechanism is distinguishable. Since, it was shown by Kumar *et al.* [74] that the capacitance gradient is depending on the dielectric constant, thus the measured CPD. In our case, we want to go one step further and want to observe the difference between the materials in the dissipation mechanism. In order to achieve the goal, spectroscopies on copper and sodium chloride were performed with the fundamental mode of oscillation f_0, since, the sensitivity of the dissipation, eq.: 4.24, and friction coefficient, eq.: 4.25 and 4.6,both depend on the spring constant k, the frequency f as well as the Q-factor Q.

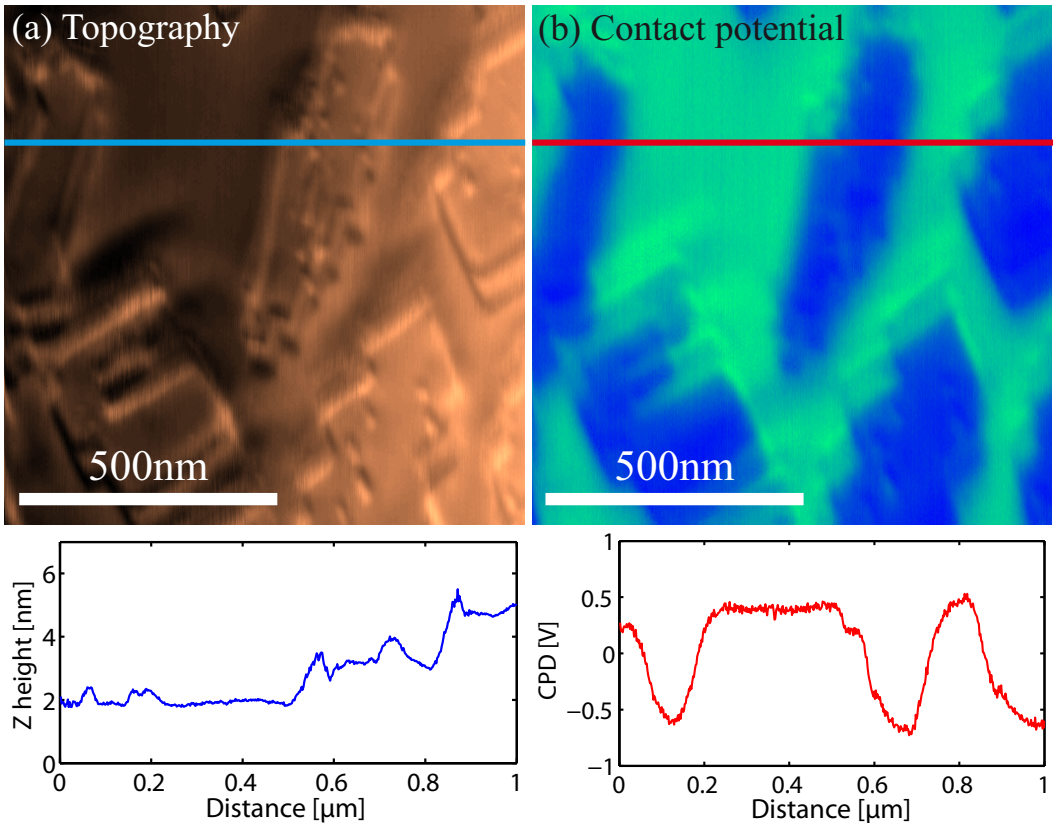

Figure 7.1. The left side, (a), shows the topography with the corresponding line section below. The right side, (b), shows the simultaneously acquired contact potential map, with the according cross section below. While the topography doesn't provide full insight into the local material, one obtains this information through the contact potential map. Image parameters: $f_{2nd} \sim 87kHz$, $A_{2nd} = 7.2nm$, $\Delta f_{2nd} = -6Hz$, $U_{ac} = 50mV$

7.3 Spectroscopy

In the following we performed force-distance spectroscopies with a high z-resolution and a long acquiring time per point to reduce artifacts in the z-dependence as well as controller noise. The typical acquiring time for a complete spectroscopy is in the range of an hour for a three thousand point spectroscopy.
The probe was positioned on top of the copper, where the contact potential was accordingly compensated. Before each spectroscopy the thermal drift and the piezo creep was equilibrated to obtain the highest stability of the measurements. The first resonance was excited at an amplitude of $A_{1st} = 15nm$. After the acquiring the data set on copper, we positioned the probe on top of sodium chloride, with the same settings to maintain comparability.
The figure 7.2 shows the performed spectroscopies. The set shown in 7.2 plots the dissipation for Cu and $NaCl$ islands fo a clean native silicon tip. The inset is the measured frequency shift. The dissipation versus distance is calculated as it was derived by equation 4.24.
The main difference in the spectroscopies is the magnitude of dissipation per cycle.

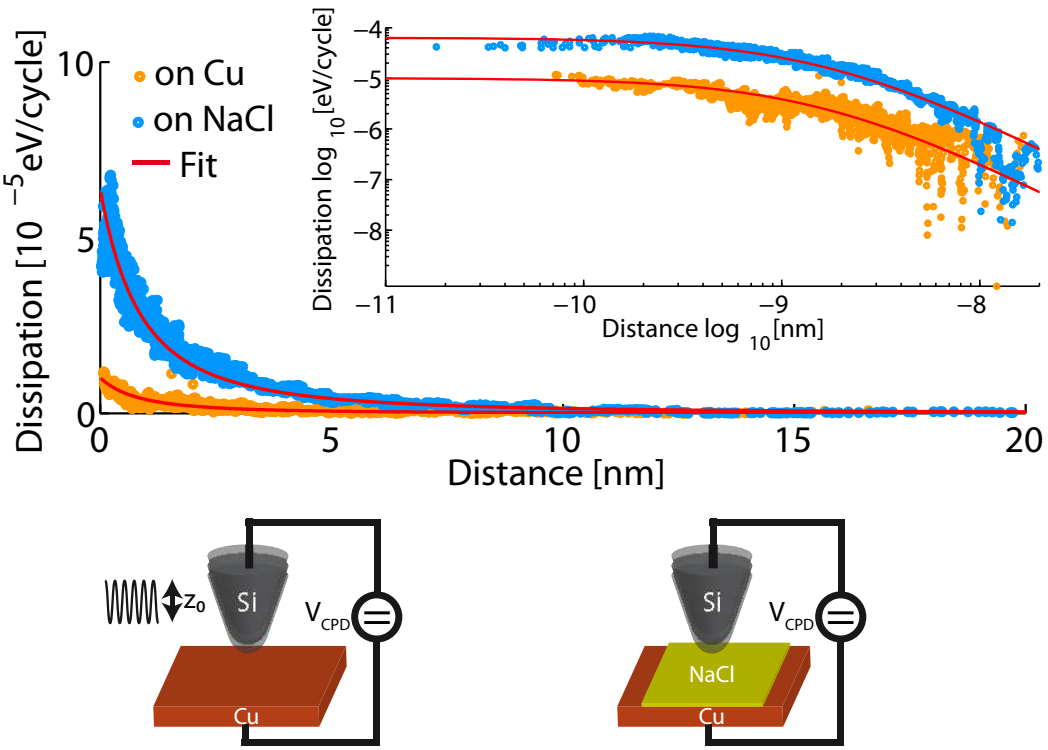

Figure 7.2. Here the spectroscopy experiments are shown. The set consists of two dissipation versus distance curves with a clean silicon tip on copper (orange curve) and sodium chloride (blue curve). The red line is the fit according to the Joule losses 4.34. The inset shows the Δf vs. distance curve. Parameters: $f_{1st} \sim 14kHz$, $A_{1st} = 15nm$, $U_{ac} = 50mV$.

The spectroscopy on copper exerts almost no energy loss of the cantilever, even in close proximity to the surface. Whereas on sodium chloride an elevated dissipation level is measured at large distances of $6nm$.
The explanation of the significant rise in non-contact friction is relative simple to determine. Since, VAN DER WAALS friction is orders of magnitude below the detection limit at separation distances of $1nm$, hence, it can be neglected. Further, adhesive friction force would easily reach the measured magnitude and even above, however, it is restricted to relaxation processes on the surface induced by the short range forces. Thus, it cannot explain the elevated energy loss level at distances of $6nm$.
The stochastic friction is capable the to explain the higher non-contact friction for sodium chloride, since the ionic islands are not perfectly screened by the localized electron density. Hence, the Brownian motion of the ions in their lattice, gives rise to larger force fluctuations. One way to be certain of the origin, would be a temperature sweep, down to $T = 4K$, since the fluctuating force is temperature dependent, see 4.30. The second way to determine the dissipation origin, would be the second set of spectroscopies 7.3, which is explained later.
Last but not least, the Joule dissipation is capable as well to explain the experiments. Here, the important factor is the capacitance gradient of the tip sample junction,

which gives rise to a displacement current in the tip as well as in the surface. The lag of the displacement current compared to the distance dependent electrostatic field arising from the cantilever oscillation, causes a frictional force during the motion.
In case of the copper spectroscopy, a pure metal, with a low defect density and a high electron mobility, shorter delays in the displacement current are expected. In addition, the electron density of copper is more likely to screen the electric field. *Thus, a lower distant dependent non-contact friction would be expected.*
A bilayer of sodium chloride gives rise to a tip sample capacitor system with a dielectric media. Here, the ionic crystal increases the electrostatic field, due to the dipole moment created in the dielectric film. Hence, the dipole relaxation time causes a decreased screening of the electrostatic field, which leads to an increased time delay of the displacement current, that causes an increased Joule dissipation in the cantilever.
In order to confirm the Joule dissipation as the origin of the non-contact friction in this system, we fitted the spectroscopies, see red line in the figure 7.2. By the formalism derived in equation 4.34:

$$\begin{aligned} \langle P_{Joule} \rangle &= \pi \; R_{Si,\; tip} \left(\frac{\partial C}{\partial z} \right)^2 \; U^2 \; A^2 \; \omega^2 \; \frac{1}{e} \\ \Rightarrow \frac{\partial C}{\partial z} &= \pi \epsilon_0 \epsilon_r \frac{R}{z + d_{offset}} \end{aligned} \tag{7.1}$$

where $R_{Si,tip} \approx 10^4 \Omega/cm$ is the resistance of the silicon tip, $U_{ac\ noise} \approx 0.025V$ the ac noise from the compensated KPFM, $A = 15nm$ the amplitude, $\omega = 14kHz$ the fundamental resonance frequency, the electronic charge $e = 1.60 \cdot 10^{-19}C$, which enters the formula in order to obtain power dissipation in eV per cycle. $\epsilon_0 = 8.85 \cdot 10^{-12}F/m$ the vacuum permittivity and $R = 12nm$ the tip radius. A constant offset of d_{offset} was introduced, which denotes the remnant distance in the junction, since the spectroscopy was stopped before the tip touched the suface, while $z = 0$ relates the end of the sweep. In addition, a constant dissipation offset P_0 was added, to correct for the free cantilever energy loss.
The only free parameter of the fit was ϵ_r, since the plate capacitor is filled with a dielectric media. In order to cross check the assumptions, the two spectroscopy fits, on Cu and $NaCl$ have been subtracted. Due to the fact, that all parameters are constant except of the permittivity constant ϵ_r, we should result in a difference of the permittivity $\Delta\epsilon_r = \epsilon_{r,NaCl} - \epsilon_{r,Cu}$ according to the literature value of sodium chloride of $\epsilon_{r,\ NaCl} = 5.9$. The difference in the fits revealed a dielectric constant change of $\Delta\epsilon_r \approx 8 \pm 3$, which is not extremely accurate, nevertheless, it is in good agreement. The fit on copper, which is a pure metal, should have an $\epsilon_r = 1$, which did not turn out. This could originate from the fact, that the highly doped silicon tip apex does not need to have an $\epsilon_r = 1$.
Furthermore, to gain information, if the Joule dissipation mechanism is the origin of the non-contact friction, the second set of spectroscopies have been performed, see 7.3. In these experiments the AFM tip has been covered with sodium chloride, by a controlled dip in one NaCl island. The change has been confirmed by means of the contact potential difference, since, the potential difference between the tip and a sodium chloride island became zero $CPD_{Nacl-NacL} = 0V$. Further, the CPD on top

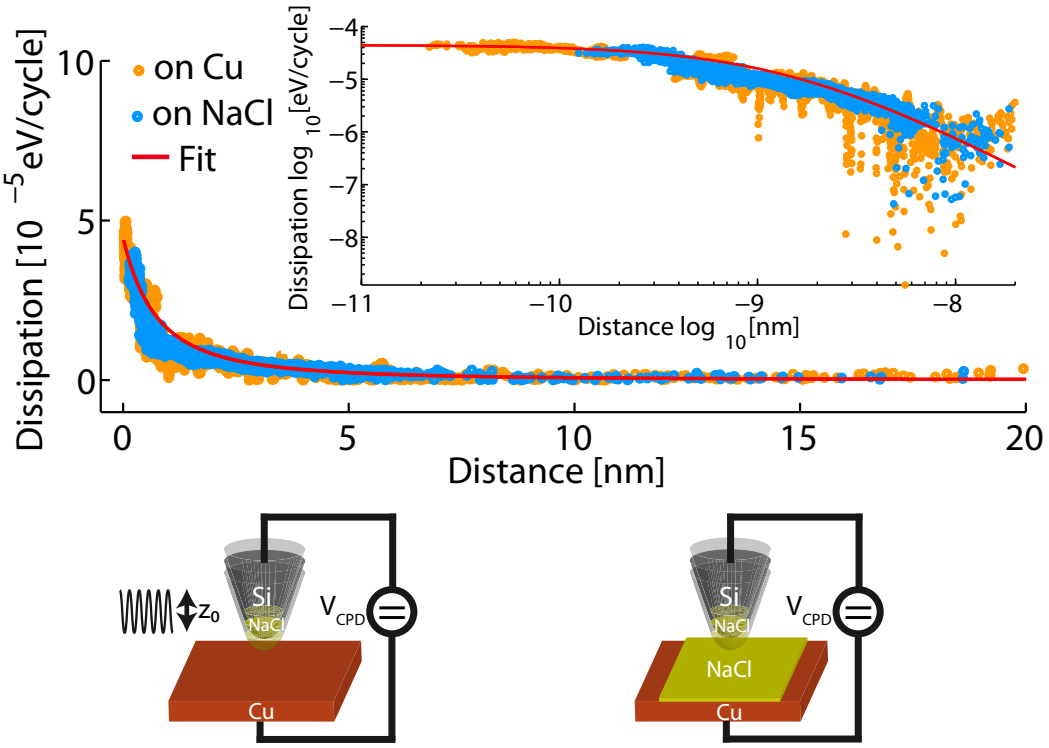

Figure 7.3. This is the second set of spectroscopy experiments. The set consists of two dissipation versus distance curves with a sodium chloride covered silicon tip on copper (orange curve) and sodium chloride (blue curve) The red line is the fit according to the Joule losses 4.34. The inset shows again the Δf vs. distance curve. Parameters: $f_{1st} \sim 14kHz$, $A_{1st} = 15nm$, $U_{ac} = 50mV$.

of copper is $\Delta CPD_{Cu-NaCl} \approx 1V$, meaning that with certainty the tip was covered with sodium chloride.
Performing then a spectroscopy on both materials lead to the data shown in 7.3, where the spectroscopy on copper shows a significant rise in the distant dependent dissipation. The energy loss per cycle was increased by a factor of 5 for the closest separation distance. Furthermore, an elevated dissipation level is measured at separation distances of $z \sim 6 - 8nm$. Also an increased energy loss for separation distances of $z = 20nm$ is measured for both spectroscopies compared to the ones in 7.2. Interestingly, the dissipation versus distance curve on sodium chloride did not change in magnitude. Furthermore, a larger scattering or noise of the data points have been measured in both spectroscopies.

The goal of this set of experiments was to determine the origin of the non-contact friction. Whether it arises from the stochastic friction force or the Joule dissipation mechanism. In case of the spectroscopy on a sodium chloride island with a sodium chloride tip, one would expect an increased stochastic friction which is about twice as large as for the uncoated silicon tip apex. Since, fluctuating force has two components, one is the fluctuating force of the surface acting on the cantilever and in addition the fluctuating force from the tip material acting on the surface, which leads

to:

$$\begin{aligned} \Gamma_{surface}(z) &= \frac{1}{k_B T}\int_0^\tau \langle F_{fluc}(z,0)F_{fluc}(z,t)\rangle dt \\ \Gamma_{tip}(z) &= \frac{1}{k_B T}\int_0^\tau \langle F_{fluc}(z,0)F_{fluc}(z,t)\rangle dt \\ \Gamma_{total\ fluc}(z) &= \Gamma_{surface}(z) + \Gamma_{tip}(z) \end{aligned} \tag{7.2}$$

Since the fluctuating forces are uncorrelated and their average does not cancel each other, it is justified to assume the total fluctuating force adds up from each component. However, this effect is not seen in the spectroscopy on sodium chloride in the magnitude to explain the non-contact friction. Nevertheless, an increased fluctuation around the mean dissipation per cycle at large separation distances is measured in both spectroscopies in 7.3 and compared to the ones of 7.2. Thus, the stochastic friction force, could explain the elevated noise in the dissipation per cycle, but not the overall behavior of the non-contact friction.
In the contrary, the line fit of the spectroscopies was done according to the Joule dissipation, see equation 7.2. Both experiments, like the one on copper and on sodium chloride, are similar systems by means of a tip sample plate capacitor with a dielectric media inside. It is regardless, on which plate the dielectric film is. Further the spectroscopy on sodium chloride islands, would be just an increased film thickness. Again the same fitting parameters were used as seen above, the only difference was the constant offset added to correct for the elevated internal dissipation of the lever. Further, the only free fitting parameter ϵ_r turned out to be equal $\Delta\epsilon_r = 0$ for both spectroscopy performed in the second set, 7.3. That is because, just the thickness of the dielectric media changes, however, in both cases we have $NaCl$ in the tip sample junction. This proves, that both systems are now equal plate capacitors with a dielectric media, causing an equally large displacement current, due to the capacitance gradient. Thus leading to a time varying current in the tip apex being uncompensated by the electric field, where a friction force arises due to motion of electrons in the tip against the local electric field. This leads to the conclusion, that the Joule dissipation mechanism is a dominant factor for the measured non-contact friction, seen in these measurements.

7.4 Bias sweep spectroscopy on copper

In order to verify the Joule dissipation mechanism, a bias spectroscopy has been performed. It is directly dependent on the applied bias voltage $\langle P_{Joule}\rangle \propto U_{Bias}^2$. Therefore, the tip was placed on top of the copper surface and the bias was swept, as it was described in section 5.3.2. The acquired dissipation data is shown in figure 7.4. Where the left side, (a), is the actual measurement of the excitation voltage converted to dissipation in $\mu eV/cycle$ depending on the distance z and the applied bias U_{Bias}. The overlaid contour lines are the corresponding constant frequency shift lines to relate the measured dissipation to the interaction strength.
The color scale shows the dissipation magnitude, where blue is low energy loss and red the maximum possible output of the applied excitation voltage $A_{exc} = A_{Exc}^{Max}$, it

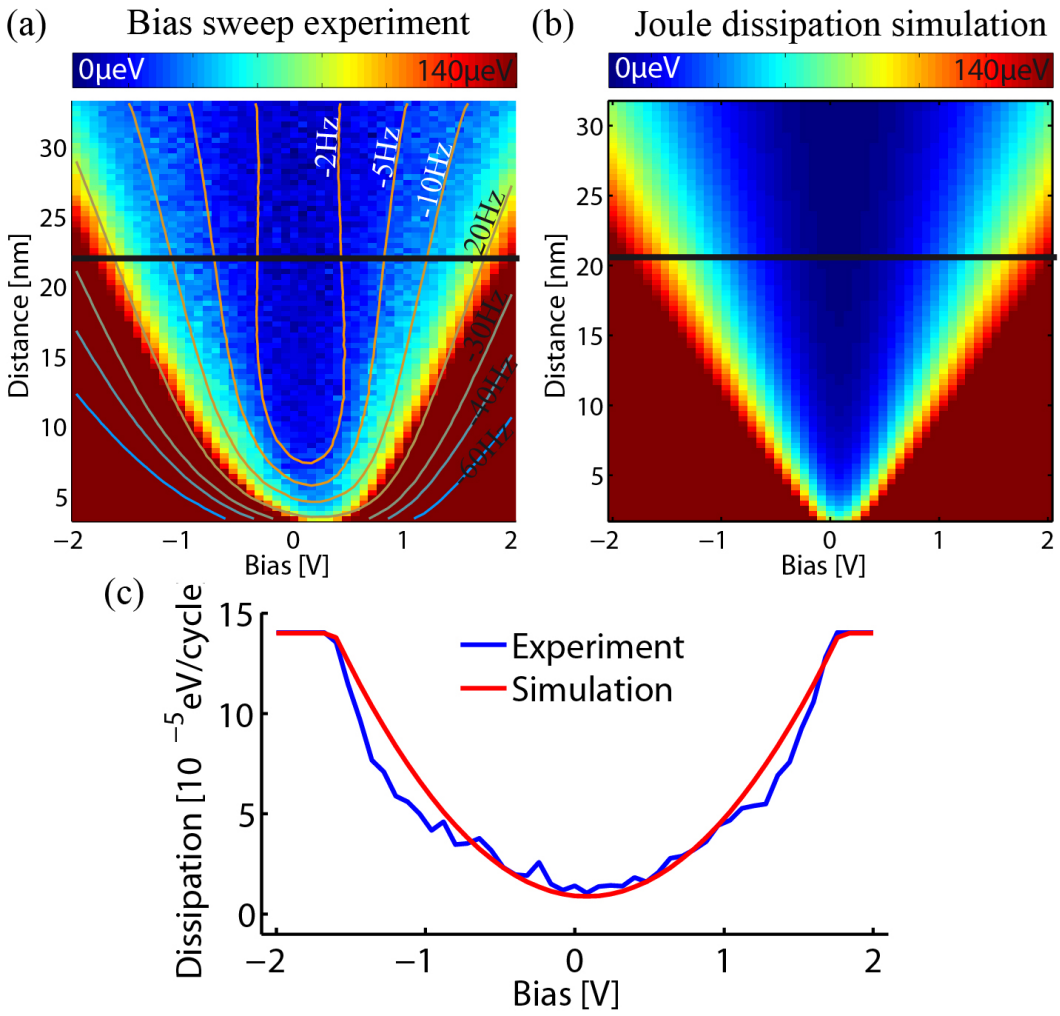

Figure 7.4. The left side (a) shows a typical bias spectroscopy with a silicon cantilever. Where on the x-axis is the sweeping bias, y-axis the tip sample distance and the color scale shows the dissipation in $\mu eV/cycle$. The other side (b) shows a simulation of the equation 7.2. Since, the Joule dissipation is voltage U dependent, it increases quadratically with the applied bias U_{bias}, see the comparison (c). Parameters of the experiment: $f_{1st} \sim 14kHz$, $A_{1st} = 15nm$

is referred to the saturation of the excitation voltage. The shape of the saturated state in figure 7.4(a), has a cone like shape, with a linear dependence on the applied biases, far away of the contact potential. The constant frequency shift contour indicates, that the saturation occurs at the same interaction force, in this case (7.4(a)) at $\Delta f = -20Hz$. The deviation of the saturation from the cone like shape, can be referred to the break down of the plate capacitor model. In other words, if the separation distance z is smaller than the tip radius R, $z < R$, the tip sample capacitor does not depend anymore linear on z. However, in the simulation of the bias dependent Joule dissipation, see 7.4(b), the overall shape of the dissipation map is recovered. A constant bias term U_{uncomp} had to be added to achieve the curvature of the dissipation at close distances. This term relates to the physical property of

the tip, where the tip is not a homogeneous object with a single work function. Therefore, a perfect compensation of the electric field cannot be achieved at very close distances, due to patch forces. The simulated dissipation map was generated by:

$$\langle P_{Joule} \rangle = \pi \; R_{tip} \; \left(\pi \epsilon_0 \epsilon_r \frac{R}{z + d_{offset}} \right)^2 \; \left[(U_{Bias} - U_{CPD})^2 + U_{uncomp} \right] \; A^2 \; \omega^2 \; \frac{1}{e} \tag{7.3}$$

The equation 7.3 reproduces the result in a qualitative way. The parameters of the simulation are: $R_{Tip,Si} \approx 10^4 \Omega/cm$, $U_{CPD} = 0V$, $U_{uncomp} = 0.16V$, $A = 15nm$, $\omega = 14kHz$, $e = 1.60 \cdot 10^{-19}C$, $\epsilon_0 = 8.85 \cdot 10^{-12}F/m$, $\epsilon_{r\ Si} = 12.1$, $R = 15.2nm$, $d_{offset} = 5.62nm$.
To gain visual guidance in order to confirm the cone like shape of the saturated state, we cut off dissipation values above the maximum of the measurements and set them to $\langle P_{sim,max} \rangle = 140 \mu eV$. Thus, the qualitative agreement of the simulation compared to the experiment was achieved. Therefore, leading to the conclusion, that the dominant dissipation mechanism for the bias spectroscopy of a silicon cantilever on a copper surface is the Joule dissipation mechanism.

7.5 Conclusions

For the investigated copper - sodium chloride surface, we find a dominance of the Joule dissipation mechanism to the measured non-contact friction. The model of the tip sample capacitor system is a suitable approach to explain the measured dissipation of the pendulum AFM, as seen in [74]. It is shown, that the electronic properties, like conductance, produce a significant difference in the non-contact friction. However, due to the model of the tip sample capacitor, it is indifferent, if the insulator is at the surface or covering the tip, see figures 7.2, 7.3. Therefor it is only dependent on the existence of an additional dielectric media in the tip sample junction.
Further, the bias dependence of the Joule dissipation was measured and confirmed 7.4, where the experiment and the simulation show that already small inhomogeneities of the work functions at the tip apex create significant rise in the dissipation. In addition, the bias spectroscopy indicates that the measured dissipation corresponds to the interaction force. In analogy with the contact friction experiments, where the measured friction force is proportional to the applied load. In the non-contact case, the measured dissipation (non-contact friction) is proportional to the interaction force with an underlying material. Leading to the fact, that Amonton's first friction law can be extended to the non-contact friction experiments, at least for these copper - sodium chloride measurements.
The investigated copper - sodium chloride surface demonstrated already the importance of the dielectric properties, to the measured dissipation. The study of electronic phase transitions of a metal - superconductor revealed a strong suppression of the non-contact friction, in the superconducting state [3]. Hence, the electronic properties have a key feature for the non-contact friction and the electric phase transitions deliver a striking possibility to confirm this observations. Therefore, we want to discuss in the following chapter a rather unique electronic state and its contribution

to the non-contact friction, the Charge-Density-Wave state of Niobium-Diselenide sample.

8 $NbSe_2$ a Charge Density Wave material

The work of this chapter has been published in:

Nature Materials 13, 173 - 177 (2014) doi:10.1038/nmat3836

Layered dichalchogenides have long been known for their phase transitions leading to picometre-sized superstructure lattice distortions and corresponding new electronic periodicities in their low-temperature ground state [75]. Among them, $NbSe_2$ (with 2H stacking) [43] stands out as a material exhibiting bulk **C**harge **D**ensity **W**ave (CDW) below the long-range-order onset temperature $T_{CDW} = 33K$ [76], as well as superconductivity below $T = 7.2K$. Here, a dissipation study is performed on the CDW-state of $NbSe_2$, in order to investigate the effects of the electron order on the non-contact friction.

8.1 Crystal structure and the CDW

Layered dichalchogenides are known for their crystallographic phase transitions, resulting in a periodic distortion of the crystal lattice. Niobium-Diselenide exhibits such a phase transition at $T_{CDW} = 33K$, where the niobium atoms rearrange periodically. Marezio *et al.* [77] Investigated the bulk structure. The unit cell of a double layer is drawn in the figure 8.1, adapted from [77]. The displacement of the niobium atoms is exaggerated to give a visual guidance. The crystal structure is shown from the top view, where the niobium atoms are marked in *green* and the selenium atoms in *orange*. The indices's of each atom are according to the layer number counted from top to bottom with $1 - 6$. A three dimensional representation is drawn in the lower left corner of the figure 8.1. The internal binding of $Se - Nb - Se$ atoms are covalent bonded, while the layers are bound by $\pi - \pi$-stacking and therefore are weak as in graphite. The cleaving plane is in every second layer, resulting in a step height of $h_{step} = 1.25nm$. The periodic distortion of the crystal lattice is only present in the niobium layer Nb, resulting in a quasi-$2D$ reconstruction of the crystal lattice and the modification of the electron density.

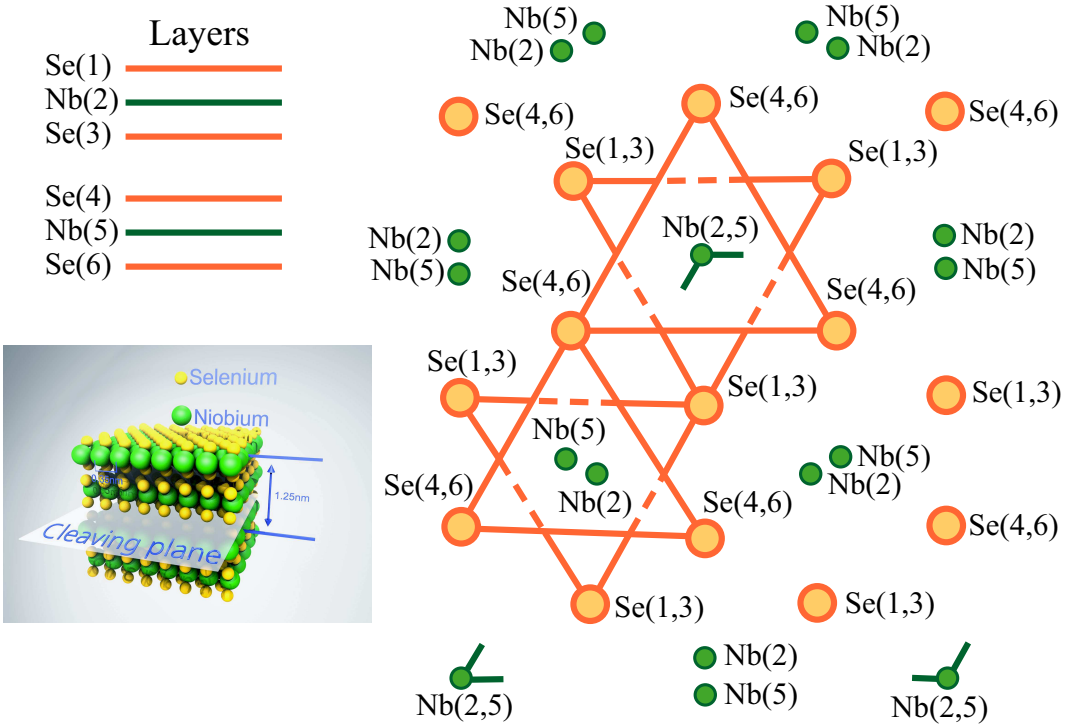

Figure 8.1. Here, a double layer of the periodically distorted crystal structure $NbSe_2$ is shown. The niobium atoms are represented as green circles and the selenium as orange, where the indices's are regarding the layer number (see upper left). The niobium displacement is exaggerated to give visual guidance. A three dimensional representation is seen in the inset on the lower left. Figure is adapted from reference [77]

8.1.1 CDW transition

The formation of a charge density wave state, was first predicted for a one dimensional chain of metal atoms by Peierls in 1955 [78]. He proposed that a one dimensional atomic chain becomes unstable at low temperatures in case, if the electron density is coupled via the electron-phonon coupling to the underlying lattice [79].
Let us consider the case of a metal at zero temperature $T = 0K$ with a half filled band. In the ground state the electrons are filled up to the Fermi level E_F. The lattice is an array of atoms with the lattice constant a and the electron density $\rho(r)$ is homogeneous in the real space, see figure 8.2(a), and no electron order exists.
However, in presence of an electron-electron or electron-phonon coupling, the lattice becomes instable at low temperatures and a periodic distortion evolves, which stabilizes the crystal lattice. The period of the lattice distortion λ is related to the Fermi wave vector k_F, by $\lambda = \pi/k_F$. Due to the distortion, a gap opens at the Fermi level in the single particle excitation spectrum, see figure 8.2(b). Since the band is only filled up to k_F, an opening of a gap results in a reduction of the electronic energy. In a pure one dimensional case the gap opening is proportional to the lattice distortion u, where the energy gain due to the distortion is $u^2 \ln u$. The lattice distortion builds up an elastic energy in the crystal proportional to u^2, which limits the maximum energy reduction by the gap opening and stabilizes the lattice distortion [78]. The change in the energy dispersion relation leads to a position dependent electron den-

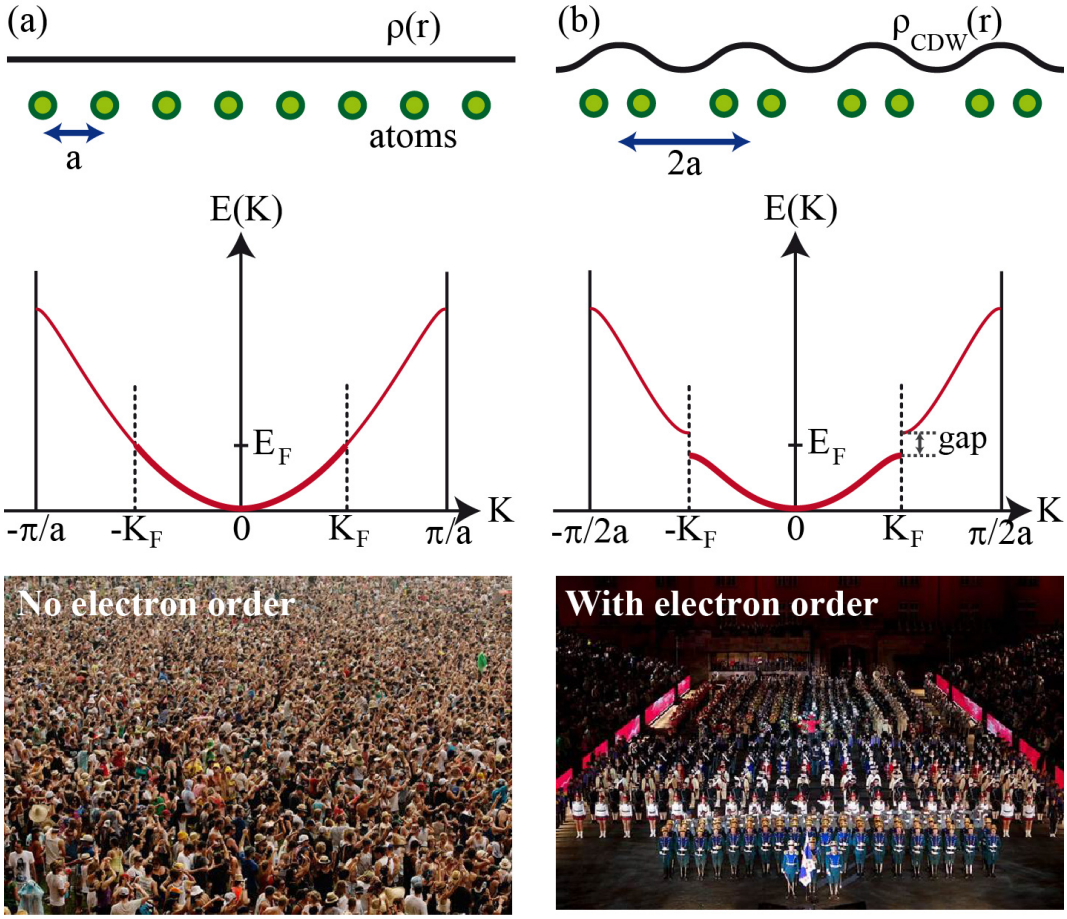

Figure 8.2. The Peierls transition is sketched for the one dimensional case. In the absence of an electron-phonon coupling the lattice remains in the undistorted state, with lattice constant a and no long range order, see (a). In the presence of electron-phonon coupling the crystal undergoes a periodic lattice distortion with the periodicity of $2a$ and a gap opens in the single particle excitation spectra. Leading to a coherent order parameter of the electron density $\rho_{CDW}(r)$, see (b). Pictures adapted [78] and from Basel Tattoo

sity $\rho(r)$, which is a periodic function of the position r, with the period b. This is the origin of the charge density wave. Further, for an arbitrary band filling of the period of the charge density wave vector will be incommensurate with the underlying lattice distortion, which means λ/b is irrational.
The position dependent electron density is:

$$\begin{aligned} \rho(x) &= \rho_0 + \frac{\Delta\ \rho_0}{\Lambda v_F k_f} \cos(2k_F\ x + \phi) \\ &= \rho_0 + \rho_1 \cos(2k_F\ x + \phi) \end{aligned} \tag{8.1}$$

where $\rho_0 = \pi/k_F$ is the electron density of the undistorted system, Δ the temperature dependent width of the gap, Λ the electron-phonon coupling constant, v_F the Fermi velocity, k_F the Fermi wave vector, ϕ the phase order parameter, ρ_1 the combined

amplitude order parameter. The collective mode is formed by electron hole pairs, introducing the wave vector $2k_F$ for the periodicity of the CDW.
In the upper mentioned case, the underlying theory assumes a Fermi surface nesting of the CDW, which stabilizes the transition for layered dichalchogenides, like TaS_2 (with 1T stacking). In case of the niobium-diselenide the Fermi surface nesting is not the driving force, to stabilize the system. For $NbSe_2$ the charge density modulation arises really only from the electron-phonon coupling and the periodic lattice distortion. Nevertheless, the commonly used term CDW will be used further on.

8.1.2 Pinned CDW

In 1954 Fröhlich [80] predicted that the CDW state, described by a phase and amplitude order parameter, should slide under an externally applied electric field, giving rise to the CDW super current, similar as in the case of superconductor. Experiments and theory later on revealed the contrary. The collective charge density wave state does not lead to a super current, since the electron state is not independent of the underlying lattice. This is in contrast to the superconductors.
For collective CDW state impurities, grain boundaries, surface effects or electrostatic potential lead to a translational symmetry breaking in the phase excitation and consequently causes pinning. In case of a random impurity distribution the long range order is perturbed and leads to a non conducting and highly polarizable ground state of the CDW.
The current-voltage transport measurements show the non linear dependence of the CDW on an applied electrostatic potential, where a threshold voltage needed to be overcome to unleash a current [81, 82]. In the figure 8.3(a) is a sketch of the I-V characteristic, while 8.3(b) sketches the onset of the measured current of the CDW, which was adapted from reference [81, 83].

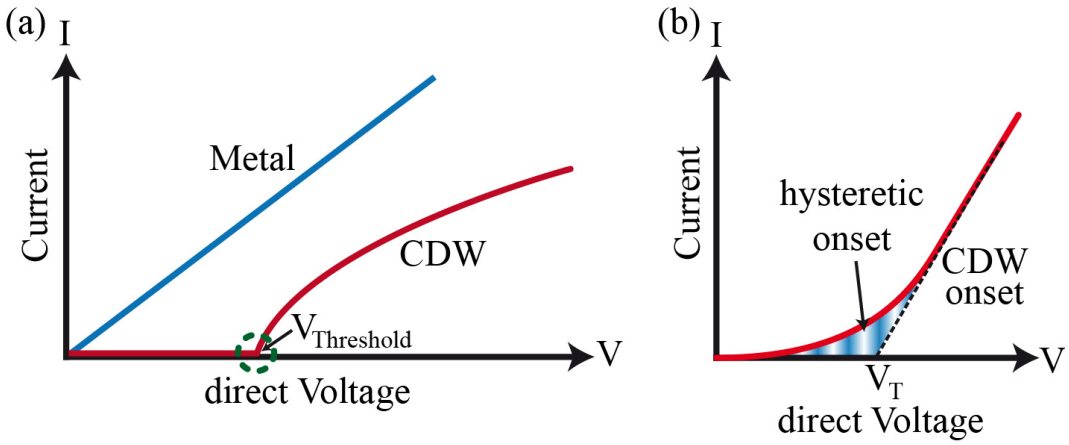

Figure 8.3. A sketch of the I-V characteristic is shown, where (a) shows the differences between the linear dependence of a metal and the non-linear for the CDW state. The threshold voltage is indicated by the dotted circle. In (b) the onset of the depinning is shown, where the smooth rise of the current implies the elastic behavior of the collective state. Figures adapted from reference [81, 83]

The figure 8.3(a), plots two different characteristic behaviors. Above the CDW transition (*blue*), $NbSe_2$ has a metallic characteristic with a linear dependence of the current on the voltage. Below the CDW transition (*red*) a direct voltage threshold needs to be overcome, in order to measure a current. That is due to the impurity pinning. Further, the onset of the depinning threshold of the CDW was investigated in more details [84], where a non linear rise of the current is measured, see figure 8.3(b). The conclusion of these experiments is, that the CDW state behaves as a coherent elastic media.
In first approximation the CDW can be assumed to be a rigid object, which explains the depinning threshold. Thus, we start with the equation of motion for a single object with an effective mass M^* and in an externally applied potential U, so we are able to write:

$$\frac{1}{\tau}\frac{dx}{dt} + \frac{\omega_p^2}{k_F}\sin(k_F x) = \frac{U}{M^*} \tag{8.2}$$

where, k_F is the Fermi wave vector, ω_p the characteristic pinning frequency, τ the period of one CDW oscillation. Solving the equation of motion determines the drift velocity of the collective mode and the pinning potential U_T:

$$\begin{aligned} v_d &= \frac{\tau}{M^*}\sqrt{U^2 + U_T^2} \\ U_T &= \frac{1}{2}\frac{M^*\omega_p^2}{k_F} \end{aligned} \tag{8.3}$$

The drift velocity and the pinning potential explains the depinning threshold. However, it could not explain the hysteretic behavior in the vicinity of the threshold. Close to it the CDW phase switches between slow creep and phase slip. Thus, more rigorous approach was formulated by Fukuyama, Lee, and Rice [79, 85, 86], treating the CDW as an elastic condensate pinned to a weak pinning potential of random impurities $V(r) = V_0\delta(r)$, with an externally applied perturbation. In the case, when the amplitude fluctuation can be neglected and the impurities perturb only the phase order parameter, the derived Hamiltonian is:

$$\mathcal{H} = \frac{1}{2}\int d\mathbf{r}\ \kappa\ (\nabla\phi(\mathbf{r}))^2 + V_0\ \rho_1 \sum_i \cos\left[2\mathbf{k}_F\cdot\mathbf{r}_i + \phi(\mathbf{r}_i)\right] + \int d\mathbf{r}\ \frac{\rho(\mathbf{r})}{k_F^2}\mathbf{V}\cdot\mathbf{k}_F \tag{8.4}$$

where the first term describes the phase elasticity of the CDW with the elasticity coupling constant κ depending on the phase fluctuations. The second term is represents the CDW phase pinning by random impurities [87, 88]. The third and last term takes the externally applied potential into account.
Latter on, we show that by introducing the localized perturbation potential by the AFM, we drive a CDW phase slip event in each tip oscillation cycle. Thus, we observe dissipation due to hysteretic switching of the CDW.

8.2 Preparation

Niobium-Diselenide ($NbSe_2$) single crystals with a high purity and large dimensions are rather complicated to manufacture by means of a standard chemical-vapour-transport technique with iodine as the transport agent. The investigated crystal was produced by Prof. Dr. Geetha Balakrishnan (Department of Physics, University of Warwick). The residual contaminants of the transport have been washed away with solvents before the crystal was mounted on an Omicron UHV holder. The $NbSe_2$ crystal has been cleaved under UHV conditions and annealed at $T = 380K$ for $t = 30min$ in order to remove remnant static charges from the cleaving process. The prepared crystal has been cooled down to $T = 77K$ for the further measurements.

8.3 Niobium-Diselenide at T=77K

To get insights into the non-contact friction on $NbSe_2$ and the CDW transition at $T_{CDW} = 34K$, we performed measurements at liquid nitrogen temperatures $T = 77K$, well above the transition.
Firstly, we obtained a topographical image and a contact potential map of the freshly cleaved single crystal, see 8.4(a,b). There it is already noticeable, that the surface is atomically flat over a large spatial area, here $300nm \times 300nm$. In fact, stepped structures are rare to find on a well cleaved $NbSe_2$ crystal. On the other hand, the contact potential map is homogeneous over the whole measured range. The variance of the CP values around the mean CPD, $CPD_{mean} \sim 600mV$, arises due to the detection limit for the small amplitude $A_{2nd} = 0.6nm$, see 6.11(c).
Secondly, we performed a force distance spectroscopy at the marked place 8.4(a), to investigate the non-contact friction behavior in the absence of the CDW. As it is expected, the distant dependent energy loss is smooth and becomes significant only at small separation distances. The dissipation signal has been fitted according to the Joule energy loss mechanism, the fit parameters can be found in the figure caption, see 8.4. The results imply, in the absence of a CDW, $NbSe_2$ exerts non-contact friction comparable to a normal metal.

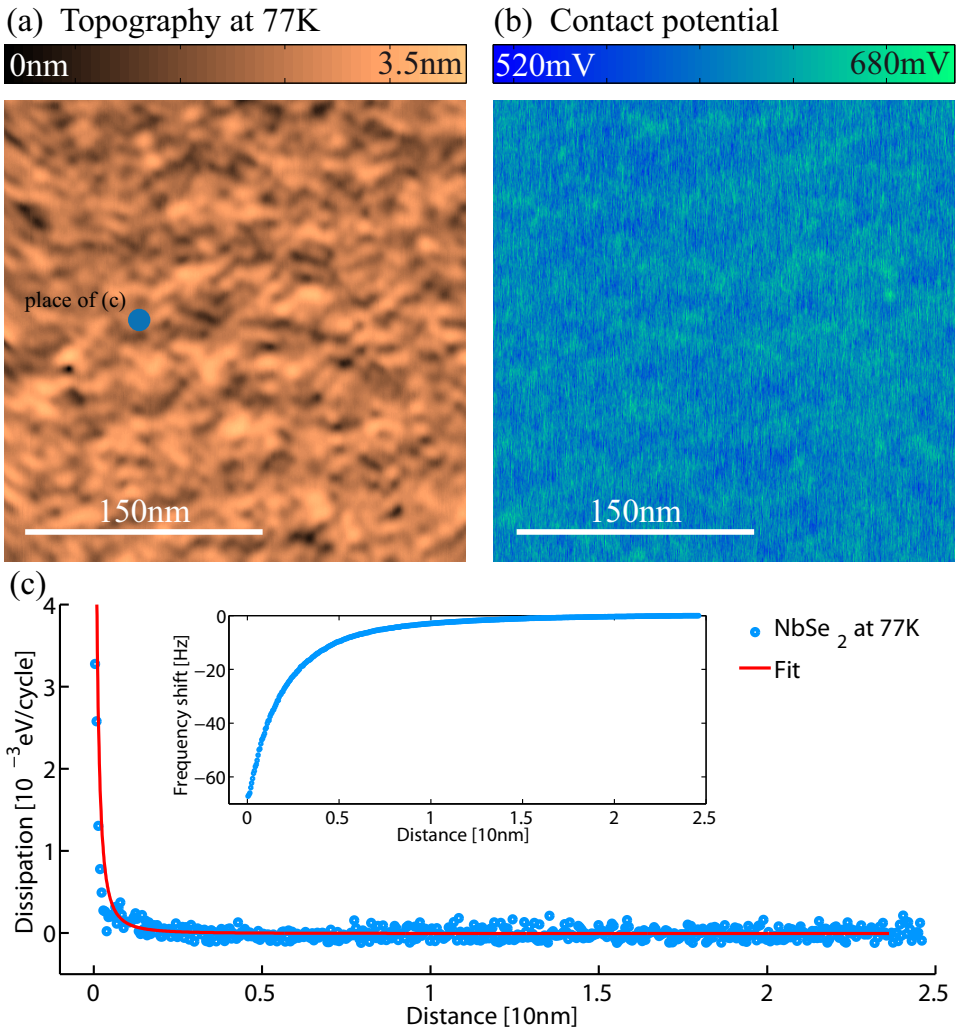

Figure 8.4. The measurements of $NbSe_2$ at $T = 77K$ are shown, with (a) the topography and (b) the simultaneously acquired contact potential map. The surface is widely flat and without any observable defects. The contact potential map shows the homogeneity of the surface material. (c) showes a force distance spectroscopy on the place indicated in the image (a). It has been fitted with the formula of the Joule dissipation, which is the expected energy loss mechanism. Image parameters: $f_{2nd} \sim 90kHz$, $A_{2nd} = 0.6nm$, $\Delta f = -6Hz$, $U_{ac} = 80mV$. Spectroscopy parameters: $f_{1st} \sim 14.5kHz$, $A_{1st} = 5nm$, $U_{ac} = 80mV$. Fit parameters: $R_{Si} = 4 \cdot 10^4 \Omega/cm^2$, $U_{ac} = 80mV$, $\epsilon_{r,Si} = 12.1$, $R_{tip} = 12.5nm$, $A_{1st} = 5nm$, $d_{offset} = 0.8nm$.

8.4 $NbSe_2$ at T=5K

For temperatures well below the Charge Density Wave transition, the measured non-contact friction changes drastically. At $T = 5K$, niobium-diselenide has a CDW, with its transition temperature of $T_{CDW} = 34K$, and below $T_c = 7.2K$ the CDW coexists with the superconductivity [76].
A series of images were taken in order to find an area on $NbSe_2$ with a stepped structure. Figure 8.5 (a), shows holes after cleaving the $NbSe_2$ sample. On a scan

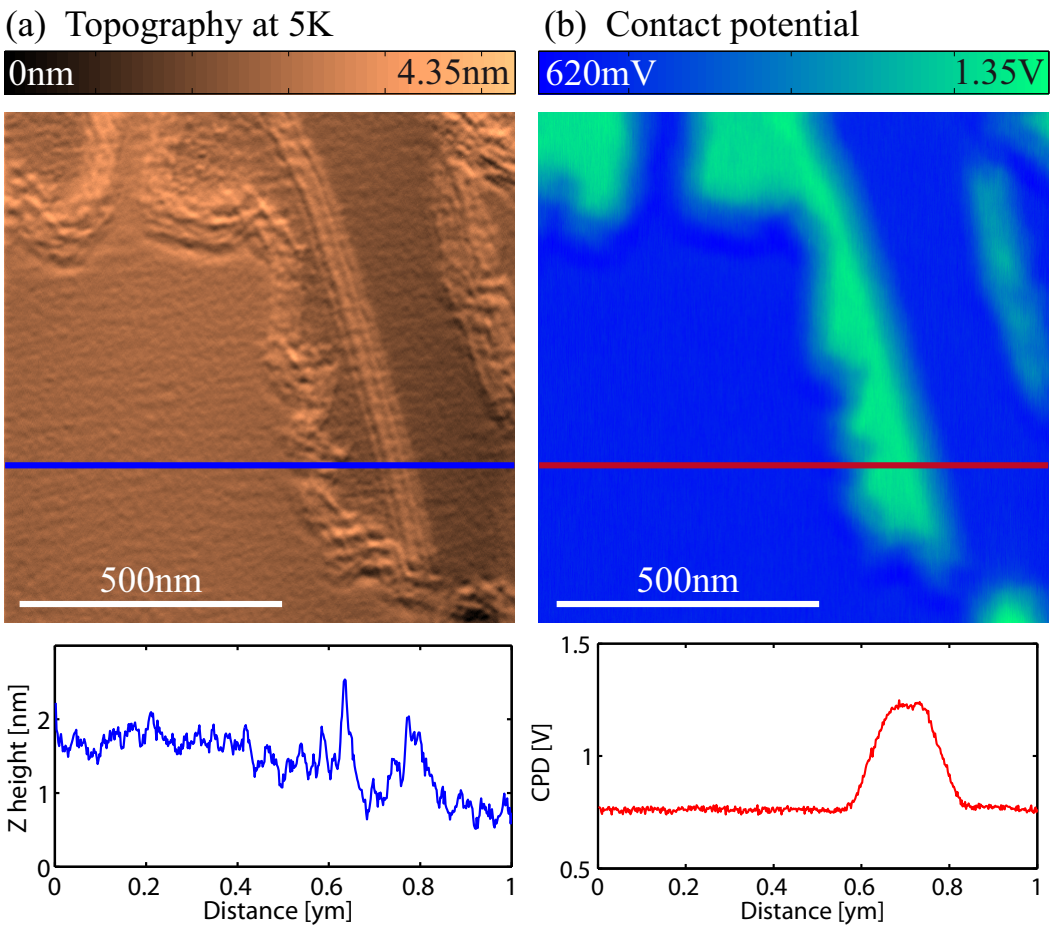

Figure 8.5. Topography and the contact potential are shown, with line scans below each. Image parameters: $f_{2nd} \sim 90kHz$, $A_{2nd} = 0.6nm$, $\Delta f = -10Hz$, $U_{ac} = 80mV$.

range of $1\mu m \times 1\mu m$. The line scan below the image roughly indicates the overall flatness of the surface. Due to the choice of a small amplitude $A_{2nd} = 0.6nm$, it is not possible to determine the step height, since the lateral forces dominate the normal one.
However, the contact potential map, 8.5 (b), clearly shows a change of contact potential of $CPD_{hole} - CPD_{plane} = \Delta CPD = 1.35V - 0.61V \Rightarrow 740mV$. This large change of CPD is contrary to the general theory of the work function of a single material, since, we are a most certain, that no surface contaminants are present. In addition, no such feature has been observed at $T = 77K$. We could not be certain, that the CDW state is present in this sample, due to the fact, that the pendulum AFM has no capability to image with atomic resolution as well as resolving the electronic density, an additional approach had to be chosen. Thus, measurements on a tuning fork AFT/STM had to be done.

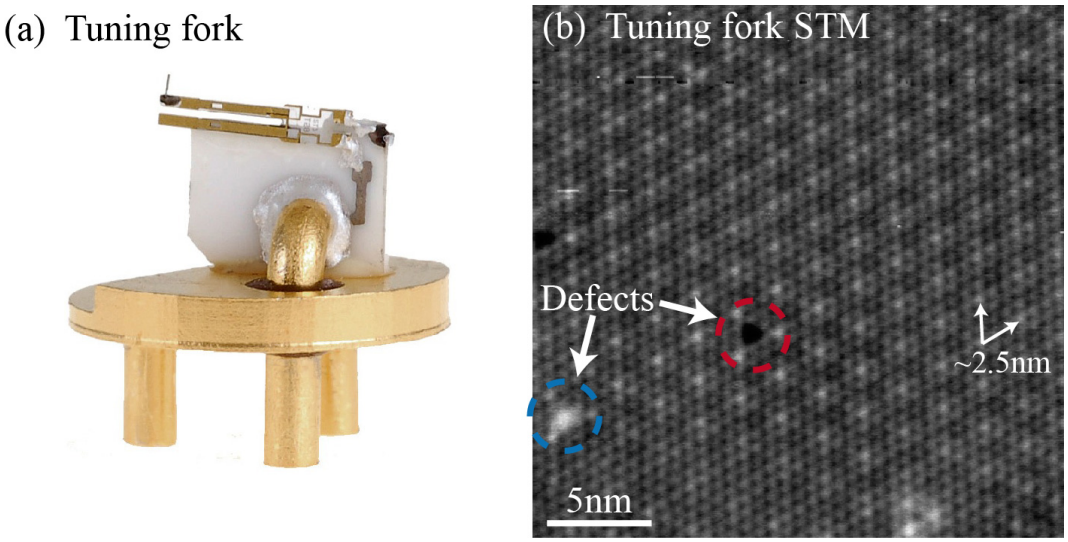

Figure 8.6. The Omicron tuning fork (a) measurement at $T = 5K$ in the **S**canning **T**unneling **M**icroscopy (STM) mode nicely shows the atomically resolved $NbSe_2$ surface with its charge density wave Moiré pattern, (b). Here, two defects are emphasized with colored circles. Image parameters: $I = 10pA$, $U = 5mV$.

8.5 Tuning fork measurements at T=5K

An Omicron tuning fork AFM/STM, 8.6(a), operating at low temperatures has the desired capability to resolve $NbSe_2$ on an atomic scale as well as the CDW induced Moiré pattern, by means of STM, see figure 8.6(b). The shown incommensurate modulation of the CDW on $NbSe_2$, with its nearby (3×3) commensurate periodicity, is well known [89]. One remarkable fact is, that the charge density wave is pinned in the near proximity of defects, Selenium vacancies, and adsorbates (marked in colored circles on (b)). In the vicinity of defects, the CDW can locally survive pristine, well above transition temperature T_{CDW}. In addition, the pinning of the CDW by these defects and the regular array of protrusions in the electron density confirms, *that the CDW is forced to rearrange between two boundary conditions.*
Hence, it is proven, that the underlying $NbSe_2$ sample exhibits a charge density wave transition for low temperatures, we were confident to relate further measurements to the presence of the CDW.

8.6 Spectroscopy with pendulum AFM

Dissipation versus distance spectroscopies on $NbSe_2$ well below the CDW transition, are strikingly different to any other previously observed smooth dissipation mechanism on metals, insulators, or superconductors, see figure 8.7. There are discrete dissipation maxima detectable at tip sample distances of $\Delta z = 3.2nm,\ 2.5nm,\ 1.7nm$. It is remarkable that the energy loss is localized and *drops off* after each maximum. Meaning that the dissipation processes are not linked and not adding up to the total non-contact friction. Thus, the spikes must be caused by a hysteretical process not interchangeable with each other.

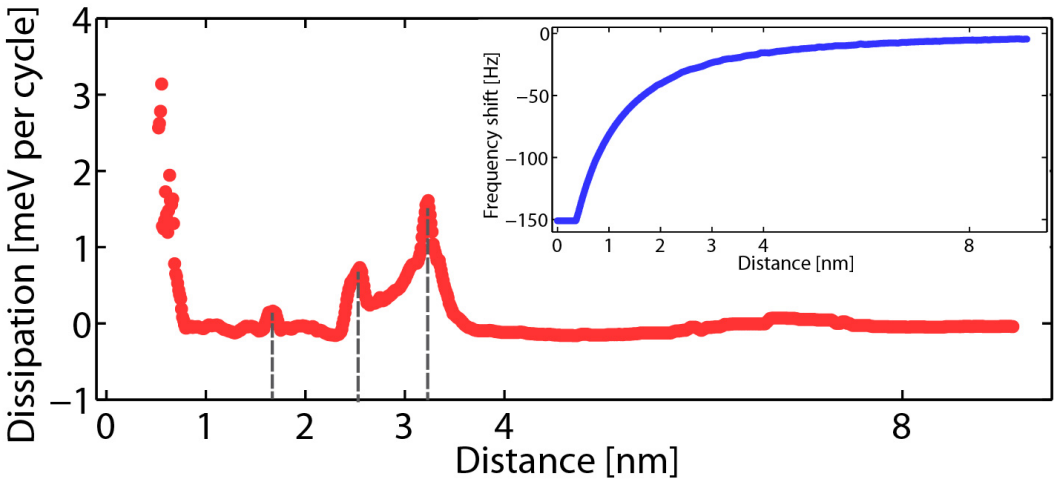

Figure 8.7. A spectroscopy on $NbSe_2$ is shown. The according frequency shift is found in the inset. Spectroscopy parameters: $f_{1st} = 14kHz$, $A_{1st} = 2nm$, $k \approx 0.2N/m$, $Q = 900000$.

To gather a more knowledge, we performed additional spectroscopies on different places on the surface. The main factor of interest was, whether the peaks and their composition, as well as their magnitude is a global phenomenon or a particular feature of the local microscopic position on the surface. Therefore, we performed a series of spectroscopies in a line, crossing on purpose a step edge between the lower terrace, with the increased contact potential difference of $U_{CPD} = 1.3V$, and the upper, with $U_{CPD} \sim 0.6V$, as illustrated in figure 8.5.
The results of the spectroscopies are found in figure 8.8, with their dissipation versus distance curves. The exact places of each experiment are shown in the topography marked with the letters.
The first thing to notice is the remarkable similarity of the spectroscopies A, B, $I - N$, with only a small difference in their relative magnitude. However, the distance dependence of the spikes are extremely well reproduced for each spectroscopy, and follows the gray bars in figure 8.8(b). Even though, that the spectroscopy on the hole exhibits a different contact potential, we measured the same composition and the same count of dissipation maxima.
For places chosen on the step, where the most irregularities are expected, we found a different composition of maxima for each spectroscopy, with a varying intensity compared to the other mentioned spectroscopies. Nevertheless, it is most striking to exhibit such discreet multiple dissipation events with this magnitude at the large separation distances. Further, we can imply from the measurements, *that flat places exhibit the same behavior of non-contact friction, regardless of the measured CPD and the distance between each other.* Extreme variation of non-contact friction has been found in the vicinity of step edges and other irregular places. Nevertheless, regardless of the composition or the place, the most astonishing finding is a whole train of non-contact friction maxima, extending far out above the surface with discreet spikes. Similar AFM dissipation peaks have been found in AFM for $InAs$ quantum dots, when the electrostatic field drives the charging/discharging of the dot, if the

coulomb barrier is overcome. The crucial difference is, that the QD observations are purely voltage driven, [47, 90]
In order to complete the picture and give an information about the dependence on the applied bias voltage, we performed a bias spectroscopy. From this we learn, whether the dissipation maxima are voltage driven or due to a process driven by interaction force.

8.7 Bias dependent dissipation

For the bias spectroscopy a flat place of the upper terrace was chosen, with a CPD of $U_{CPD} \sim 0.6V$. The question arises, whether evolution of the dissipation maxima is driven by the electric field in the tip sample junction or by the interaction force of

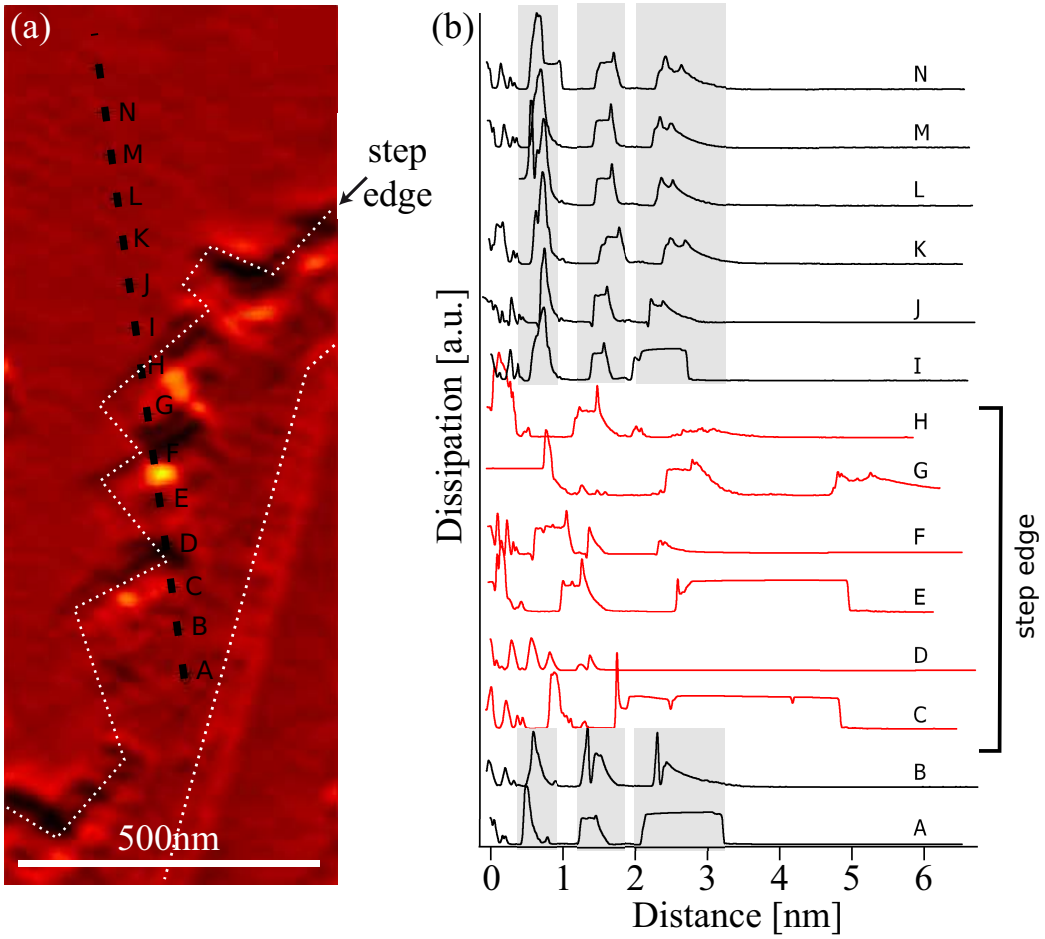

Figure 8.8. A series of spectroscopies on $NbSe_2$ is shown. The purpose was to determine the local and global behavior of the non-contact friction maxima. (a) shows the position of each spectroscopy marked by the letters. (b) shows the acquired dissipation versus distance curves. For the flat surface, we obtained similar compositions and magnitudes of the dissipation maxima, while the spectroscopies acquired on the step edge are not comparable. However they still show non-contact friction maxima. Spectroscopy parameters: $f_{1st} = 14kHz$, $A_{1st} = 2nm$, $k \approx 0.2N/m$, $Q = 900000$.

the tip. Therefore, we show here the result of the bias spectroscopy, figure 8.9.

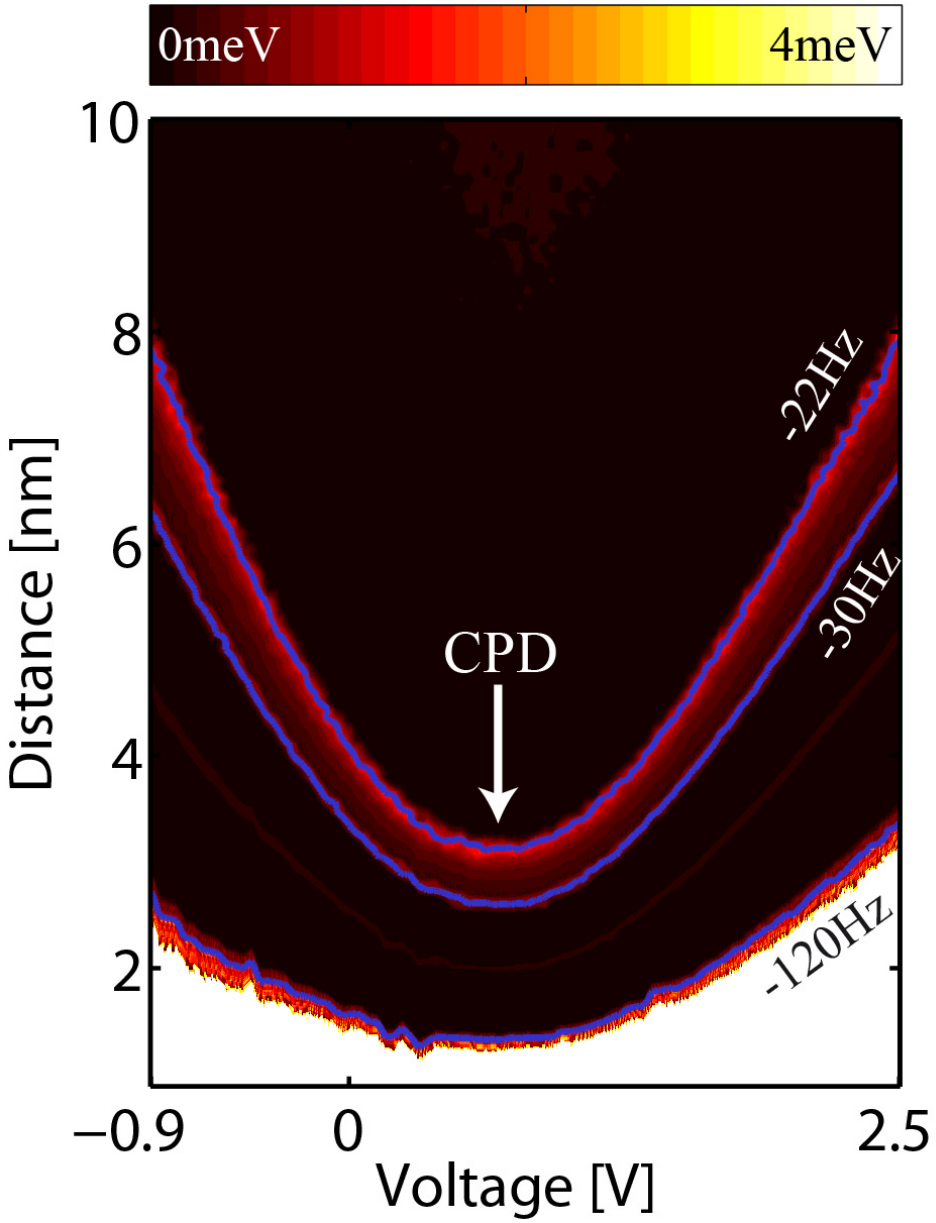

Figure 8.9. The bias spectroscopy on $NbSe_2$ is shown (a), with a line section at zero bias to give a better insight into the dissipation and frequency shift (b,c). Spectroscopy parameters: $f_{1st} = 12kHz$, $A_{1st} = 5nm$, $k \approx 0.2N/m$, $Q \approx 900000$.

Here, the dissipation per oscillation cycle is color coded and plotted against the distance and applied bias voltage. Firstly, we notice, that the dissipation maxima extending further in distance from the sample for larger offsets of the bias. Secondly, the evolution of each maximum is smooth with respect to the bias voltage. Thirdly, the magnitude of the dissipation of each maximum is exactly the same, regardless of the voltage.
There are three reasons, why the dissipation mechanism is force driven. On the one

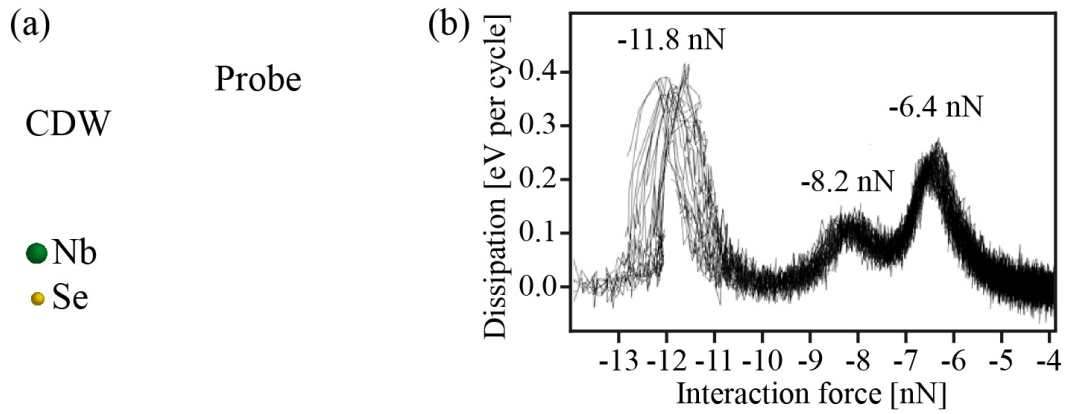

Figure 8.10. The collapsed bias spectroscopy of the tuning fork AFM is shown in (b). With a sketch of the probe interacting with the CDW floating on top of the $NbSe_2$ surface. Spectroscopy parameters: $f = 25kHz$, $A = 200pm$, $k \approx 1800N/m$, $Q \approx 35000$.

hand, at the contact potential and the absence of an electric field in the tip sample junction, we still observe the non-contact friction spikes. This means, that both the vdW force and the electrostatic force are capable to drive the mechanism.
Secondly, the dissipation maxima follow the contours of constant interaction, indicated by the superimposed contours of $\Delta f = -22Hz$, $-30Hz$, $-120Hz$ in figure 8.9. Third and last indicator, is that the interaction contour as well as the dissipation maxima, follows the quadratic behavior. That is expected for the capacitively coupled conical tip and sample, where $F \sim U^2/d$. From this result, it is reasonable to state, that the driving mechanism of the non-contact friction is force driven.
Due to the fact, that there is no confirmed conversion algorithm for the frequency shift to the interaction force for the pendulum geometry, as the Sader-Jarvis conversion algorithm [91],we had to perform the spectroscopies with the tuning fork AFM. There, we are able to recover the interaction force from the measured frequency shift. The open question is, whether the tuning fork is sensitive enough to detect the dissipation spikes.
An amazing fact is, that the dissipation maxima are measured by the tuning fork AFM, as well, with three distinct maxima. In order to confirm, that the dissipation mechanism is measured at a constant interaction force. A bias spectroscopy has been performed. The spectra for different bias voltages are converted by means of the Sader-Jarvis algorithm and plotted in figure 8.10(b). Each maxima could be clearly related to a particular interaction force, where the three measured maxima appeared at interaction forces of $F_{int} = -6.4nN$, $-8.2nN$, $-11.8nN$. *This leaves no doubt of the force driven nature of the dissipation mechanism.*
One mechanism of dissipation could be the direct interaction with the crystal itself. Meaning, that the layers of the crystal lift off and produce an adhesion hysteresis as mentioned in the theory chapter. Therefore, a last set of experiment had to be done, to rule that out.
Niobium-disulfide, NbS_2, is another representative of the layered dichalchogenides. It has the similar crystal structure and is another layered compound, but does not exhibit a CDW transition. The layers of NbS_2 are also weakly bound via $\pi - \pi$ stacking and therefore comparable, by means of crystal structure.

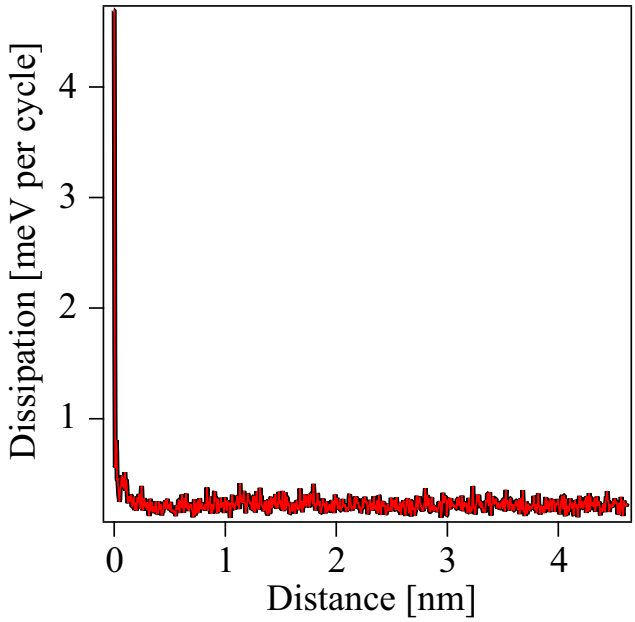

Figure 8.11. The dissipation versus distance is shown for NbS_2. No dissipation maxima is observed, due to layer lift off. Spectroscopy parameters: $f_{1st} = 12kHz$, $A_{1st} = 5nm$, $k \approx 0.2N/m$, $Q \approx 800000$, $T = 5K$.

In the figure 8.11 a spectroscopy of NbS_2 at $T = 5K$ is shown. It is representative for all spectroscopies, which we measured on the surface. The difference to $NbSe_2$ is immediately visible, there are no dissipation maxima present. Therefore, we are confident to rule out the layer lift off as a dissipation mechanism for $NbSe_2$, which leaves only the CDW state as a possible candidate for the dissipation observed in all spectroscopies on $NbSe_2$.

8.8 2π Phase slip

So, what is the origin of these non-contact friction maxima extending far above the surface? Even with guessing, the most reasonable answer can be given right away: Their presence is related to the CDW, due to the fact, that the surface shows a smooth dissipation rise well above the transition at $T = 77K$. Also NbS_2, a similar layered dichalchogenides without a CDW, does not show any peaks in the dissipation. However, the exact mechanism is rather simple. As it has been discussed, the charge density wave is, in first approximation, an elastic coherent media pinned by surface contaminants by the phase order parameter $\phi(x)$ of the density modulation $\rho(x) = \rho_1 \cos(Q \cdot x + \phi(x))$, where Q is the wavenumber and ρ_1 the constant amplitude order parameter.
The tip and its potential is acting as a localized tunable perturbation of the local phase order parameter of the CDW. Meaning, that the tip is acting as an additional defect, which is able to probe the local elasticity of the phase order parameter. This problem is then reduced to an energy minimization, which is a function of the order parameter $\phi(x)$ and the external perturbing tip potential $V(x)$:

$$E(\phi(x)) = \int \left[(\nabla\phi(x))^2 + V(x)\rho(x) \right] dx \tag{8.5}$$

For reasons of simplicity the CDW is treated in uni-direction, while the mechanism should hold for a tri-directional $NbSe_2$, as seen in the tuning fork STM measurements, 8.10. For a given perturbation potential of the tip the CDW energy can be minimized by adapting the local phase shape. Here, arises already the difference to the treatment, which were deduced for pinning impurities [87, 88]. Since the tip potential $V(x)$ is larger than the typical period of the charge density wave with $2\pi/Q \sim 2.5nm$, hence in the first assumption the amplitude order parameter is not affected, by the potential $V(x)$.
Further, an important role is played by the boundary conditions of the CDW. Here, we assume an overall pinning at a certain initial phase parameter, according to the experimental findings. Thus, the pinned state is only defined by modulo 2π, allowing a qualitatively different representation of the CDW by the existence of perturbation introducing an integer number N of phase rotations between the boundaries, $2\pi N$. The integer number N, is further called the "winding number" of the given order parameter configuration.

The minimized energy in the subspace of a given winding number was calculated by the group of Erio Tosatti *et al.*, for a given amplitude of the perturbation potential $V(x)$. The evolution of the energies is shown in the figure 8.12, for a Lorentzian tip potential mimicking a conical tip approaching the surface.
The energy evolutions for different winding numbers N is plotted and it can be seen: Each solution branch is crossing sharply each other at specific distances, where the cross over points are marked with dotted circles. The CDW phase winding number changes at these cross over points from the state N to a winding number $N \pm 1$. Here, the inset shows the different solution for different winding numbers, where the full line is the amplitude order parameter and the dashed line the phase order. Each solution introduces a symmetry difference, making it impossible to have a smooth transition between two states. Where for $N = 1$ and $N = 2$ an extra $2\pi N$ CDW phase is locally pumped beneath the tip. This mechanism is provided by the phase slip. A tip oscillation around these cross over points, will result in a hysteresis cycle in the tip mechanics, which explains the giant dissipation peaks despite the extreme low frequencies of the cantilever oscillation, compared with the dielectric relaxation frequency measured in the transport measurements with applied alternating voltage.
In order to regard the picture to the measured height of the dissipation peaks from the experiments, we have to consider the area of the hysteresis cycles enclosed at the cross over points. It is expected, that the area is related to the angle between the energy curves α and the average slope at the crossing point β. Thus the dissipated energy is approximately $W \propto \sin\alpha \cos^{-2}\beta$. As seen in the plots, the shape of the energy curves $E(d)$, that depend on these two parameters, has an opposing effect on the height of the peaks, as the tip approaches the surface. A decreasing α would decrease the dissipation area and an increasing β would increase the dissipation, which leads to the full picture explaining the non-monotonic peak intensity observed in experiments.

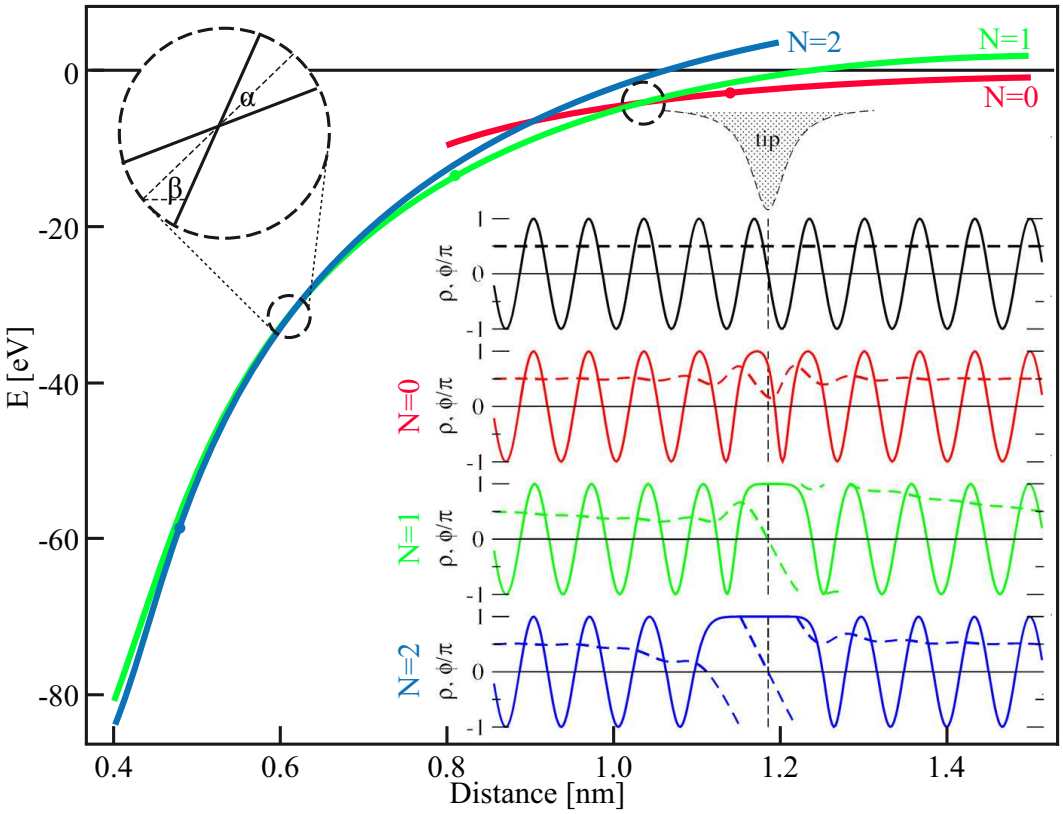

Figure 8.12. The Energy as a function of the distance for the elastic CDW model under the tip perturbation. The reported solutions are for different winding numbers N. The dashed circles are the cross over points for the solutions. The inset illustrates the perturbation states of the CDW, where the full lines are the density modulation $\rho(x)$, dashed lines are the phase order parameter $\phi(x)$. From top to bottom indicates the states for increasing perturbation potential. Adapted from reference [92]

8.9 CO deposition

Despite the amazing finding of the dissipation spikes and the explanation of the non-monotonic behavior of the dissipation maxima by the cross over of the winding numbers of the phase order parameter of the CDW, an open question remains. Is it possible to control the non-contact friction or better is there a possibility to switch it ON or OFF.

In order to investigate this effect, we performed an addition set of experiments. It is known [87, 88], that the formation of the coherent electron state is influenced by the defect density pinning the local phase parameter. An increased defect density with a dipole moment can perturb the CDW globally so much, that a coherent state is now longer accessible or energetically favorable, as shown in [93].

In the experiment, we choose to deposit CO molecules on the surface, which have a dipole moment, and are able to be removed fully above the desorption temperature of $T \sim 70K$. Thus, we are able to suppress the creation of the CDW at the surface and monitor the dissipation.

To be sure, that the suppression of the CDW is correct and not due to a surface

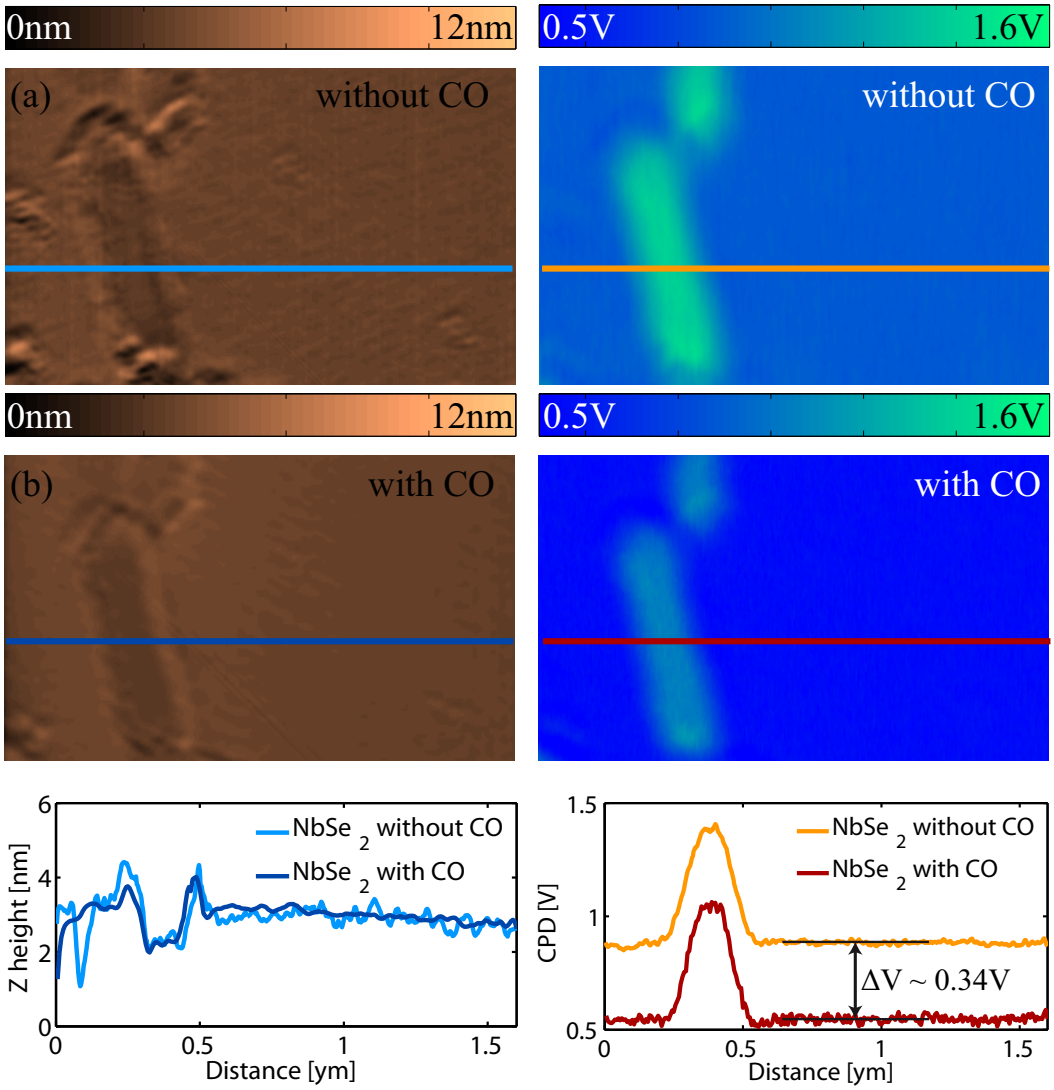

Figure 8.13. The left figure column shows the topography of $NbSe_2$ with and without CO molecules, with a corresponding cross section of the image below. Indicating that the measured topography does not change upon the CO deposition. However, the right column shows the work function maps of the same region, with exactly the same color coding. Here, the cross section shows a clear difference in the CPD, due to the CO molecules changing the surface dipole. Hence, a constant voltage difference of $\Delta V \sim 0.34V$ is globally detected. Image parameters: $f_{2nd} = 89.8kHz$, $A_{2nd} = 0.4nm$, $k \approx 0.2N/m$, $Q_{2nd} \approx 600000$, $U_{ac} = 0.2V$.

artifact, we deposited the CO molecules in-situ. This means we scanned and stayed close to the surface in order to remain exactly at the same position, before and after CO deposition.
The CO was deposited at a pressure of $p_{deposite} \approx 5 \cdot 10^{-8} mbar$ and for $t_{deposite} = 2min$. The deposition rate as well as coverage could not be determined, since the cryostat itself acts as a vacuum pump, making it impossible to estimate the amount of the CO molecules reaching the surface. However, the deposition could be confirmed

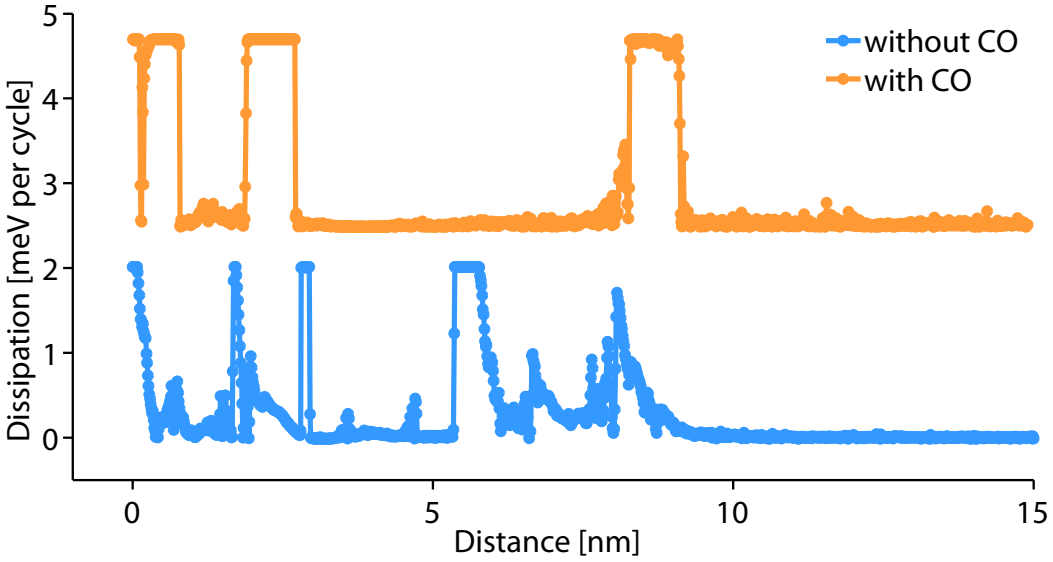

Figure 8.14. The spectroscopy on $NbSe_2$ with and without the CO molecules is shown. The dissipation map with the CO still shows two distinct maxima. However, one notices that the forest of dissipation maxima has cleared out and became more distinguishable. Spectroscopy parameters: $f_{1st} = 14.4kHz$, $A_{1st} = 2nm$, $k \approx 0.2N/m$, $Q_{2nd} \approx 900000$.

to be successful, judging from the topography scans with the accompanied KPFM. Here, the contact potential shows a clear difference between the clean $NbSe_2$ surface and the CO covered one, compare figure row (a) and (b) of 8.13. As a matter of fact, due to the in-situ deposition, we could remain at the exact same position on the surface, seen in the figure 8.13. The comparison of the topography, see the line scan, shows no change.
Nevertheless, the contact potential maps of the same regions show a clear difference for the same color coding. Here, a global constant offset of the CPD, $\Delta V \sim 0.34V$, is measured due to the deposition of the CO. Confirming the successful deposition of an addition dipole layer on the surface.
The figure 8.14 shows, two force distance spectroscopies, one without and with CO. The spectroscopy before deposition clearly shows the mentioned train of dissipation maxima. However, the spectroscopy after the deposition shows a reduced number of dissipation maxima. The remaining dissipation spikes leave an open question.
One possible dissipation mechanism could be the periodic lattice distortion of the $NbSe_2$ crystal itself. If we recall the mentioned theory of the CDW formation, we acknowledge, that the electron modulation results purely from previous the phase transition of the crystal, namely the periodic lattice distortion. The lattice modulation and the CDW is only stabilized by the electron-phonon coupling below the critical temperature [75]. Hence, the local phase slip events occurring on the perturbation of the tip potential is affecting purely the phase order parameter of the surface CDW. However, the electron modulation has a coherence length on the orders of micrometer in $NbSe_2$ [88]. Thus, we can assume, that the periodic lattice distortion is not affected by a local nanometer sized perturbation, due to the elec-

tron phonon coupling to the micrometer large coherent object. This means, that the energy barrier, which is needed to be overcome in order to perturb the lattice distortion is to high for the tip potential.
However, in case of the CO deposition, where we believed that the CDW at the surface is completely suppressed [93]. The stabilization mechanism of the lattice distortion, namely the electron-phonon coupling, is suppressed as well. Then the energy barrier of the periodic lattice distortion is greatly reduced, and the lattice reconstruction below the phase transition is extremely fragile upon external perturbations, namely the tip potential. Due to the fact, that the normal crystal structure is more stable any external local perturbation would destroy locally the reconstruction.
In case of the tip potential, there could be sufficient large interaction strength at a certain distance above the surface, to overcome the stabilizing energy barrier. An oscillation around that point, would result in an adhesion hysteresis within the each oscillation cycle, causing enormous non-contact friction maxima. Thus, I in my humble opinion believe that this could be a suitable dissipation mechanism for observation in the experiments 8.14.
Further, theoretical studies are necessary to confirm these statements, however, $NbSe_2$ accompanied with the charge density wave state has an enormous potential for non-contact friction studies.

8.10 Conclusions

The non-contact friction study of niobium-diselenide, $NbSe_2$, below the charge density wave transition revealed a new aspect of dissipation mechanisms, which were not observed to this day [92, 94]. The remarkable train of dissipation maxima and their magnitude, 8.7, 8.10, as seen in these experiments, show further potential for investigations and possible applications. Since, the energy loss spikes are at discrete points above the surface and are able to be extended for large tip sample junctions with an applied bias voltage 8.9, we could think of a possible non contact friction break with switchable capability. Furthermore, thanks to the theoretical work of the group of Prof. Dr. Erio Tosatti *et al.*, the mechanism of the dissipation maxima, was found and proven to be the local perturbation of the phase order parameter of the coherent CDW state. Where, the tip potential acts as a local perturbation center, deforming and introducing a local 2π phase slip, with a reshaping of the CDW locally under the tip, which made any transition between the integer winding number N of the phase slip impossible, 8.12.
However, an open quest remains for the CO experiments, where the total suppression of the maxima were not successful and some maxima remain 8.14. In my humble opinion, the PLD destruction of the crystal is here the most prominent candidate for the dissipation mechanism. Nevertheless, further studies remain to clarify the open questions on $NbSe_2$. Where the most striking fact is already settled, non-contact friction is not negligible anymore.

9 Strontium Titanate

Perovskites, like strontium titanate $SrTiO_3$, have been heavily studied since the recent past, due to their structural and electronic phase transitions [95–98]. Strontium titanate (STO), at room temperature is a cubic centered crystal, while it changes below the critical transition temperature $T_c = 105K$ to an orthorhombic crystal structure [99]. With the new crystallographic phase the electric properties change as well. STO undergoes the transition to a new electric phase, known as paraelectric phase [100–102]. Furthermore, it is known that the paraelectric phase undergoes a second order phase transition to the ferroelectric state at $T_{PE\rightarrow FE} \approx 18K$ [103–105], depending on the doping concentration. It is even stated, that the pure STO crystal exhibits a third transition from the paraelectric state to the Quantum paraelectric state at $T_{PE\rightarrow QFE} < 3K$ [106, 107].
The dielectric response is extremely large, of the orders of $\epsilon_r > 310$, rising up at low temperatures to $\epsilon_{r,\ LT} > 10000$ [107]. This makes it particularly interesting for the use of high power capacitors.
Despite of the wide range investigations, by means of transport measurements, electron energy loss spectroscopy (EELS), microwave loss experiments or x-ray diffraction, almost no study is done about the friction behavior of the perovskites. Here, we want to present the preliminary studies on the non-contact friction measured by means of pendulum AFM.

9.1 Structural properties of $SrTiO_3$

Perovskites, obeying the general formula ABX_3, are compounds consisting cations $A,\ B$ in equal ratio with an anion X, which is usually oxygen. From the structural point of view, perovskites are made of corner sharing octahedra with the B side inside. [97] In the case of STO, it is the TiO_6 representation, which is often used.
At room temperature the STO crystal is in its highest symmetry phase, the cubic centered, see Figure 9.1(a). In the cubic phase, each oxygen perfectly bisects a pair of nearest neighboring titanium atoms.
For low temperatures the crystallographic picture changes, even though that the literature is not clear about the true nature of the reconstruction, many studies [95, 97, 101] relate the crystal properties of STO to the existence of an orthorhombic unit cell. In this chapter, we will refer further on to the new crystal structure of STO as the orthorhombic reconstruction, as seen in figure 9.1(b). There the oxygen atoms, in plain of the titanium layer, shift their positions, that the octahedra rotates alternately form one unit cell to the next. Meanwhile the oxygen layer in the plain of strontium atoms remain at their positions.
The orthorhombic phase can establish different symmetry domain. Thus, it is common to introduce a symmetry order parameter of STO, with a tri-directional in plane axis.

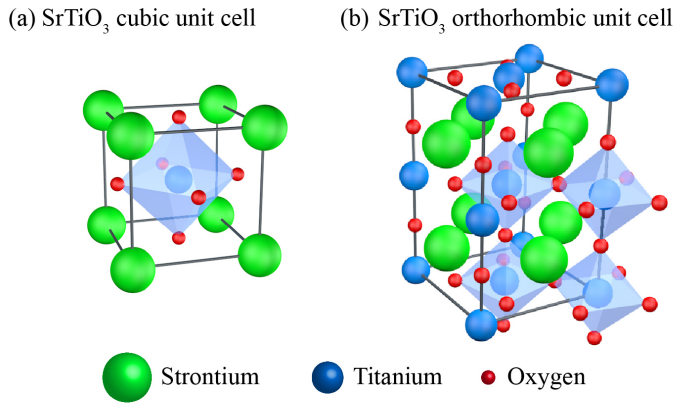

Figure 9.1. The left (a) shows the B cubic centered structure of STO, where the right (b) illustrates the low temperature orthorhombic reconstruction. The strontium atoms are green, titanium atoms blue, oxygen atoms red. Figures adapted from reference [97].

Here, we want to stress out, that this thesis is not dedicated to an analysis of the crystallographic study. Furthermore, the keen interest is to study the non-contact friction properties in the vicinity of the phase transitions itself.

9.2 Sliding over Phase Transition

The idea of replacing a "dead" substrate, meaning a passive material, with a "live" material accompanied with phase transitions was proposed, by Benassi *et al.* [108]. The knowledge gained by studying the frictional properties and their change on the same material, has a larger potential of gaining an access to a control of the friction at the anomaly of the phase transition. Benassi *et al.* addresses and answers three questions, in the following we cite directly the stated questions from the reference (ref):

1. What is the frictional coupling mechanism between tip motion and a substrate structural phase transition?
2. What is the distinguishing element of the phase transition to the background friction?
3. Could one achieve friction control through external field that influence the substrate order parameter?

The theoretical studies are concerning the friction mechanism of a tip in contact with the surface. Our results are for the non-contact friction regime. Thus, we can give an answer to the second question, regarding the distinguishable element of the non-contact friction at the phase transition towards the background. The coupling mechanism of the tip motion to the substrate is due to the phonon coupling [3], which is invoked the by the linear response of the standard "golden rule", where the average power dissipation at the transition is:

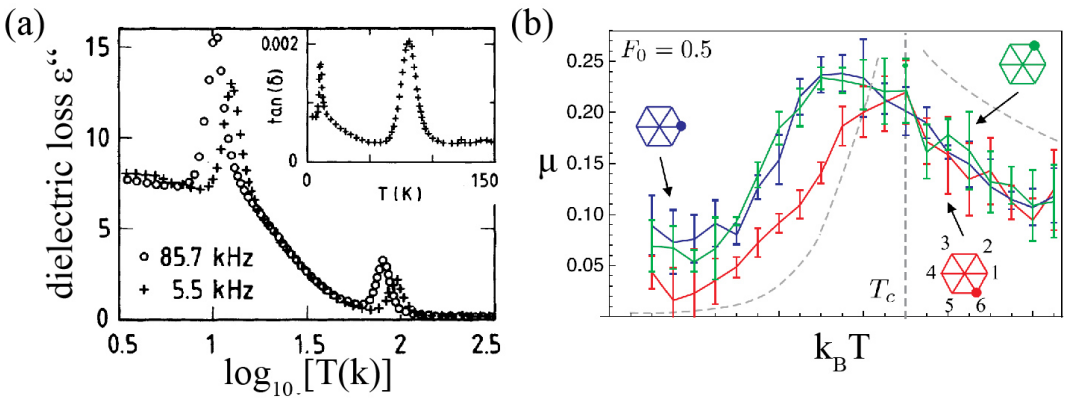

Figure 9.2. On the left, the dielectric response measurements indicate the existence of the two phase transitions. One structural at $T \approx 105K$ and the electronic at $T \sim 20K$. On the left is the expected friction coefficient shown for the crossing of the structural transition and the three order parameters, calculated by Benassi *et al.*, with the maximum at the transition temperature. Figures adapted from references [100,108]

$$\langle P \rangle \propto \sum_k \omega_k |V_k|^2 \chi''(\mathbf{k},\ \omega_k) \tag{9.1}$$

where V_k is the Fourier expansion coefficient of the slider-substrate potential, $\omega_k = \mathbf{k} \cdot \mathbf{v}$, and $\chi''(\mathbf{k},\ \omega_k)$ is the imaginary part of the substrate density-density correlation function, as in the electron energy loss.
Since, $\mathbf{k} \cdot \mathbf{v}$ is a low frequency, the predictions expect a rise in the friction, due to the increased accessibility of the low frequency modes originating from the softening of the displacive mode and therefore a peaking of the friction at the critical temperature of the phase transition, see figure 9.2(b).
In addition, the paper states a possibility of controlling the friction by an externally applied field E, which can couple to the order parameter of the substrate in the form $u \cdot E$, where u is the displacement order parameter of the averaged distortion of atoms. Thus, the applied field induces an order parameter switching between the stable configurations. Due to this, the friction is theoretically predicted to increase.

9.3 Preparation of STO

In this study, we used a single crystal of strontium titanate (100) with 1% niobium doping, bought from the MTI Corporation. The niobium doping is necessary to perform STM measurements. The crystal was cleaned with solvents in an ultrasonic bath for $t = 15min$ to remove the surface contaminants from the manufacturing and transport. The STO was then mounted on a molybdenum UHV sample holder and introduced in the vacuum. Since, the crystal was polished to obtain the desired surface flatness, we had to anneal the surface in order to retrieve a stable reconstruction. The crystal was initially annealed for several hours at temperatures of $T_{anneal} = 1200K$ for $t_{anneal} = 15h$. After the long term annealing, we performed short flash annealing cycles, which means heating the sample to $T \approx 1200K$ for $t_{flash} = 10min$. This was done by means of E-Beam heating.

The flashing cycles have been repeated 10× to obtain surface steps with a clear reconstruction, The STM images of the clean sample are shown in figure 9.3.

9.4 Non-contact friction over phase transition

After the successful preparation of STO, we analyzed the non-contact friction behavior over the structural phase transition. To stay in a constant distance above the surface during the temperature sweep is difficult, due to the thermal expansion coefficient of the sample and the whole microscope. The thermal drift would ram the probe in the surface and crash it, if there is no active distance control. The frequency shift feedback, which usually regulates the distance, is not useful unless one knows the temperature dependent frequency change of the free cantilever.
Therefore, a temperature sweep of the free cantilever needed to be acquired. The thermal dependence of the Young's modulus is given by the Wachter-formula [109]:

$$E(T) = E_0 - B \cdot T \cdot e^{\frac{T_0}{T}} \tag{9.2}$$

$$\Rightarrow \omega(T) = \alpha^2 \frac{t}{L^2} \sqrt{\frac{E(T)}{12\rho}} \tag{9.3}$$

where $\alpha = 1.875$, t the thickness, L the length and ρ the density of silicon. The fitted temperature dependence resonance curve of the probe is then used to establish a constant frequency shift feedback, to stay at a constant interaction force condition, even when the temperature is swept. Due to the fact that the tip-sample interaction strength is widely independent of the temperature, we believe that the probe is therefore at a constant distance from the sample as well.
For the measurements shown in figure 9.4, three temperature sweeps have been performed, always from $T = 77K$ to $T = 140K$. The plotted temperature is ranging form $85K$ to $127K$, especially around the predicted $T_c = 105K$ for STO. Since, the dielectric response measurement of figure 9.2(a), indicate a phase transition at lower temperatures, the maximum for the low frequency response is around $T_c = 90K$.

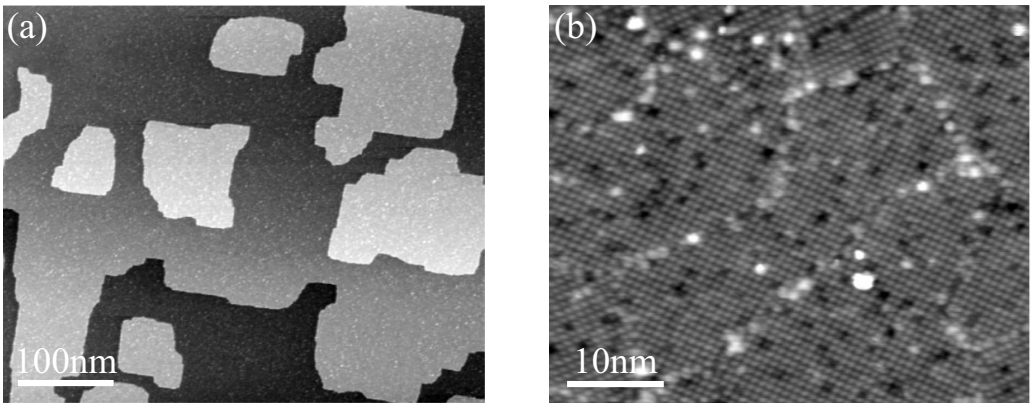

Figure 9.3. The left (a) shows tuning fork STM measurements of the stepped surface reconstruction of STO, where the right (b) illustrates domain creation below the transition temperature for $T = 77K$.

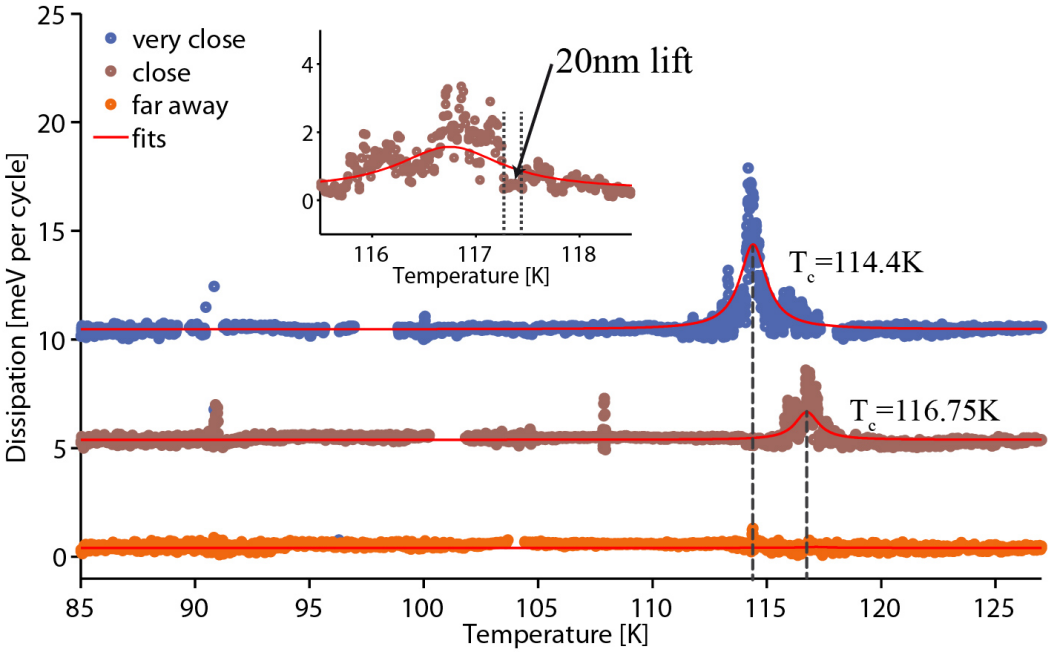

Figure 9.4. Three temperature sweeps over the structural phase transition of STO are plotted. The dissipation peak rises, when the tip sample distance is decreased and therefore the interaction is increased. Interestingly the dissipation maxima also appears for lower T_c in case of larger interaction. Each curve has been shifted by $5meV$. Spectroscopy parameters: $f_{1st} \sim 14kHz$, $A_{1st} = 15nm$, $U_{CPD} = 720mV$.

No dissipation peak is observed in the case of large separation distances for the whole temperature range. If the probe is set closer to the surface, while sweeping the temperature, we observe a maximum at $T_c = 116.75K$. We are certain, that the dissipation maximum is due to the interaction with the surface. To prove this, we retracted the tip by $20nm$ above the surface, and the dissipation dropped off to the free cantilever values, see inset of figure 9.4. After approaching the tip again to the surface, the measured dissipation increased again.
The same was done for the temperature sweep, where the tip was set very close above the surface. Firstly, we observed by a factor of 4 larger dissipation maximum, compared to the previous one. Secondly, the center of the maximum shifted towards lower temperatures to $T_c = 114.4K$.
In no case, we observed an increased dissipation for temperatures below $T < 100K$ [100]. However, the temperature sweeps have been performed at a compensated contact potential, meaning that there is in principal no electric field present in the tip sample junction. Thus, the oscillating tip has no effect on the dielectric response. Nevertheless, we performed on purpose sweeps with an electric field and still did not observe any effect on the dissipation within this temperature range.
Therefore, we believe, that the observed dissipation maxima is the phononic friction, due to the mechanism proposed by Benassi *et al.* [108]. It is known, that for niobium doped STO the structural phase transition shifts slightly above $T_c > 105K$ [110], This corresponds to our results. The fact that the dissipation drops off rapidly for increasing distances, could be due to the decreasing phonon coupling to the tip

motion. This could be caused by the rapidly decreasing VAN DER WAALS force with distance. In addition the maxima rises in magnitude for stronger tip sample interaction, which was proposed as well.
However, further studies on the non-contact friction behavior over the structural phase transition have to be done, to rule out the doubts and reveal the true nature of the measured non-contact friction.

9.5 Paraelectricity, quantum ferroelectricity and non-contact friction

Above the structural transition of STO at temperatures of $T = 142K$ we performed a bias spectroscopy, see figure 9.5. The Dissipation map shows an increasing loss due to the Joule dissipation mechanism, regarding the high dielectric constant of STO, $\epsilon_r = 310$ [107]. In addition, we observed a bending of the contact potential, which is visible in the minima of the superimposed constant frequency shift contours. The extracted spectra of the dissipation and the frquency shift, see figure 9.5(b, c), show no indication of an anomaly. However, this changes drastically if STO is cooled below the paraelectric phase transition.
STO at room temperature has a cubic unit cell, which does not allow creation of dipoles. However, below the structural phase transition $T_c \sim 110K \pm 7K$ and with the creation of an orthorhombic unit cell, the crystal changes also from a dielectric media to a paraelectric one. The paraelectric phase manifests itself with a random dipole orientations in the absence of an electric field. If a sufficiently large external electric field is applied, an energy barrier can be overcome and the dipoles align anti parallel to the field to reduce the field strength. Upon the removal of the electric field the dipoles randomize their orientation to achieve the ground state.
For pure and niobium doped STO a second electronic phase transition at $T_{PE \to FE} \sim 18K \pm 3K$ is possible. Below the transition, the crystal becomes ferroelectric. Ferroelectric materials have permanent electric dipoles even in the absence of an externally applied electric field. For the dipoles it is favorable to align parallel with each other. Nevertheless, in oder to minimize the total energy of the crystal, domains of opposing orientation are established. A given orientation of a dipole domain, can be switched with a sufficiently large electric field [111].
The non-contact friction behavior of STO changes drastically in the ferroelectric phase. In the figure 9.6 (a) a bias spectroscopy map is shown. Again a remarkable train of dissipation maxima is observed in the spectra. The superimposed constant frequency shift contour indicates for the first two maxima, see $\Delta f = -13Hz,\ -34Hz$, that they are force driven. The magnitude of the dissipation maxima, of the first pair, is equal for every applied bias voltage. However, the second pair of maxima do not persist at the contact potential, see $\Delta f = -45Hz, -80Hz$ and the peak intensity decreases below the detection level of the probe.
The origin of the maxima remains unclear to this point. However, one important factor is already clear, the paraelectric phase influences the measured dissipations behavior. Since, no features have been observed above the structural phase transition.
The niobium doped strontium titanate crystal can exhibit an XY quantum ferro-

electric state, measured by J.G. Bednorz and K.A. Müller [107]. This would manifest itself in the STO as a dipole domain ordering in the XY plane, with a dimensionality of $d = 2$. An electric field or a mechanical stress uni-axial perpendicular to the planar oriented dipoles, can switch the domains above critical threshold barrier. It was proposed, that the system is an XY, $n = 2$ ferroelectric with a quartic anisotropy. Thus, it can be assumed, that the energy barriers for each polarization axis is a priori not equal. This means, that the switching of each orientation towards the energetically more favored, switches at a different electric field strengths.
Thus, one could expect upon a domain change a non-linear electronic response, lead-

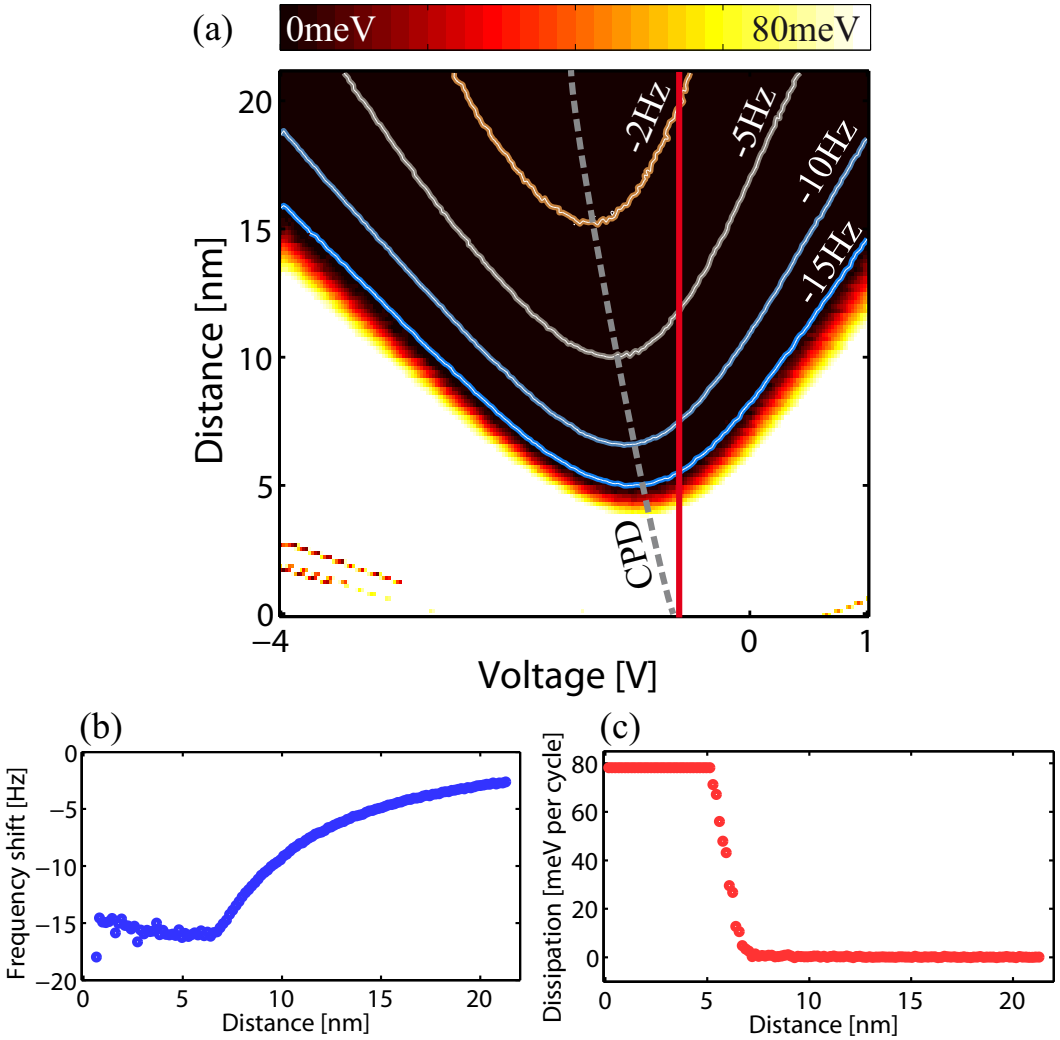

Figure 9.5. Figure part (a) shows the bias spectroscopy map of STO at $T = 142K$. The dissipation map is governed by the Joule dissipation, since the permittivity constant is $\epsilon_r = 310$, according to the manufacturer (MTI corporation). Four constant frequency shift contours are superimposed to show the bending of the CPD, the minimum of each parabola. No features have been observed in the dissipation map or the single spectra (c), as well as the frequency shift curve (b). Spectroscopy parameters: $f_{1st} \sim 14kHz$, $A_{1st} = 5nm$, $\Delta f = -2Hz, -5Hz, -10Hz, -15Hz$.

ing to an energy loss upon switching, causing the dissipation in the bias spectroscopy, 9.6(a). In addition, we have to consider the reversibility of the domain change upon the electric field or uni axial stress, due to the symmetry in the applied bias voltage with respect to the contact potential. Secondly, domain switching on the uni-axial stress is observable at the contact potential in the absence of an electric field. From this point, we could state, that the multiplet of spikes is due to the domain switching on the surface as well as in the bulk of the STO crystal. Thus, each pair is due to the XY domain switching in a plane, furthermore the absence of other pairs at the contact potential is understandable. Here, the VAN DER WAALS interaction is only capable to exert stress on the first layer [46], while the stress is attenuated in the

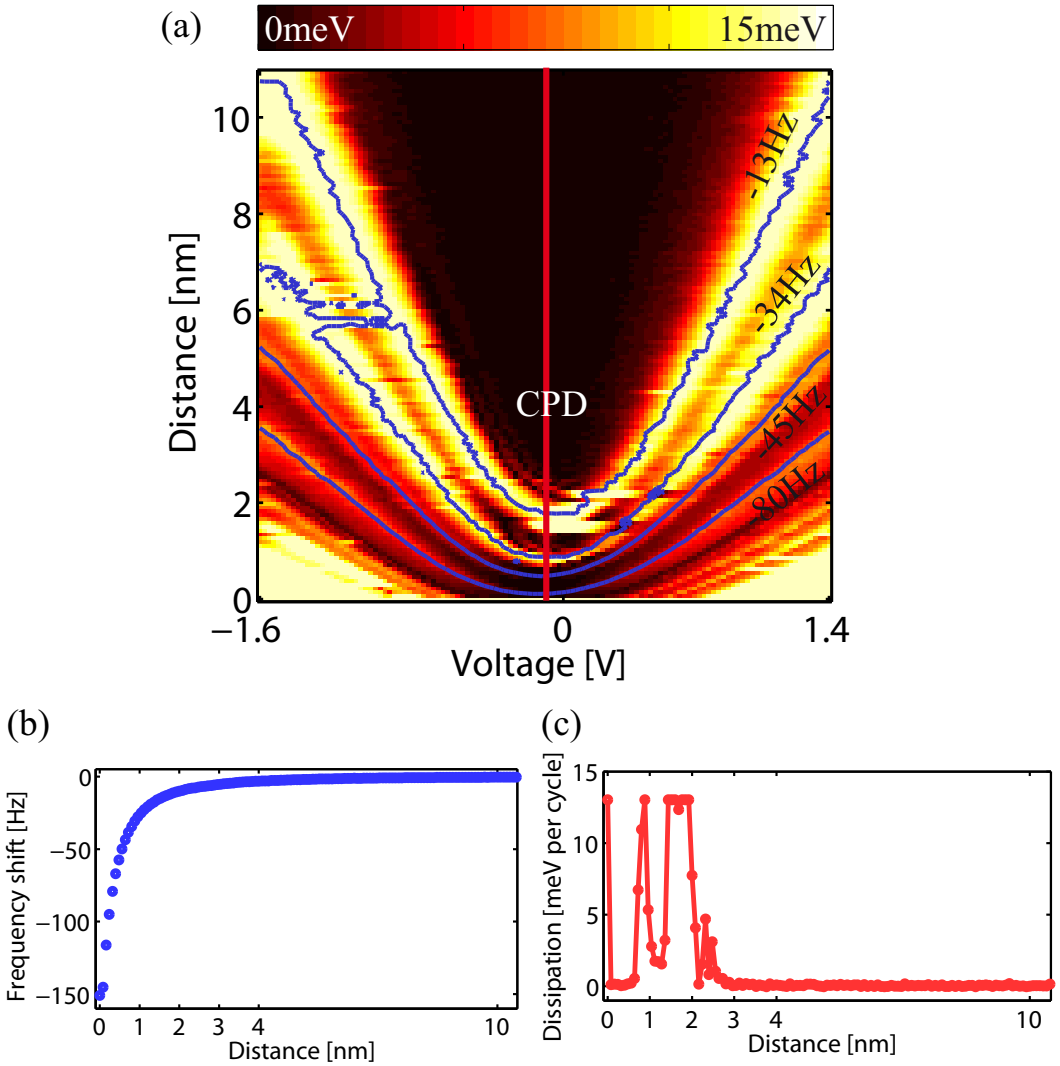

Figure 9.6. Figure part (a) show the bias spectroscopy map of STO at $T = 5K$. The dissipation map changes drastically. Here another train of dissipation maxima is observed. Four constant frequency shift contours are superimposed to show again the Spectroscopy parameters: $f_{1st} \sim 14kHz$, $A_{1st} = 2.5nm$, $\Delta f = -13Hz, -34Hz, -45Hz, -80Hz$, $U_{CPD} = -120mV$.

bulk towards the next layer and is below the critical stress barrier in oder to switch the domains.
The analysis of the observed dissipation maxima in niobium doped strontium titanate is preliminary. Thus the possible explanation must be proven further in order to maintain knowledge of the true nature of the non-contact friction maxima in STO.

9.6 Conclusions

The interesting result on th phase transitions of strontium titanate leave a wide area of further investigations. In our opinion, we have observed the proposed [108]dissipation maxima at the structural phase transition 9.2(b). This kind of peak is expected, because near the structural transition the system becomes very slow and soft, qualitatively because there is a proliferation of domain walls, defects, disorder in the distortive part of the crystal structure, see figure 9.4.
Furthermore, we observed a remarkable multiplet of dissipation spike at low temperatures, 9.6(a), below the paraelectric phase transition $T_{P\rightarrow F} \sim 18K \pm 3K$. Here, I want to stick to the possible candidate for the loss mechanism proposed by J.G. Bednorz and K.A. Müller in [107]. Where the energy loss occurs at the dipole domain switching. This proposal is still far from being proven, but it offers an answer to all observables seen in the bias spectroscopy 9.6.
However, the field of non-contact friction offers a wide range and rich physics of energy loss mechanisms, which is still poorly studied. The origins of friction and non-contact friction at the nanoscale leave after such a long history of investigations, still a book of open questions, which wait to be discovered and understood.
Eventually, applications, like non-contact brakes with a switching capability, would become accessible in the near future, having the advantage of dissipating the kinetic energy in the absence of material loss. However, the understanding of the non-contact friction mechanism would be of great benefit for the MEMS and NEMS technology.

Bibliography

[1] Mo, Y., Turner, K. T., and Szlufarska, I. *Nature* **457**(7233), 1116–9 February (2009).

[2] E. Meyer, R. Overney, K. Dransfeld and Gyalog, T. *Nanoscience: friction and rheology on the nanometer scale*. World Scientic, (1998).

[3] Kisiel, M., Gnecco, E., Gysin, U., Marot, L., Rast, S., and Meyer, E. *Nat. Mater.* **10**, 119–122 (2011).

[4] Binnig, G., Quate, C., and Gerber, C. *Phys. Rev. Lett.* **56**(9) (1986).

[5] Albrecht, T. and Grütter, P. *J. Appl. ...* **69**(2), 668 (1991).

[6] Ohnesorge, F. and Binnig, G. *Science (80-.).* **260**(5113), 1451–6 June (1993).

[7] Bennewitz, R., Gnecco, E., Gyalog, T., and Meyer, E. *Tribol. Lett.* **10**(1-2), 51–56 (2001).

[8] Gross, L., Mohn, F., Liljeroth, P., and Repp, J. *Science (80-.).* **324**(5933), 1428–31 June (2009).

[9] Giessibl, F. *Science (80-.).* (13) (1995).

[10] Bhushan, B. and Marti, O. *Nanotribology and Nanomechanics I.* Springer Berlin Heidelberg, Berlin, Heidelberg, (2011).

[11] Persson, B. *Sliding friction.* Springer, (1998).

[12] E. Gnecco, E. M. *Fundamentals of Friction and Wear on the Nanoscale.* Springer, (2007).

[13] Morita, S., Wiesendanger, R., and Meyer, E. *Noncontact atomic force microscopy.* Springer, (2002).

[14] Guggisberg, M., Bammerlin, M., Loppacher, C., Pfeiffer, O., Abdurixit, a., Barwich, V., Bennewitz, R., Baratoff, a., Meyer, E., and Güntherodt, H.-J. *Phys. Rev. B* **61**(16), 11151–11155 April (2000).

[15] Giessibl, F. *Rev. Mod. Phys.* **75**(July) (2003).

[16] Hudlet, S., Saint Jean, M., Guthmann, C., and Berger, J. *Eur. Phys. J. B* **2**(1), 5–10 April (1998).

[17] Bruder, C. *Phys. unserer Zeit* **28**(4), 149–154 (1997).

[18] Rodriguez, A. W., Capasso, F., and Johnson, S. G. *Nat. Photonics* **5**(4), 211–221 April (2011).

[19] Gotsmann, B., Seidel, C., Anczykowski, B., and Fuchs, H. *Phys. Rev. B* **60**(15), 11051–11061 October (1999).

[20] Kawai, S., Canova, F., Glatzel, T., Foster, A., and Meyer, E. *Phys. Rev. B* **84**(11), 115415 September (2011).

[21] Musser, A. (May), 1–25 (2009).

[22] Kantorovich, L. *J. Phys. Condens. Matter* **945** (2001).

[23] Trevethan, T. and Kantorovich, L. *Nanotechnology* **18**(8), 084017 February (2007).

[24] Asaki, N. S. and Sukada, M. T. *Jpn. J. Appl. Phys.* **39**(12), 1334–1337 (2000).

[25] Anczykowski, B. and Gotsmann, B. *Appl. Surf. ...* **140**(3-4), 376–382 February (1999).

[26] Stipe, B., Mamin, H., Stowe, T., Kenny, T., and Rugar, D. *Phys. Rev. Lett.* **87**(9), 096801 August (2001).

[27] Trevethan, T. and Kantorovich, L. *Nanotechnology* **15**(2), S44–S48 February (2004).

[28] Trevethan, T. and Kantorovich, L. *Nanotechnology* **17**(7), S205–12 April (2006).

[29] Gauthier, M. and Tsukada, M. *Phys. Rev. B* **60**(16), 11716–11722 October (1999).

[30] Garcia, R. and Herruzo, E. *Nat. Nanotechnol.* **7**(4), 217–26 April (2012).

[31] Lifshitz, R. and Roukes, M. *Phys. Rev. B* **61**(8), 5600–5609 February (2000).

[32] Houston, B. and Photiadis, D. *Appl. Phys. ...* **80**(7), 1300 (2002).

[33] Zener, C. *Phys. Rev.* **230**(1937) (1938).

[34] Berry, A. S. N. and S., B. *Anelastic Relaxation In Crystalline Solids*. Academic, (1972).

[35] Rast, S., Gysin, U., Ruff, P., Gerber, C., Meyer, E., and Lee, D. W. *Nanotechnology* **17**(7), S189–94 April (2006).

[36] Haucke, H., Liu, X., and Vignola, J. *Appl. Phys. Lett.* **86**(18), 181903 (2005).

[37] Hutter, J. and Bechhoefer, J. *Rev. Sci. Instrum.* **64**(7), 1868 (1993).

[38] Yang, J., Ono, T., and Esashi, M. *Appl. Phys. Lett.* **77**(23), 3860 (2000).

[39] Sharpe, W. and Yuan, B. *IEEE* , 424–429 (1997).

[40] D. Bellet, P. Lamagnère, A. Vincent, Y. B. *J. Appl. Phys.* **80**(7), 3772 (1996).

[41] Gnecco, E., Bennewitz, R., Gyalog, T., Loppacher, C., Bammerlin, M., Meyer, E., and Guntherodt, H. *Phys. Rev. Lett.* **84**(6), 1172–5 February (2000).

[42] Bowden, F. P. (1950).

[43] Weber, J. *Phys. Rev.* **101**(6) (1956).

[44] Kubo, R. *Reports Prog. Phys.* **255** (1966).

[45] Kantorovich, L. and Trevethan, T. *Phys. Rev. Lett.* **93**(23), 236102 November (2004).

[46] Schiessel, H., Oshanin, G., Cazabat, A., and Moreau, M. *Phys. Rev. E* **66**(5), 056130 November (2002).

[47] Stomp, R., Miyahara, Y., Schaer, S., and Sun, Q. *Phys. Rev. ...* **94**(5), 056802 February (2005).

[48] Volokitin, A. and Persson, B. *J. Phys. Condens. ...* **11**, 345–359 (1999).

[49] Volokitin, A. and Persson, B. *Phys. Rev. B* **63**(20), 205404 April (2001).

[50] Volokitin, A. and Persson, B. *Rev. Mod. Phys.* **79**(4), 1291–1329 October (2007).

[51] Dorofeyev, I., Fuchs, H., Gotsmann, B., and Wenning, G. *Phys. Rev. B* **60**(12), 9069–9081 (1999).

[52] Gysin, U., Rast, S., Kisiel, M., Werle, C., and Meyer, E. *Rev. Sci. Instrum.* **82**(2), 023705 February (2011).

[53] Giessibl, F. *Phys. Rev. B* **56**(24), 16010–16015 December (1997).

[54] Giessibl, F. and Bielefeldt, H. *Phys. Rev. B* **61**(15), 9968–9971 April (2000).

[55] Sarid, D. *Scanning force microscopy.* Oxford University Press, (1991).

[56] S. Sadewasser, T. G. *Kelvin Probe Force Microscopy.* Springer, (2012).

[57] Sarid, D. *Kelvin Probe Force Microscopy.* Wiley-VCH Verlag GmbH & Co. KGaA, (2007).

[58] Nonnenmacher, M. *Appl. Phys. ...* **58**(25), 2921 (1991).

[59] Zerweck, U., Loppacher, C., Otto, T., Grafström, S., and Eng, L. *Phys. Rev. B* **71**(12), 125424 March (2005).

[60] Loppacher, C., Bennewitz, R., and Pfeiffer, O. *Phys. Rev. B* **62**(20), 13674–13679 November (2000).

[61] Bennewitz, R., Barwich, V., and Bammerlin, M. *Surf. Sci.* **438**, 289–296 (1999).

[62] Bennewitz, R. *J. Phys. Condens. Matter* **18**(26), R417–35 July (2006).

[63] Bennewitz, R., Schär, S., Gnecco, E., Pfeiffer, O., Bammerlin, M., and Meyer, E. *Appl. Phys. A* **78**(6), 837–841 March (2004).

[64] Foster, A., Hofer, W., and Shluger, A. *Curr. Opin. Solid State Mater. Sci.* **5**(5), 427–434 October (2001).

[65] Bombis, C., Ample, F., and Mielke, J. *Phys. Rev. Lett.* **104**(18), 185502 May (2010).

[66] Gross, L., Mohn, F., Liljeroth, P., and Repp, J. *Science (80-.).* **324**(5933), 1428–31 June (2009).

[67] Langewisch, G., Fuchs, H., and Schirmeisen, a. *Nanotechnology* **21**(34), 345703 August (2010).

[68] Mohn, F., Gross, L., Moll, N., and Meyer, G. *Nat. Nanotechnol.* **7**(4), 227–31 April (2012).

[69] Glatzel, T., Zimmerli, L., Koch, S., and Such, B. *Nanotechnology* **20**(26), 264016 July (2009).

[70] Pfeiffer, O., Gnecco, E., Zimmerli, L., Maier, S., Meyer, E., Nony, L., Bennewitz, R., Diederich, F., Fang, H., and Bonifazi, D. *J. Phys. Conf. Ser.* **19**, 166–174 January (2005).

[71] Meyer, G., Gross, L., Mohn, F., and Repp, J. *Chimia (Aarau).* **66**(1-2), 10–5 January (2012).

[72] Li, Y. J., Kinoshita, Y., Tenjin, K., Ma, Z. M., Kou, L. L., Naitoh, Y., Kageshima, M., and Sugawara, Y. *Jpn. J. Appl. Phys.* **51**, 035201 February (2012).

[73] R. Bennewitz, M. Bammerlin, M. Guggisberg, C. Loppacher, A. Barato, E. Meyer, H.-J. and Güntherodt. *Surf. ...* **27**, 462–466 (1999).

[74] Kumar, B., Bonvallet, J., and Crittenden, S. *Nanotechnology* **23**(2), 025707 January (2012).

[75] Weber, F., Rosenkranz, S., Castellan, J.-P., Osborn, R., Hott, R., Heid, R., Bohnen, K.-P., Egami, T., Said, a. H., and Reznik, D. *Phys. Rev. Lett.* **107**(10), 107403 September (2011).

[76] Moncton, D., Axe, J., and DiSalvo, F. *Phys. Rev. Lett.* **34**(1975), 734–737 (1975).

[77] Marezio, M., Dernier, P. D., Menth, A., and Hull, G. W. *J. Solid State Chemestry* **4**, 425–429 (1972).

[78] G. Grüner. *Rev. Mod. Phys.* **60**(4) (1988).

[79] Rice, T. and Scott, G. *Phys. Rev. Lett.* **35**(2) (1975).

[80] Frohlich, H. *Proc. R. Soc. ...* **223**(1154), 296–305 May (1954).

[81] A. Zettl and G. Grüner. (1983).

[82] A. Zettl and G. Grüner. *Phys Rev. B* **29**(2) (1984).

[83] Lee, P. and Rice, T. *Phys. Rev. B* **19**(April) (1979).

[84] Strogatz, S., Marcus, C., Westervelt, R., and Mirollo, R. *Phys. Rev. Lett.* **61**(20), 2380–2383 (1988).

[85] Fukuyama, H. and Lee, P. *Phys. Rev. B* **17**(2) (1978).

[86] Littlewood, P. and Rammal, R. *Phys. Rev. B* **38**(4), 2675–2690 (1988).

[87] Tütto, I. and Zawadowski, A. *Phys. Rev. B* **32**(4) (1985).

[88] Tucker, J. *Phys. Rev. B* **40**(8) (1989).

[89] Wise, W., Boyer, M., and Chatterjee, K. *Nat. Phys.* **4**(9), 696–699 July (2008).

[90] Ashoori, R. *Nature* (1996).

[91] Sader, J. and Jarvis, S. *Appl. Phys. Lett.* **84**(10), 1801 (2004).

[92] Langer, M., Kisiel, M., and Pawlak, R. *Nat. Mater.* **13**(12), 1–5 December (2014).

[93] Matthias M. May. *Two ways of suppressing charge density waves in 1T-TiSe2.* PhD thesis, Humboldt-University of Berlin, (2010).

[94] Saitoh, K., Hayashi, K., Shibayama, Y., and Shirahama, K. *Phys. Rev. Lett.* , 5 December (2010).

[95] Cowley, R. *Adv. Phys.* **29**(1), 1–110 (1980).

[96] Pynn, R. *Nature* **281**, 433–437 (1979).

[97] Smith, A. *Structural and defect properties of strontium titanate.* PhD thesis, (2012).

[98] Erdman, N., Poeppelmeier, K., and Asta, M. *Nature* **419**(6902), 55–8 September (2002).

[99] Castell, M. *Surf. Sci.* **505**, 1–13 (2002).

[100] Viana, R., Lunkenheimer, P., and Hemberger, J. *Phys. Rev. B* **50**(1), 601–604 (1994).

[101] Saha, S., Sinha, T., and Mookerjee, A. *J. Phys. Condens. ...* **3325** (2000).

[102] Sander, L. and Shore, H. *Phys. Rev. B* **3**(4), 1472–1482 (1971).

[103] Grupp, D. and Goldman, A. *Science (80-.).* **276**(5311), 392–394 April (1997).

[104] Lemanov, V. V., Sotnikov, A. V., Smirnova, E. P., and Weihnacht, M. *Phys. Solid State* **44**(11), 2039–2049 (2002).

[105] Itoh, M., Wang, R., Inaguma, Y., Yamaguchi, T., Shan, Y.-J., and Nakamura, T. *Phys. Rev. Lett.* **82**(17), 3540–3543 April (1999).

[106] Müller, K. and Burkard, H. *Phys. Rev. B* **19**(7) (1979).

[107] Muller, J. G. B. and A., K. *Rhys. Rev. Lett.* **52**(25), 2289–2292 (1984).

[108] Benassi, A., Vanossi, A., Santoro, G., and Tosatti, E. *Phys. Rev. Lett.* **106**(25), 256102 June (2011).

[109] J. B. WACHTMAN, W. E. TEMPT, D. G. LAM, C. S. A. *Phys. Rev.* **122**(6) (1961).

[110] Menoret, C., Kiat, J., Dkhil, B., and Dunlop, M. *Phys. Rev. B* **65**(22), 224104 May (2002).

[111] W. Kleemann and H. Schremmer. *Phys. Rev. B* **40**(10), 7428–7431 (1989).

10 Acknowledgements

To accomplish a PhD is a long and demanding path with a lot of frustration. Thus, it is even more important to have a team around, which supports you in every way. I learned a lot and laughed even more in Basel. Therefor, I thank Prof. Dr. Ernst Meyer, for giving me the possibility to start in his group my Master Project, Master Thesis and now the PhD.
I am glad for the great opportunity to attend so many conferences to broaden my scientific horizon on the one hand and on the other to find so many new friends. Especially, that Mr. Meyer is responsible to send me to the Joint ICTP-FANAS Conference on Nanotribology in Trieste, where I met my wife Dr. Nino Samadashvili.
Nevertheless, the group in Basel has an amazing knowledge base, where so much can be learned from. I thank Dr. Marcin Kisiel in particular, with his broad and fundamental knowledge of physics and the electronics. He was always there to answer my stupid questions and show me how its done. He was open for new ideas and discussions - scientific as well as private. He motivated me, if the measurements were bad, and cheered up with me, when the times were good. His humor made the PhD time fly by.
I want to thank also Dr. Remy Pawlak, a.k.a. Mr. Tuning fork. He, is an amazing young researcher. Full of new ideas and superb in operating the tuning fork. He helped me and Marcin every time, when we needed a beautiful STM/AFM image or a complicated spectroscopy. He was always a good discussion partner, regardless of the topic - physics or life.
I thank also Dr. Thilo Glatzel, who was my supervisor during my Master, who encouraged my decision to start a PhD in AFM. Which also turned out to be in the same group. He is a great person and helps everyone at any time and he is a great resource in the group for any kind of AFM questions. I would like to thank also Dr. Shigeki Kawai, due to his outstanding technical know-how in the field of AFM.
Besides them, I want to thank all the other group members, whom I worked with, for the relaxing and wonderful environment. Especially, Dr.Sascha Koch for the great time during my Master Thesis and the PhD for the breathless laughters we had and for introducing the Feuerzangenbowle tradition in our group at the X-Mas party. Dr. Gregor Fessler for the relaxing Lunch break Frisbee sessions in the summer and the Top Gear broadcast for the winter. Also Dr. Sweetlana Fremy and the "Da müssen ma snaggen" discussions and Dr. Baran Eren, for the good political discussions and for the tasty Turkish Delight sweets, which he brought us every time after his trip to Turkey. Also I like to thank Matthias Wasem, for the music suggestions, Alexander Bubendorf, for the Movie suggestions and Matias Schulzendorf for the tech-talk. Besides them, I thank Urs Gysin, Antoine Hinaut, Laurent Marot, Yves Pellmont, Gino Günzburger, Lucas Moser, Res Joehr, Elcin Külah for the warm atmosphere in the group, which formed a second home for me.

Last but not least, I thank my dearest wife, Dr. Nino Samadashvili, for the great support and love she gave me. All became so much more easy with her. Besides the romantic talk, we had long lasting serious discussion about non-contact and contact friction mechanisms, which made the writing progress of the thesis so much faster.

11 List of Publications

- B. Eren, L. Marot, M. Langer, R. Steiner, M. Wisse, D. Mathys, E. Meyer
  The effect of low temperature deuterium plasma on molybdenum reflectivity
  Nuclear Fusion, **51**, 103025, (2011)

- S. Koch, M. Langer, S. Kawai, E. Meyer, Th. Glatzel
  Contrast inversion of the h-BN nanomesh investigated by nc-AFM and Kelvin probe force microscopy
  J. Phys.: Condens. Matter, **24**, (31), 314212, (2012)

- M. Langer, M. Kisiel, R.Pawlak, F. Pelligrini, G. E. Santoro, R. Buzio, A. Gerbi, G. Balakrishnan, A. Baratoff, E. Tosatti, E. Meyer
  Giant frictional dissipation peaks and charge-density-wave slips at the $NbSe_2$ surface
  Nature Materials, **13**, 173-177, (2014)

12 Presentations

Oral Presentations:

- German Physical Society (DPG), Frühjahrstagung 2010, Regensburg, Germany
- German Physical Society (DPG), Frühjahrstagung 2012, Berlin, Germany
- 15th International Conference on NC-AFM, 2012, Ceský Krumlov, Czech Republic
- 29th European Conference on Surface Science, 2012, Edinburgh, United Kingdom
- Towards Reality in Nanoscale Material VI, 2013, Levi, Finland
- 4th Conference on Advances in Atomic Force Microscopy Techniques, 2013, Karlsruhe, Germany
- i-net Nano, 2013, Basel, Switzerland
- 16th International Conference on NC-AFM, 2013, Maryland, USA
- 5th Conference on Advances in Atomic Force Microscopy Techniques, 2014, Karlsruhe, Germany

Poster Presentations:

- 2th Conference on Advances in Atomic Force Microscopy Techniques, 2010, Karlsruhe, Germany
- Swiss Physical Society (SPS), 2010, Basel, Switzerland
- Joint ICTP-FANAS Conference on Nanotribology, 2011, Trieste, Italy
- 14th International Conference on NC-AFM, 2011, Lindau, Germany
- Towards Reality in Nanoscale Material V, 2012, Levi, Finland
- 4th nanoMRI Conference, 2012, Ascona, Switzerland
- Swiss Nano Convention, 2013, Basel, Switzerland

Curriculum Vitea

Personal Information:

Markus Samadashvili geb. Langer

Hammerstrasse 75

4057 Basel

Switzerland

Email: Markus.Langer@unibas.ch

Date of Birth: 11th of August 1985 in Lörrach, Germany

Nationality: German

Family status: Married to Dr. Nino Samadashvili, 26th July 2013

Education:

1992 – 1996	Scheffelschule, Rheinfelden-Herten, Germany
1996 – 2005	Georg-Büchner-Gymnasium, Rheinfelden, Germany
2005 – 2008	Bachelor of Science in Physics, University of Basel
2008 – 2010	Master of Science in Physics, University of Basel **Master Thesis**: “Contrast inversion of the h-BN nanomesh”
2010 – 2014	Phd in Physics, University of Basel **PhD Thesis**: “non-contact friction studied with pendulum AFM”